Spring 1-1-2014

Formation of Microstructures in Crosslinked Polymer Films by Photocrosslinking of Monomers in Evaporating Solvents

Liang Wang
University of Colorado Boulder, liangwang2559@gmail.com

Recommended Citation

Wang, Liang, "Formation of Microstructures in Crosslinked Polymer Films by Photocrosslinking of Monomers in Evaporating Solvents" (2014). *Mechanical Engineering Graduate Theses & Dissertations*. 96.
https://scholar.colorado.edu/mcen_gradetds/96

FORMATION OF MICROSTRUCTURES IN CROSSLINKED POLYMER FILMS BY PHOTOCROSSLINKING OF MONOMERS IN EVAPORATING SOLVENTS

written by

LIANG WANG

B.E., Northwestern Polytechnical University, 2009

M.S., University of Colorado, 2012

A thesis submitted to the
Faculty of the Graduate School of the
University of Colorado in partial fulfillment
of the requirement for the degree of
Doctor of Philosophy
Department of Mechanical Engineering
2014

This thesis entitled:

FORMATION OF MICROSTRUCTURES IN CROSSLINKED POLYMER FILMS BY PHOTOCROSSLINKING OF MONOMERS IN EVAPORATING SOLVENTS

written by

Liang Wang

has been approved for the Department of Mechanical Engineering

____

Dr. Yifu Ding, Chair

____

Dr. Wei Tan, Committee Member

Date______________

The final copy of this thesis has been examined by the signatories, and we find that both the content and the form meet acceptable presentation standards of scholarly work in the above mentioned discipline.

ABSTRACT

Wang, Liang (Ph.D., Mechanical Engineering)

FORMATION OF MICROSTRUCTURES IN CROSSLINKED POLYMER FILMS BY PHOTOCROSSLINKING OF MONOMERS IN EVAPORATING SOLVENTS

Thesis directed by Professor Yifu Ding

Crosslinked microstructured polymer films have received much attention due to their potential applications. Currently, these polymer films can be fabricated through a range of processes and lithographic techniques. However, they often require multiple fabrication steps and expensive instruments. In this thesis, we report the structure formation of films obtained *via* a simple, low cost one-step synthesis/fabrication process, by *in situ* photocrosslinking of precursors during the evaporation of solvents.

Under controlled dry N_2 flow, the forced convective evaporation resulted in highly hierarchical film morphology, featuring a skin layer atop of a layer of microspheres. This unique morphology is determined by the interplay between fast solvent evaporation and reaction induced phase separation between the reactive precursor and the remaining solvent. For the first time, the skin layer formed during the evaporation was directly observed after the complete evaporation of the solvent. The thickness of the skin layer is dependent on the processing parameters including the N_2 flow rate, UV intensity and precursor concentrations. Under the free convection or by means of adding non-solvent, the skin layer formation could be suppressed. A model is presented that can qualitatively describe the skin layer formation and its dependence on the processing parameters, providing a mechanistic understanding of the photocrosslinking-

induced phase separation under evaporative environments. We further used *N*-isopropylacrylamide/carbon disulfide (CS_2) as a model system to study the evolution of the composition and morphology within the solution drop. Within seconds of the process, fast evaporation of solvent dominated, which resulted in the formation of a concentration gradient that led to a skin layer later. Subsequently the evaporation rate slowed down and excessive solvent activity due to the reaction resulted in the phase separation that not only interrupted the further growth of the capping skin layer but also generated a particulate layer underneath.

Using the same fabrication process but in the presence of moisturized N_2 flow, we successfully produced honeycomb like porous structures in the crosslinked polymer films. This is based on the "breath figure" formation during the *in situ* crosslinking of reactive monomer solutions. A range of precursor solutions, including tert-butyl acrylate/tetraethylene glycol dimethacrylate (TEGDMA) in chloroform, methyl methacrylate/TEGDMA in CS_2 and Norland optical adhesive 65 (NOA65) in CS_2 was crosslinked upon UV radiation under a moist and nitrogen saturated chamber and micro-size pores with reasonably uniformity were obtained in these crosslinked polymer films, illustrating the generality of this approach. The size, shape, uniformity and ordering of the pores show significant dependences on the casting conditions. In contrast, the pore morphology remains similar despite varying precursor compositions, suggesting that the pore-fixing process is still dominated by the solvent evaporation similar to that of conventional breath figure process, and is less dependent on the crosslinking process. We further observed the pores at the peripheral regions appeared more uniform in size and showed higher degree of ordering, due to the interplay between the solvent evaporation and crosslinking reaction. Detailed characterizations of the chemical and physical properties, including the glass transition temperature, thermal stability, and surface wettability of the porous films were carried out.

ACKNOWLEDGEMENTS

I would like to take this opportunity to thank all people involved throughout my pursuit of doctoral degree. To all of you, thank you for always being there for me.

First and foremost, I wish to give my great appreciation to my Ph.D. advisor, Dr. Yifu Ding for the support of my Ph.D. study and research. I am thankful for his aspiring guidance, invaluably constructive criticism and helpful advice. He has been supportive since the first day I working in the lab and always strove to provide an excellent platform for students to pursue their research interest with countless encouragement and freedom. His dedication, motivation, enthusiasm and profound knowledge make him an outstanding advisor. Without him, I would never have been able to finish this thesis.

Secondly, I express my warm thanks to all committee members: Dr. Christopher Bowman, Dr. Alan Greenberg, Dr. Yung-Chen Lee and Dr. Wei Tan. Thanks for all valuable input they have provided since my comprehensive examination, which has been a source of energy, and motivation to continue my research project. They are very kind to be my committee members and my thesis readers.

I would also like to thank all the lab mates and collaborators. Special thanks to Devid Maniglio, who helped me build up the reaction chamber that I have used in almost every experiment in the thesis. Although he went back to Italy in the beginning of my Ph.D study, we still have maintained active collaborations, which made it possible for the publication of my first journal paper. I need to thank Michael Skaug from Department of Chemical and Biological Engineering, with whom I have worked since last year. I have learned a lot of knowledge from him that is out of my field. My sincere appreciation also goes to the seniors, Dae Up Ahn, Sajjad Maruf and Zhen Wang, who were always willing to help whenever I had problems especially in

my first two years. I am also grateful to Zheng Zhang, and Lewis Cox for their valuable suggestions and discussions about research. They are fun and easy to talk with. I enjoy the time with them.

Additionally, I want to thank Dr. Wei Zhang and Chao Yu from Department of Chemistry and Biochemistry for the use of GPC. My grateful thanks are extended to Dr. Parag Shah for the help with near-IR and also to Dr. Mark Stoykovich and Kate Morrissey from Department of Chemical and Biological Engineering for meaningful discussions.

I would like to give my deepest gratitude to my parents. Thanks for supporting my study for so many years. I appreciate their understanding for my absence in the family for the past five years. I would also like to thank my dear girlfriend, Lei Bao, who has accompanied me throughout the hardship of PhD study.

Finally, I thank NSF for financial support.

TABLE OF CONTENTS

LIST OF TABLES

LIST OF FIGURES

SYMBOL LIST

T	Temperature
T_g	Glass transition temperature of polymer
ΔT	Temperature difference
T_m	Melting temperature
T_s	Spinodal temperature
T_q	Quench depth
t	Time
$t*$	A finite time associated with the growth of skin layer in a crosslinking solution
D	Mutual diffusion coefficient of the solution
D_c	Diffusion coefficient of CS_2 into N_2
$\emptyset_1$	Solvent volume fraction
$\emptyset_{1h}$	Solvent volume fraction at the top surface of the solution
$\emptyset_{1i}$	Initial solvent volume fraction of the solution
c	Concentration of polymer solution
$\emptyset_2$	Solute volume fraction (polymer or precursor)
$\emptyset_{2h}$	Solute (polymer or precursor) volume fraction at the top surface of the solution
$\emptyset_{2i}$	Initial solute (polymer or precursor) volume fraction
$\emptyset_{2g}$	Polymer volume fraction corresponding to the gel point
$\emptyset_{2n}$	Volume fraction of the solvent at network formation
h_0	Initial thickness of the solution
h	Solution thickness
$\dot{h}$	Velocity of the solution surface boundary
$\dot{h}_g$	Velocity of the interface between the remaining solution and the skin layer
ψ	Solvent volume fraction in the vapor phase right above the solution
ψ_∞	Solvent volume fraction in the vapor a distance infinitely far away from the solution
ψ^*	Solvent volume fraction of pure solvent in the vapor phase right above the solution
R	Gas constant
P^*	Vapor pressure of pure solvent
P_g	Partial vapor pressure of solvent right above the air-solution interface
χ	Flory-Huggins interaction parameter

J	Evaporation flux
J_0	Evaporation flux constant
Pe	Dimensionless parameter, Pe $\equiv h_0 J / D$
k	Mass transfer coefficient
$\overline{k_c}$	Average mass transfer coefficient
r_{skin}	Growth rate of the skin layer
b	Thickness of the crosslinked skin layer
r	Radius of a solution deposited on a solid substrate
k^{-1}	Capillary length
g	Gravitational acceleration
γ	Surface tension of the solution
ρ	Density of the solution
V	Volume of deposited solution
Ma	Marangoni number
Ma_c	Critical Marangoni number
Ra	Rayleigh number
Re	Reynolds number
Sh_L	Sherwood number
S_c	Schmidt number
l	Characteristic length of the solution
ν	Kinematic viscosity of the solution
α	Thermal diffusivity of the solution
β	Solution thermal expansion coefficient
u	N_2 flow rate
L	Length of the substrate in the N_2 flow direction
k_S	Thermal conductivity of the substrate
k_L	Thermal conductivity of the solution
k_R	Relative thermal conductivity, $k_R \equiv k_S / k_L$
θ	Contact angle of the solution drop
θ_c	Critical contact angle of the solution drop
θ_E	Contact angle of the solution drop in equilibrium state
d	Diameter of condensed liquid droplets

ε	Scaling factor in Section 2.2
x	Ratio of molar volumes of the polymers to solvent
A, B	Front factors depending on the specific network models
$\Delta\mu_1$	Chemical potential change of solvent after mixing
a_1	Activity of the solvent
υ_e	Concentration of elastically active network chains in a volume unit
$\bar{V}$	Molar volume of the solvent
Λ_m	Wavelength in spinodal decomposition
q	Interaction length of spinodal decomposition
m	Coordination number of pores in films prepared by breath figure templated assembly
F_m	Fraction of every coordination m
ξ	Entropy of pore packing
δ	Hildebrand solubility parameter
δ_s	Solubility parameter of solvent
δ_p	Solubility parameter of polymer
δ_d	Dispersion component of solubility parameter δ
δ_p	Polar component of solubility parameter δ
δ_h	Hydrogen bonding component of solubility parameter δ
f_d	Dispersion component of Teas parameter
f_p	Polar component of Teas parameter
f_h	Hydrogen bonding component of Teas parameter
$\bar{M}_N$	Number average molecular weight of polymer
n	Refractive index increment
H	Refractometer constant
W	Peak area from gel permeation chromatography
ΔH_v	Evaporation enthalpy of solvent
ΔH_c	Polymerization enthalpy
ΔH_i	Heat generated by UV adsorption

1 INTRODUCTION

Crosslinked microstructured polymers are promising due to their potential applications in biotechnologies[1–6], photonics[7,8], electronics[9,10], and separation membranes[11]. Microstructures of polymers broadly refer to nano/micro particles, micro/macroporous matrix, and their combined morphologies. It is challenging to process crosslinked polymers due to their inability to dissolve and to plastically deform even at high temperatures. Therefore, the structures in the crosslinked polymers are often formed either prior to or at the same time of crosslinking reaction. Processes that are capable of fabricating controlled and tunable microstructures in crosslinked polymers are highly desirable.

For example, several strategies have been developed to synthesize crosslinked micro and nanoparticles, including polymerization methods (emulsion[12], suspension[13], precipitation[14], and dispersion[15] polymerization), lithographic techniques (photolithography[16], soft lithography[17], and imprint lithography[18]), and microfluidic synthesis[19]. However, these strategies often suffer from low throughput, high cost, long operation time and specific requirement of reactant chemistry.

On the other hand, crosslinked micro/macroporous films have been created through a range of techniques as briefly reviewed as follows. Top-down lithographic techniques can reliably fabricate micro- or nano-pores into crosslinked polymer films, with precise control over the shape, size, and spatial ordering *via* the design of the masks or templates. Normally, these lithographic techniques only fabricate single-layer holes. To achieve multilayer ordered pores, interference lithography, based on optical wave mixing, are needed.[20–24] However, these approaches often require multiple fabrication steps, expensive instruments, pre-patterned templates or masks, and specific material chemistry. A scalable approach to create porous crosslinked polymer films is the foaming process, similar to the manufacturing of microcellular thermoplastic films.[25] This process requires long saturation time under high pressures, and produces a network with a broad distribution in both size and shape.

Processing methods based on reaction-induced phase separation between the polymer network and solvent can also create three-dimensional porous network films.[26–28] Reaction induced phase separation (RIPS) of polymers refers to the process through which polymerization, including crosslinking of one component within a homogeneous mixture, leads to the separation between the reacting phase and the inert phase. Depending on the phase separation mechanism, a range of morphologies can be created in crosslinked films.

In recent years, self-assembly based fabrication approaches become increasingly attractive due to their simplicity, high throughput, and relatively low cost.[29–31] Among them, “breath figure templated assembly” (BFTA) is a simple and elegant bottom-up assembly technique to create ordered pores in polymeric films.[32–35] BF exploits the nucleation and assembly of condensed liquid droplets, within an evaporating polymer solution. The evaporation of the volatile solvent causes a local temperature drop in the concentrating polymer solution. Subsequently, saturated vapor condenses in such a cooler surface/film *via* a nucleation process, and self-organizes into well-ordered honeycomb like morphology.[36] Once the polymer solution evolves into a gel-like state, the structure is then fixed. With the removal of entrapped droplets, a polymer film-containing honeycomb like pores is obtained.

Almost all polymers used in the BFTA are non-crosslinked ones, obviously due to the required solubility in the volatile solvent. To create crosslinked porous film based on BFTA, a post-crosslinking strategy is often employed. The specific crosslinking chemistry adopted ranges from oxidation/crosslinking of linear polystyrene by deep UV[37–41], to imidization reaction[42], to high-temperature curing of poly(*para*-phenyleneethynylene) containing azide groups[43], to maleic anhydride copolymers[44] and polycinnamate[45], and to polymers containing carbon-carbon double bond such as polybutadiene[46,47] and polyisoprene[48,49]. This fabrication route requires a tedious synthesis to grant BF forming polymers with crosslinkable chemical groups, and thus not applicable to a broad range of polymer networks. Another issue with the post-crosslinking strategy is significant structural collapse of BF films that has been reported by several researchers.[42,43]

The review of the past and current research above illustrates the interest and need to create desirable microstructures in crosslinked polymers. To date, although a variety of processes and lithographic techniques have been developed to fabricate crosslinked microstructured polymers, they often require a considerable amount of operation time and expensive equipment, which evidently possesses disadvantages of high cost and low throughout. Therefore, a new fabrication strategy without the drawbacks of current processing techniques is needed. On the other hand, limited studies using a volatile solvent during the process show the evaporation of solvent can actually lead to a series of unique film morphologies that cannot be obtained in a non-evaporating solvent medium due to the interplay between in-situ crosslinking reaction and fast solvent evaporation. However, these studies are at the preliminary stage without systematic investigation. Therefore, all we mentioned above provide a motivation to find and implement a methodology that can create abundant kinds of microstructures in the crosslinking matrix in a cost-effective and fast way.

In this thesis we aim to develop a low-cost, facile one-step fabrication strategy to create a plethora of microstructures in crosslinked polymers by simultaneous photocrosslinking of the precursors and fast evaporation of an organic solvent. The utilization of UV initiated photocrosslinking reaction and a volatile solvent permits us to obtain crosslinked microstructured polymers in just a couple of minutes. The results regarding the mechanistic study will be presented which elevates the understanding of the convoluted morphological evolution, thus making it possible to fine tune the final film morphologies for targeted applications.

The layout of this thesis is as follows. Chapter 1 is introductory mainly about the motivations and objectives of this thesis work. In Chapter 2 the concept of photocrosslinking of precursors in an evaporating solvent breaks down to individual aspects, namely, drying of a polymer solution under dry/moist N_2 flow and photopolymerization induced phase separation. A brief review is presented regarding these aspects. Chapter 3 focuses on the experimental setup, sample preparation and characterizations methods used. In Chapter 4, we investigated the formation of hierarchical structures featuring a skin layer atop of a particulate layer, which was prepared under dry N_2 flow. Both theoretical and experimental efforts were made to understand the underlying mechanism. Moreover, we demonstrated the versatility of this method to prepare microstructured hydrogels and studied the time-dependent compositional and morphological evolutions. In Chapter 5, we studied the formation of crosslinked honeycomb like porous films in the presence of moisture. Detailed characterizations including morphological, chemical and physical properties of the fabricated porous films were carried out. Lastly in Chapter 6 the entire thesis work is summarized and outlook for the future research work is suggested.

2 BACKGROUND

This thesis aims to investigate the structural formation in crosslinked polymers resulted from *in situ* photocrosslinking of precursors in an evaporating solution (Figure 2.1). Clearly the structural formation is a result of interplay between a couple of thermodynamic and dynamic processes: evaporation of solvent, photocrosslinking reaction, reaction induced phase separation (resulting in the particle layer shown on the left schematics of Figure 2.1), and condensation of water droplets (resulting in the pores shown in the image on the right of Figure 2.1). In the following, study of these individual processes from current literatures is briefly reviewed.

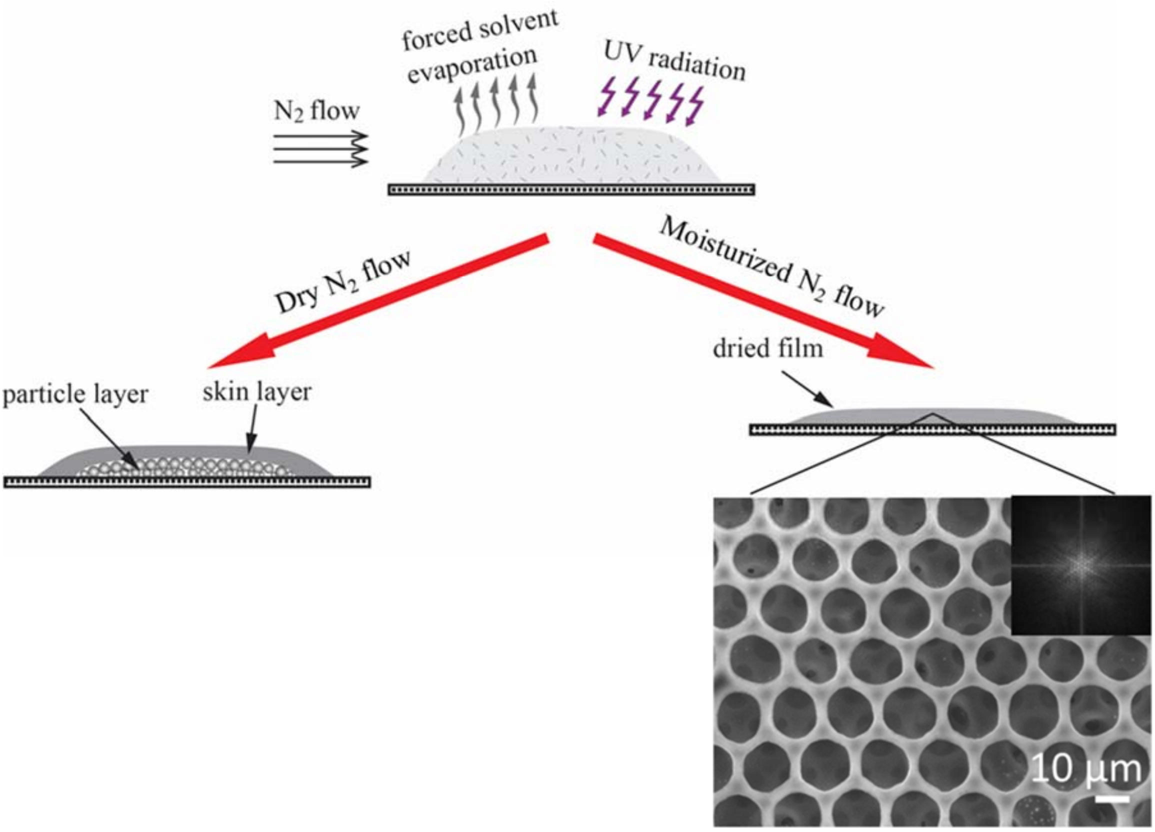

Figure 2.1 Schematic illustration of structural formation in a crosslinked polymer by *in situ* photocrosslinking of precursors during the evaporation of the solvent. Depending on the humidity in the N_2 flow, two distinct film morphologies can be formed. The image on the right was taken by a scanning electron microscope (SEM) showing the surface morphology of resulting film prepared under moisturized N_2 flow. The inset of the image is the fast Fourier transform (FFT), showing the pores are hexagonally close packed.

2.1 Drying of a polymer solution

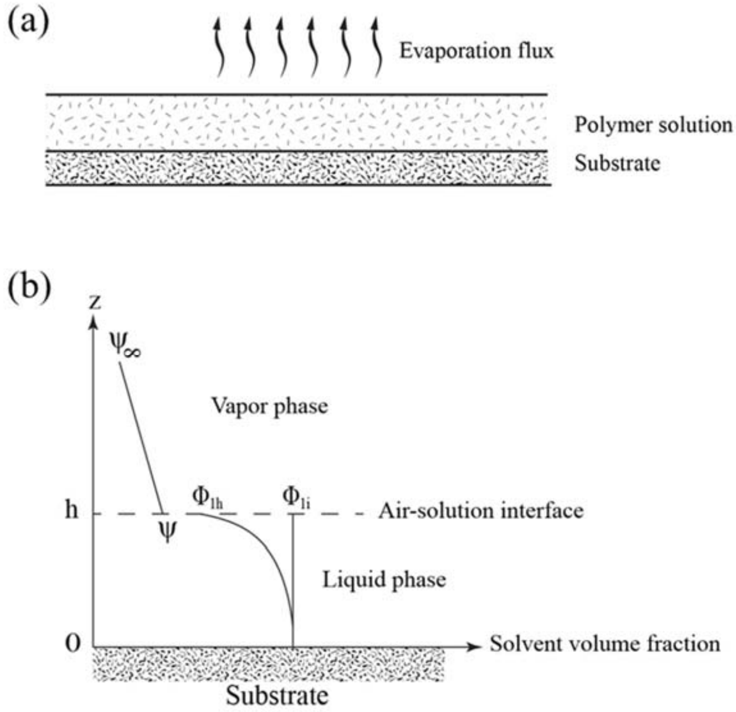

Figure 2.2 (a) drying of a homogeneous polymer solution on a solid substrate, (b) solvent volume fraction profile at the vertical dimension.

The study on the drying of a polymer solution has attracted broad interests in recent years due to its wide industrial applications, such as film coating[50,51] and inkjet printing[52,53]. In a typical drying processing, a homogeneous polymer solution is cast on a solid substrate, as illustrated in Figure 2.2a. Within the liquid phase, solvent evaporation causes a concentration gradient (Figure 2.2b) and therefore diffusion occurs according to Fick's second law,

$$\frac{\partial \emptyset_1}{\partial t} = \frac{\partial}{\partial z}\left[D(\emptyset_1, T)\frac{\partial \emptyset_1}{\partial z}\right] \qquad \text{Eqn 2.1}$$

where $\emptyset_1$ is solvent volume fraction in the liquid phase and $D(\emptyset_1, T)$ is mutual diffusion coefficient of the solution that is dependent on temperature (T) and $\emptyset_1$[54]. Cautions must be taken, as Eqn 2.1 is only valid on the premise that $T_g < T$, where T_g is the glass transition temperature of the plasticized polymer (due to the existence of solvent). For the diffusion in polymer at glassy state, different diffusion equation applies. The concentration gradient may be relieved depending on the concentration relaxation time (h^2/D) as compared to the total drying time.[55]

At the air-solution interface, solvent volume fraction at the top surface of the solution ($\emptyset_{1h}$) and in vapor phase right above the solution (ψ) can be correlated by Flory-Huggins theory,[56,57]

$$\psi = \psi^* \emptyset_{1h} \exp[1 - \emptyset_{1h} + \chi(1 - \emptyset_{1h})^2] \qquad \text{Eqn 2.2}$$

where $\psi^* = P^*/(RT)$ is solvent volume fraction of pure solvent in the vapor phase right above the solution, $P^*$is vapor pressure of pure solvent that is dependent on T, R is gas constant, and χ is the Flory-Huggins interaction parameter between the polymer and the solvent. Assuming a dilute solution (*i.e.* Henry' law) and $\chi = 0$ (*i.e.* good solvent), Eqn 2.2 can be simplified as

$$\psi = \psi^* \emptyset_{1h} \qquad \text{Eqn 2.3}$$

There is also a concentration gradient of solvent in the vapor phase (Figure 2.2b). The solvent vapor near the interface is continuously transferred away from the solution either by diffusion (a.k.a. free convection) or a moving gas flow (a.k.a. forced convection), hence the evaporation flux. This evaporation flux J is given by[58,59]

$$J = k(\psi - \psi_\infty) \approx J_0 \emptyset_{1h} \qquad \text{Eqn 2.4}$$

where k is the mass transfer coefficient, ψ and ψ_∞ are the solvent volume fraction in the vapor phase right above the air-solution interface and a distance infinitely far away from the solution, respectively, and J_0 is a constant. Eqn 2.4 reveals that evaporation flux decreases as drying proceeds.

Another accompanying effect of drying is the decrease of $D(\emptyset_1, T)$, as seen from Figure 2.3.[60] In this example, $D(\emptyset_1, T)$ of polyvinyl alcohol aqueous solution almost remained same in the low concentration region and decreased dramatically by a few orders of magnitude as the polymer concentration increases, particularly as the solution approaches gelation and vitrification.

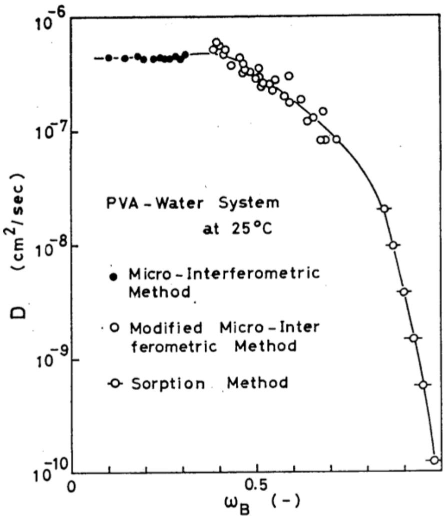

Figure 2.3 Mutual diffusion coefficient of polyyinylalcohol (PVA) aqueous solution as a function of PVA weight fraction (ω_B).[60]

The gradually slowed drying kinetics of a polymer solution due to the decreasing $D(\emptyset_1, T)$ and J has been observed in experimental and simulation works.[36,56] Figure 2.4 shows an example of a drying polystyrene (PS)/carbon disulfide (CS_2) solution. In the beginning of the evaporation, the slope of solution mass loss (drying rate) is almost constant, especially for very dilute solutions. Starting from ~ 50 s, drying rate of 5 wt.% solution is appreciably reducing (corresponding to ~ 10 wt.% concentration), as manifested by the decreasing slope.

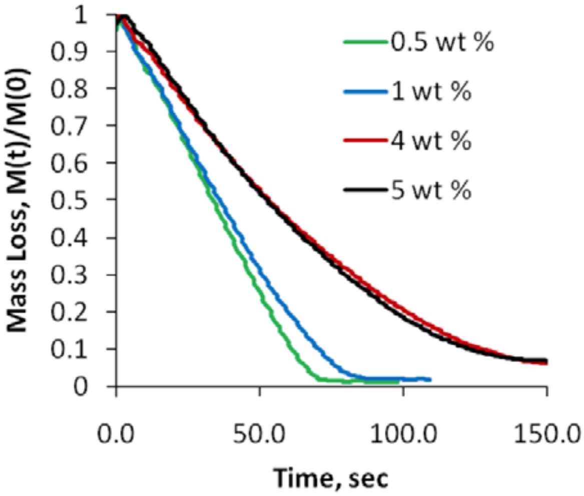

Figure 2.4 Mass loss profile of polystyrene/carbon disulfide solutions under 0.75 m/s airflow with varying polystyrene concentrations. Mass loss in the y axis is normalized by the initial solution weight.[36]

In the following subsections, we will focus on the phenomena occurring at the localized region of a drying polymer solution. At the air-solution interface, a thin, gelled layer may form due to both the concentration gradient and slow concentration relaxation rate of the solution. At three-phase contact line, faster evaporation leads to the non-uniform temperature across the solution surface that accounts for a variety of instability flows within the solution.

2.1.1 Skin effect

At the early stage of drying, the fast evaporation of the solvent may generate a concentration gradient in the vertical direction. The concentration at the top surface may reach gelation concentration, thus forming a thin, elastic skin layer. In the past decade, an increasing amount of research efforts has been made to understand the mechanism governing the skin formation. A theoretical interpretation of the skin layer during the fast drying of a polymer solution was first reported by de Gennes.[58] Doi and co-workers proposed an analytic model to describe the criterion for the formation of a skin layer and its growth rate.[57,59,61] Alongside these theoretical efforts, Pauchard and Allain experimentally investigated the buckling instability on the skin layer during the drying of a polymer solution.[62,63]

Experimentally, it is challenging to directly measure the polymer skin layer either *ex situ* or *in situ* during the solvent evaporation, because of the re-dissolution and/or low mechanical strength of the uncrosslinked polymers. Until recently, Shimokawa et al. measured the skin layer during the early stage of the evaporation by combining the electric field tweezers with an optical lever technique using parallel-lined laser beams.[64] For the first time, the growth rate of the skin layer for polyvinyl acetate and polymethyl methacrylate (PMMA) solution as a function of time, as well as their stiffness, was determined.[65]

Theoretically, Doi and co-worker has proposed a criterion for the skin layer formation:[59]

$$\mathrm{Pe} \equiv \frac{h_0 J}{D} > \frac{\emptyset_{2g} - \emptyset_{2i}}{\emptyset_{2i}(1 - \emptyset_{2i})} \qquad \text{Eqn 2.5}$$

where h_0 is the initial thickness of the polymer solution, $\emptyset_{2i}$ and $\emptyset_{2g}$ are initial polymer volume fraction and polymer volume fraction corresponding to the gel point, respectively. Eqn 2.5 implies that for a given polymer/solvent pair that has an associated gel point ($\emptyset_{2g}$) and D, a relatively high initial polymer concentration ($\emptyset_{2i}$) or evaporation flux (J) or initial solution thickness (h_0) may result in the emergence of skin layer.

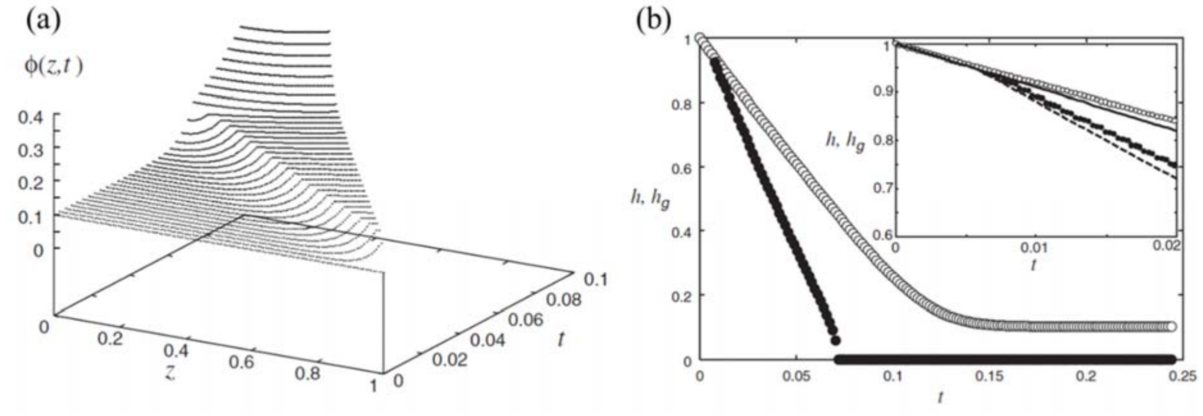

Figure 2.5 (a) Space-time plot of a drying polymer solution experiencing the skin formation using a numerical approach, (b) skin layer thickness as function of time by the numerical approach and inset by the analytical approach.[59] $\emptyset_{2i} = 0.1, \emptyset_{2g} = 0.2$.

The drying process of a polymer solution experiencing a skin layer formation can be depicted as follows. At the beginning, due to the fast evaporation rate and/or long concentration relaxation time (h^2/D) (that is not able to homogenize the solution), a concentration gradient forms. Once the criterion is met (Eqn 2.5), a thin skin layer emerges ($\emptyset_{2h} \geq \emptyset_{2g}$), as shown in Figure 2.5a. This skin continues to growing downwards at a constant rate, r_{skin}, given by[59]

$$r_{\text{skin}} = \dot{h} - \dot{h_g} = J_0 \frac{\emptyset_{2i}(1 - \emptyset_{2g})}{\emptyset_{2g} - \emptyset_{2i}} \qquad \text{Eqn 2.6}$$

where $\dot{h}$ is the velocity of the solution surface boundary, and $\dot{h_g}$ is the velocity of the interface between the remaining solution and the skin layer. The constant growth rate of skin layer is also confirmed by both numerical (Figure 2.5b) and analytical (inset of Figure 2.5b) approaches.

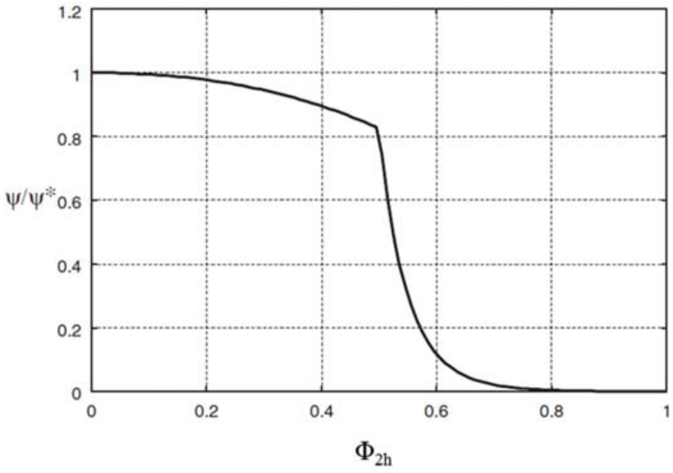

Figure 2.6 Solvent volume fraction in the vapor phase right above the air-solution interface vs. solvent volume fraction in the solution phase right below the interface, simulated by numerical method.[57] Gel point is $\Phi_{2h} = 0.5$.

The formation of the skin does not prevent the continuous evaporation of the remaining solvent and in fact the solvent can readily diffuse through the capping skin layer into the vapor phase. This is because the formed skin is soft (*i.e.* Young's modulus of the skin layer is measured ~ MPa as opposed to that of its solidified counterpart ~ GPa[65]) with significant amount of entrapped solvent. Nonetheless, the formation of the skin layer greatly reduced the evaporation rate.[57,62,66,67] A numerical approach clearly shows the dramatic decrease of ψ and therefore the decrease of J according to Eqn 2.4 at the gel point, as shown in Figure 2.6.[57] Eventually, the skin extends to the whole thickness of the solution, meaning that the whole solution is now gelled. The solvent in the gelled solution may still evaporate afterwards (Figure 2.5a). It is worth noting that the dried morphology of the films that have experienced the skin formation is indifferent from those without, thus obscuring the discovery of the skin formation by researchers.

2.1.2 Temperature profile and associated types of convections within the solution drop

The evaporating solvent at interface undergoes rapid phase change (with an associated endotherm, ΔH_v) that brings in the localized cooling effect. It is known that the evaporation rate is non-uniform across the solution surface, implying that the degree of cooling is varying in different spots. As a result, the temperature profile across the solution surface can be highly non-uniform depending on the rate of the heat/mass transfer.

Before we elaborate the temperature profile and its consequence, it is worth to know the shape a polymer solution adopts on a rigid substrate, which plays an important role in the drying process. After deposited without mechanical forces, *i.e.* spin coating or blade casting, the solution spreads out spontaneously until an equilibrium contact angle is achieved. The solution shape in equilibrium is dependent on the relative ratio of the solution radius (r) to the capillary length ($\kappa^{-1} = (\gamma/\rho g)^{1/2}$)[68], where γ is surface tension of the solution, ρ is the density of the solution, and g is the gravitational acceleration. For the small drop ($r < \kappa^{-1}$), spherical cap shape is adopted (Figure 2.7a) because the gravity is negligible and the highest point (h_0) can be estimated by solving

$$V = \frac{\pi h_0 \left(3r^2 + {h_0}^2\right)}{6} \qquad \text{Eqn 2.7}$$

where V is the volume of deposited solution. On the other hand, for the heavy drop ($r > \kappa^{-1}$), gravity flattens the drop that forms a puddle (Figure 2.7b). And the thickness of this puddle (h_0) is given by

$$h_0 = 2\kappa^{-1} \sin\frac{\theta_E}{2} \qquad \text{Eqn 2.8}$$

where θ_E is the contact angle of the solution drop in equilibrium state.

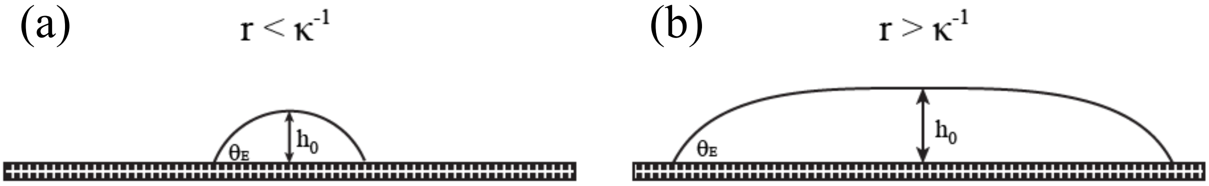

Figure 2.7 Schematic illustration of the shape a polymer solution adopts when deposited on a rigid substrate (a) spherical cap (b) puddle.

For a polymer solution having such geometry (spherical cap or puddle), the evaporation rate is reportedly non-uniform across the entire surface with evaporation rate at the contact line being the largest,[69–72] and so is the temperature. Two types of convections may coexist due to the temperature gradient across the solution surface. One is known as Marangoni convection or thermo-capillary flow. It arises due to the surface tension gradient as a result of the temperature gradient, *i.e.* surface tension (γ) is negatively dependent on T for most substances. Figure 2.8a shows the streamline of Marangoni convection in a sessile solution drop by the lubrication analysis.[71] A dimensionless number (*Ma*) is used to characterize the relative effects of surface tension gradient to viscous damping forces and it is given by[70,73–75]

$$M_a = -\frac{d\gamma}{dT}\frac{l\Delta T}{\rho\nu\alpha} \qquad \text{Eqn 2.9}$$

where ΔT is the temperature difference, l is the characteristic length, ν is the kinematic viscosity, and α is the thermal diffusivity of the solution. For Marangoni convection to occur in a solution, a critical Ma_c has to be met.[73,74]

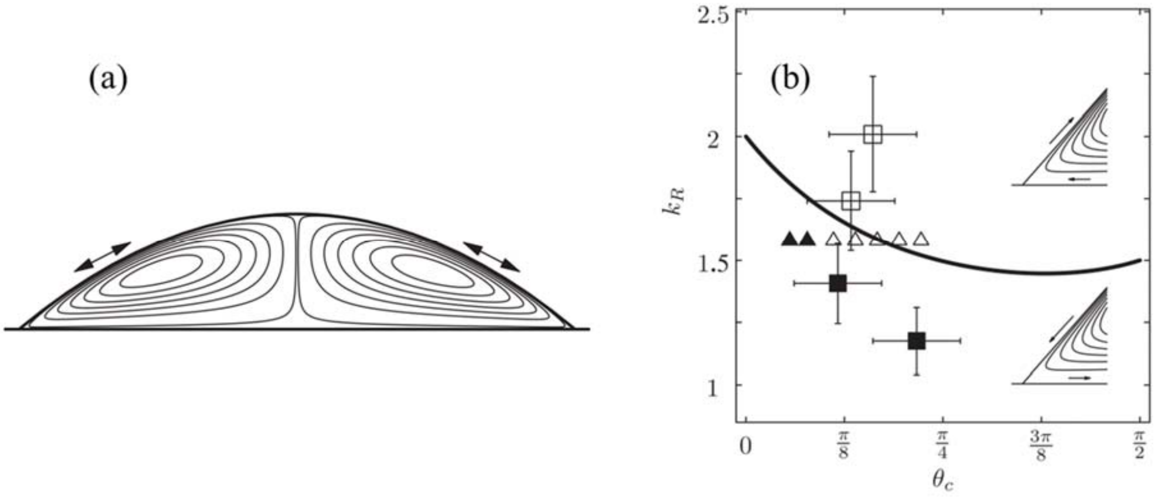

Figure 2.8 a) Streamlines of Marangoni flow in a sessile drop and b) its direction dependence on the relative thermal conductivities of the substrate (k_S) and the solution (k_L) and on the contact angle (θ).[71]

The direction of Marangoni convection in a sessile drying solution is expected to be dependent on the temperature gradient on the surface. Intuitively, the temperature at the contact line is lowest since the evaporation rate is largest.[76] This hypothesis however is disapproved by others who believe that the apex of the solution is the coldest spot because the apex is furthest away from the substrate which serves as the heat source for the solution above.[69] Regardless, the argument that the temperature gradient from the top of the solution to the contact line is monotonic is widely accepted, although few exceptions do exist.[72] Until recently, the temperature gradient (hence the direction of Marangoni convection) reportedly depends on relative thermal conductivities (k_R) of the substrate (k_S) to the solution (k_L) and on the CA (θ) as shown in (Figure 2.8b).[71,75] The solid line in Figure 2.8b is given by[71]

$$k_R = \tan\theta_c \cot\left(\frac{\theta_c}{2} + \frac{{\theta_c}^2}{\pi}\right) \qquad \text{Eqn 2.10}$$

where is θ_c the critical CA. Above this solid line, the temperature decreases from contact line to apex with contact line being the hottest and apex being the coldest, therefore the flow pattern is clockwise (upper inset); while below this solid line, the temperature profile is reversed and flow pattern becomes counterclockwise (lower inset).

The other convection is the buoyancy-driven convection, also called Rayleigh-Bénard convection, based on the fact that the density of solution is dependent on the temperature.[73,74,77–80] Similar to Ma, a dimensionless Rayleigh number (Ra), which expresses the ratio of the buoyant force to the viscous damping forces, is given by[77,78]

$$R_a = \frac{\Delta T g \beta l^3}{\nu \alpha} \qquad \text{Eqn 2.11}$$

where β is the solution thermal expansion coefficient. The size of the polymer solution of interest in laboratory study is fairly small with base radius varies from millimeter to submicron. In this case, the buoyancy-driven convection is significantly smaller than Marangoni convection ($Ra \propto l^3$ while $Ma \propto l$) and it is safe to neglect the buoyancy-driven convection. Therefore only Marangoni convection will be discussed in the rest of the thesis.

2.2 Drying a polymer solution under a saturated vapor - BFTA

The phenomenon of moisture condensing on a cold surface and thus forming a pattern of foggy array is ubiquitous. The formed pattern was termed breath figure (BF) and was first studied more than 100 years ago.[81–83] Since the last two decades, using BF to template microporous polymer films has been extensively investigated.[32,35] The essence of this idea is to use a dilute polymer solution containing a volatile solvent. During the evaporation of the solvent, a considerable temperature drop occurs in the solution, which creates a cold surface that induces the BF formation; and the solidifying polymer eventually fixes the foggy imprints, thus forming microporous films after the removal of the condensed liquid drops (see Figure 2.9).

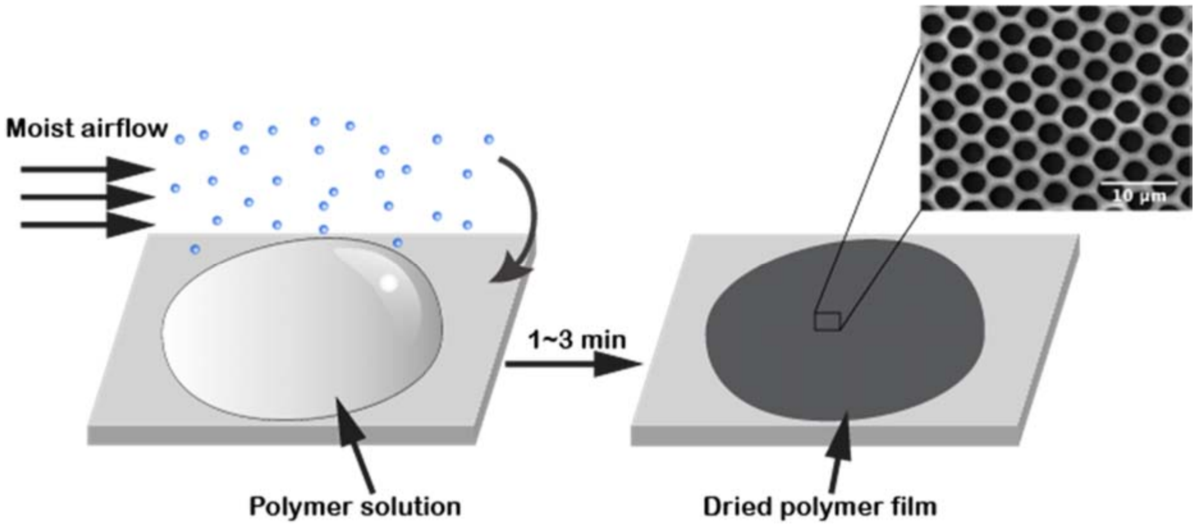

Figure 2.9 Schematic of BF formation under moisturized airflow.

The mechanism governing the BF formation in an evaporating polymer solution is not yet fully understood due to its highly dynamic, non-equilibrium nature. A generalized picture however can be depicted as shown in Figure 2.10. A dilute polymer solution having a volatile solvent such CS_2 has extremely rapid evaporation rate and significant enthalpic change at the air-solution interface, resulting in localized temperature drop that may reach as low as 0 °C (Figure 2.11).[36] Note that the temperature in such an evaporating solution drop is non-uniform as mentioned above, and Figure 2.11 shows the local temperature sensed by a single probe.

Nonetheless, such a cold surface, albeit non-uniform temperature, makes it possible for the condensation of the saturated vapor (such as water, methanol) in the atmosphere *via* heterogeneous nucleation if the local temperature brought down by cooling is lower than the dew point of this vapor. These condensed droplets are isolated and dispersed randomly across the solution surface (Figure 2.10-1). These droplets are able to grow in size through the uptake from the surrounding vapor. Prior to the maximum surface coverage, the growth rate of the droplets is given in terms of diameter as a function of time by $d \propto t^{\varepsilon}$, where ε was found to be between 0.3-0.35 if there no appreciable coarsening/coalescence occurs.[84–87] Indeed coalescence is diminished to the greatest extent due to the barrier effect by the Marangoni convection and/or the polymer layer encasing around the droplets.[35,87,88] Moreover, the growing droplets start to re-arrange itself according to the neighboring ones and are hexagonally close packed into rafts, as seen in Figure 2.10-3. The rafts grow in size by coordinating more droplets and at certain instant they start to collide with one another (Figure 2.10-4).

Apparently, the raft has lower mobility as compared to individual droplets, therefore the collision results in the defects such as point defects (missing droplets) and grain boundaries. The maximum surface coverage is expectedly achieved (Figure 2.10-6). Depending on the viscosity of the solution at this instant, further growth of droplets may occur through coalescence $d \propto t$, which enlarges the pore size distribution in the final morphology.[84–86] In some cases, this whole layer of the close-packed droplets may sink into the solution, allowing the formation of additional one or multiple layers atop that repeat the same process described above. Upon the complete drying with removal of both solvent and condensed liquid, a one-layered or multilayered microporous film is obtained. These pore arrays are usually hexagonally close packed which corresponds to the lowest free energy.[89] In the presence of external interference during the process, *i.e.* inclined substrate, square or rhombohedral arrangements may be achieved.[90,91]

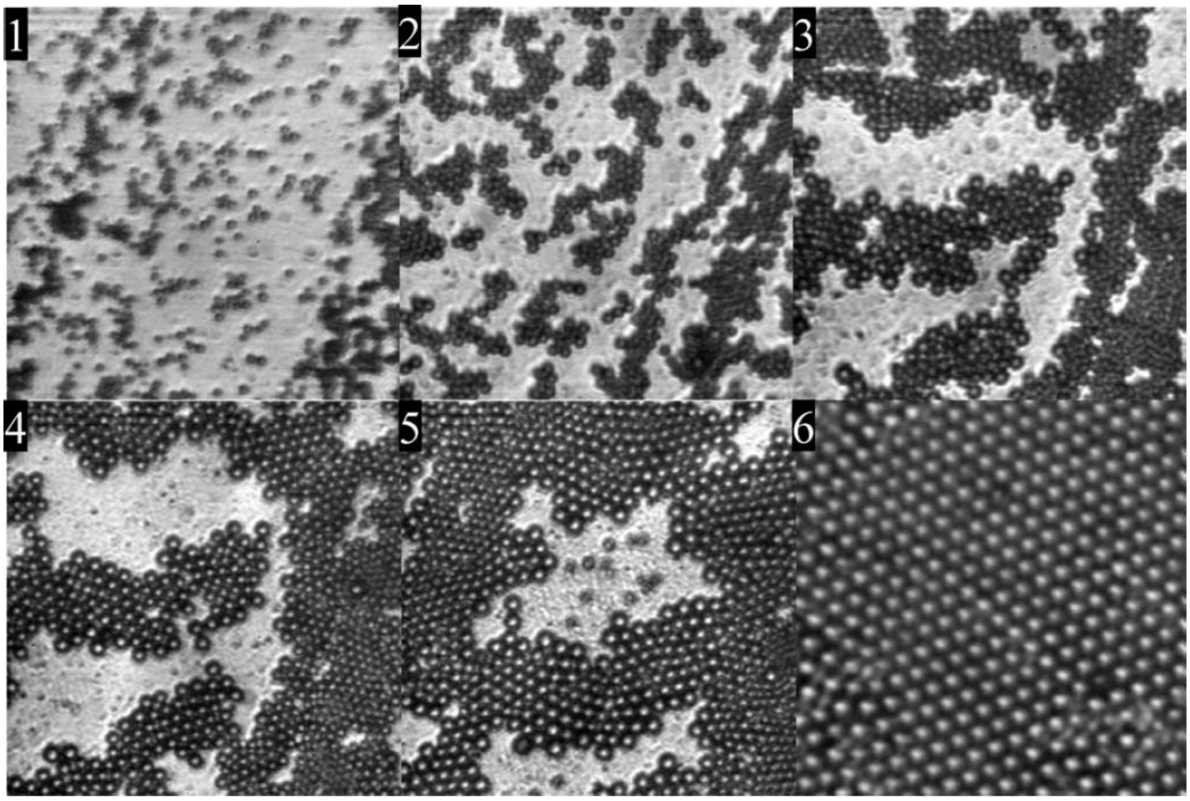

Figure 2.10 Observation of BF formation using a PS/CS2 solution by optical microscope (180 × 180 μm).[92]

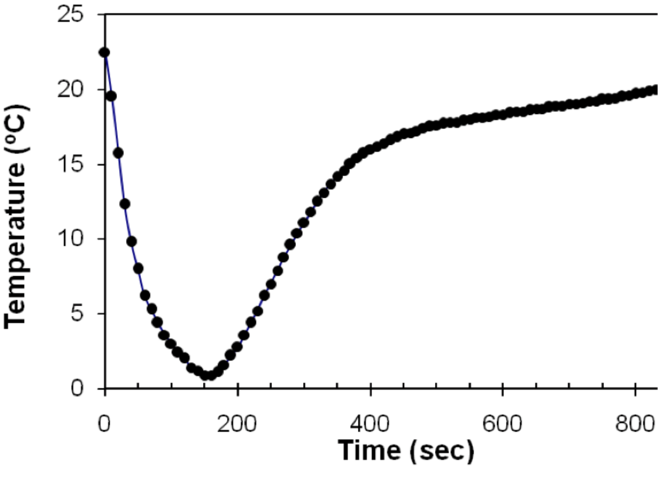

Figure 2.11 Temperature evolution of BF formation process using PS/CS2 solution by embedded thermocouple method.[36]

The selection of polymer solution systems and casting conditions is key to the final morphologies. We talk about the polymer solution systems first. Generally, variables regarding a polymer solution system include types of polymer and solvent, and solution concentration. A wide range of polymers have been demonstrated to form regular BF structures, from homopolymers such as (PS) and polyphenylene oxide (PPO)[35,93], to block copolymers or functionalized polymers[32,94–98], to biodegradable polymers[99], to organometals and functionalized metal nanoparticles[100–102] or ceramic precursors[103]. With respect to solvent choices, rule of thumb is to use a solvent with high volatility and none or least miscibility with the condensed liquid during the BF formation process. A volatile solvent dries out shortly, which significantly limits the diffusion of condensed liquid deep into the solution, making the nucleation and growth process almost a surface phenomenon. Otherwise, the liquid may act as the non-solvent for the polymer, thus causing phase separation in a ternary phase diagram. This actually is a phase inversion concept to prepare irregular microporous matrix and is termed "vapor induced phase separation".[104]

In terms of casting conditions, a variety of parameters can be chosen including relative humidity, airflow rate, ambient temperature and pressure, substrate shape such as planar or non-planar, and substrate surface roughness and wettability, flow rate (static or dynamic), ambient temperature and pressure. Some of the parameters may have the same effects. For example, increasing airflow rate to enhance the evaporation rate is equivalent to decreasing the ambient pressure.[33] Regardless, manipulating a set of these parameters makes the BF method a highly tunable process, e.g. a wide range of pore size can be readily prepared from 100 nm to 20 μm.[33,105]

2.3 Photopolymerization induced phase separation

For a precursor-solvent binary system upon UV radiation, the instantaneous thermodynamics of a reacting solution can be expressed as,[106–108]

$$\frac{\Delta\mu_1}{RT} = \ln a_1 = \ln(1-\emptyset_2) + \emptyset_2\left(1-\frac{1}{x}\right) + \chi\emptyset_2^2 + \upsilon_e\bar{V}\left(A(\emptyset_{2n})^{2/3}{\emptyset_2}^{1/3} - B\emptyset_2\right) \qquad \text{Eqn 2.12}$$

where $\Delta\mu_1$ is the chemical potential change of solvent after mixing, a_1 is the activity of the solvent, $\emptyset_{2n}$ equals to the volume fraction of the solvent at network formation, x is the ratio of molar volumes of the polymers to solvent, υ_e is the concentration of elastically active network chains in a volume unit, $\bar{V}$ is the molar volume of the solvent, and A and B are front factors depending on the specific network models. Note that the last term in Eqn 2.12 only contributes to the solvent activity when the three dimensional network has already formed.

Eqn 2.12 suggests several causes for phase separation. The most commonly observed is called liquid-liquid demixing. For a non-evaporative solution, $\emptyset_2$ is constant while x increases continuously due to the UV initiated polymerization, and therefore solvent activity, $a_1$increases (Eqn 2.12). The increasing a_1 at certain instant may exceed the unity and as a result reaction induced phase separation (RIPS) sets in.[109,110] This can be more clearly described with the graphical illustration in Figure 2.12, which shows an upper critical solution temperature (UCST) phase diagram. In fact, RIPS can also occur in lower critical solution temperature (LCST) phase diagram. The point, $P(\emptyset_2,\ T)$ represents a homogenous solution, as it appears in the one-phase region prior to the UV photopolymerization. As the reaction takes place, the phase diagram moves up and the critical point shifts to the left. At certain instant, $P(\emptyset_2,\ T)$ may enter the two-phase region, hence the onset of phase separation.

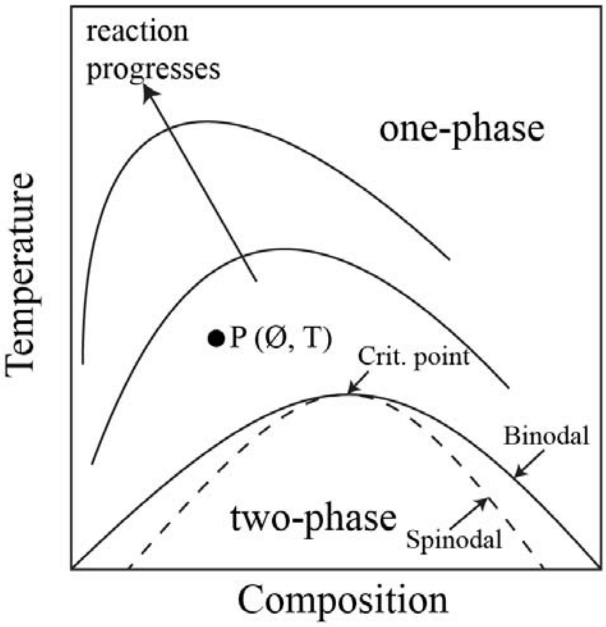

Figure 2.12 Illustration of reaction induced phase separation in an UCST phase diagram.[109]

Other causes that induce phase separation are subtle. One is called χ-induced syneresis. In particular, during the polymerization reaction, the change in the composition and temperature (due to the reaction heat) of the solution, and/or the molecular weight buildup of the polymer chains may result in the change of χ, thus inducing phase separation. On the other hand, in the presence of crosslinker in the solution, the last term in Eqn 2.12 comes to play *via* υ_e induced syneresis as the crosslinking density of individual gels increases variably beyond the gel point.

Regardless of the difference causes, the phase separation always occurs *via* either nucleation and growth (NG) mechanism at metastable region (between binodal and spinodal curves) or spinodal decomposition (SD) at unstable region (within the spinodal curve), depending on where $P(\emptyset_2, T)$ traverses the phase diagram (Figure 2.12). When the $P(\emptyset_2, T)$ falls into the metastable region as result of reaction, multiple nuclei forms at random sites of the solution with nearly equilibrium composition that contains very low concentrations of solvent *via* either homogenous nucleation process or heterogeneous nucleation in the presence of exotic surfaces. Once the critical diameter is met, the forming nuclei can further grow in size at the expense of surrounding materials or by engulfing other particles through coarsening. Due to both the random nucleation time in the solution and coarsening process, the resulting particles *via* NG mechanism will have a broad distribution in size.

On the other hand, when the polymerization of the precursors thrust the solution into the unstable region of the phase diagram, concentration waves occurs spontaneously. The fastest growing wave, with a wavelength of Λ_{m}, becomes the dominant structure. Here the Λ_{m} is given by[109,111]

$$\Lambda_m \approx 2\pi q\left(3T_q/T_s\right) \qquad \text{Eqn 2.13}$$

where q is the interaction length, T_q is the quench depth and T_s is the spinodal temperature. Normally, one of the two continuous phases, namely polymer-rich and solvent-rich, breaks into droplets due to the interfacial fluctuations thus forming uniform particles with particle size reminiscent of the dominant spinodal wavelength. If there is no constraints, the forming particles may further coarsen with surrounding particles like that occurs in NG mechanism, eventually resulting in agglomeration of particles with wide size distribution. In the presence of crosslinker in the solution, the elasticity stemmed from crosslinking reaction significantly limits the coalescence of the particles and expectedly a connected-globular structures is resulted upon the completion of the process (Figure 2.13).[108–110]

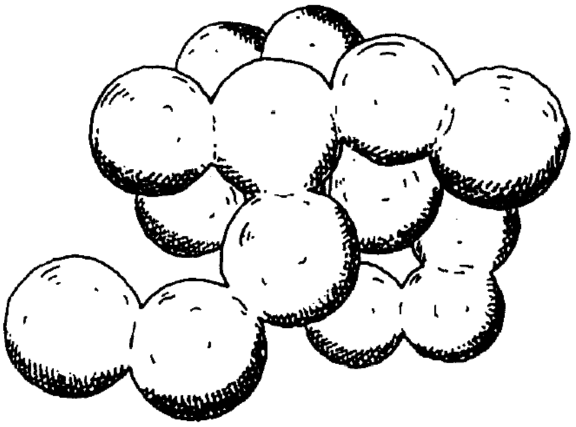

Figure 2.13 Schematic illustration of connected globular structures resulted from the spinodal decomposition with suppressed coarsening.[109,110]

3 EXPERIMENTAL

This chapter is dedicated to present the experimental information regarding the process of structural formation in crosslinked polymers by *in situ* photocrosslinking of precursors during the evaporation of the solvent. The content therefore will be arranged according to the following sequence: film-forming materials we employed, method of film preparation, morphological analysis by scanning electron microscope (SEM), and characterizations of chemical and physical properties of the resulting films by other equipment.

3.1 Materials and film preparation

The prepared composition of the photoactive precursors typically consists of a monofunctional monomer such as MMA, a difunctional crosslinker such as EGDMA, and a type I photoinitiator, DMPA (see Table 3.1). Alternatively, a commercially formulated optical resin (premixed as received), NOA65, which consists of mercapto-ester with acrylate monomer[112], was used. The former photopolymerizes *via* free radical chain growth; whereas the latter *via* free radical mediated step growth mechanism that reportedly has much faster reaction kinetics and higher O_2 tolerance.[113–115] Either precursor was then dissolved in a solvent (see Table 3.1) with designated concentrations. The precursor solutions were homogenized with a vortex mixture prior to use. All chemicals were used as received.

The photocrosslinking/evaporation process was carried out in a home-built reaction chamber (Figure 3.1). The chamber consists of a closed aluminum box containing a gas inlet and outlet, with a 2 mm-thick glass cover on the top. The glass cover contains a small hole to allow the injection of the precursor solution and can then slide to fully cover the chamber. N_2 was used to both remove O_2 that is detrimental to the conventional free-radical based photocrosslinking reaction[116,117] and to control the evaporation rate of the solvent. The flow rate of N_2 gas was controlled by a flow meter and a three-way valve, which allows purging N_2 either directly into the chamber or through a gas bubbler (to saturate with water vapor) before entering the chamber. Such design allows selectively purging dry or moist N_2 into the chamber during the UV exposure. Unless otherwise mentioned, an OmniCure UV/Visible spot curing system equipped with a notch filter whose bandgap is 320-500 nm and with a collimating kit was used to provide uniform radiation across the sample surface. The output spectrum of this curing system is shown in Figure 3.2 as specified by the manufacturer. In cases a sufficiently small intensity is needed, an optical neutral density (Edmund Optics) filter was mounted to attenuate the UV intensity. The UV output was placed ~ 10 mm away from the reaction chamber and its intensity that reached the plain of substrate was measured with a handheld radiometer (ILT1400-A, International Light Technologies).

The N_2 stream was purged for at least 5 min to saturate the reactive chamber prior to the solution deposition. Subsequently, a solution drop was deposited onto a solid substrate such as polyethylene terephthalate (PET) and glass slide by a micropipette *via* a hole on the sliding cover glass. Upon injection, the hole was moved aside to fully seal the chamber, immediately followed with UV radiation. During the process, the solution drops remained quiescent on the substrates in spite of the blowing N_2 flow. After the designated process time elapsed, the sample was taken out of the chamber and if necessary, further dried in an ambient environment for the following characterizations.

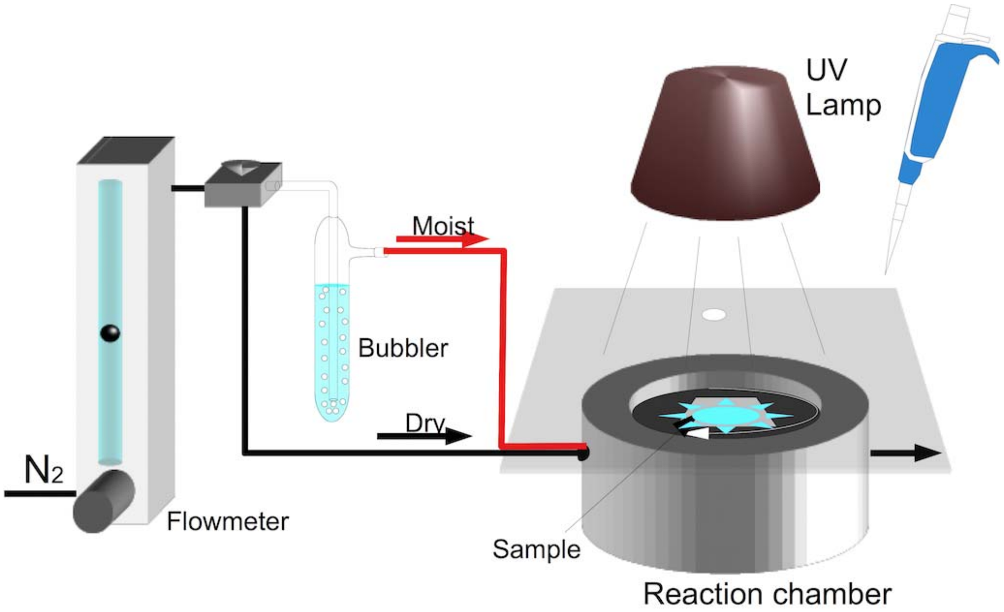

Figure 3.1 Schematic of the experimental setup for the fabrication of microstructured polymer films.

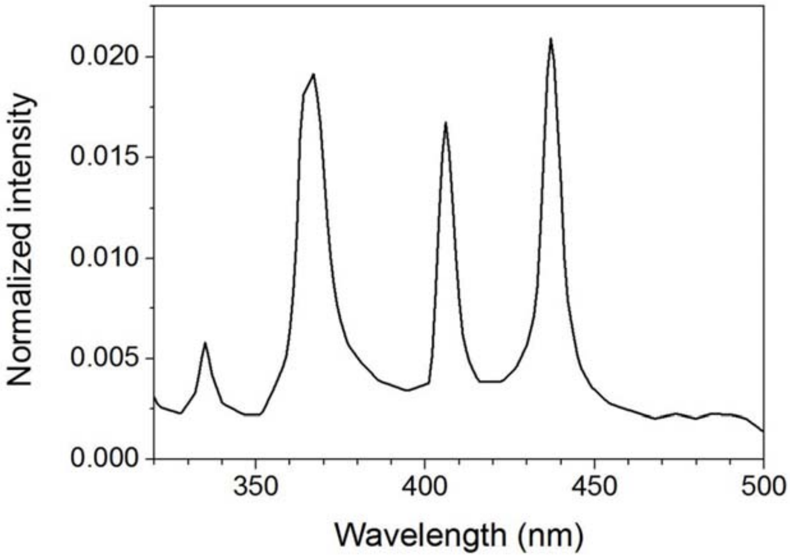

Figure 3.2 Normalized UV output spectrum of Omnicure S2000 spot curing system (with 320-500 bandpass filter) equipped with an 8 mm liquid light guide and an adjustable collimating adaptor. Raw data (without normalization) was digitized from the manufacturer's manual.

Table 3.1 Photoactive precursor solutions employed in the study

		Abbrev.	Grade	Manufacturer
photoinitiator	2,2-dimethoxy-2-phenylacetophenone	DMPA	99%	Sigma Aldrich
monomer	methyl methacrylate	MMA	99%	Aldrich
	butyl methacrylate	BMA	99%	Aldrich
	acrylic acid	AAc	99%	Aldrich
	tert-butyl acrylate	tBA	98%	Sigma Aldrich
	Styrene	/	/	Scientific Polymer
	Acrylamide	AAm	≥ 99%	Sigma
	2-hydroxyethyl methacrylate	HEMA	Ophthalmic	Polysciences
	N-isopropylacrylate	NIPAm	≥ 99%	Aldrich
crosslinker	ethylene glycol dimethacrylate	EGDMA	98%	Aldrich
	tetraethylene glycol dimethacrylate	TEGDMA	99%	PolySciences
	polyethylene glycol dimethacrylate (MW ~ 750)	PEGDMA	98%	Aldrich
commercial resin	Norland optical adhesive 65	NOA65	/	Norland Products
solvent	carbon disulfide	CS_2	ACS reagent	Sigma Aldrich
	Hexane	HEX	/	Fisher Scientific
	Acetone	/	certified ACS	Fisher Scientific
	chloroform	/	ACS spectrophotometric	Sigma Aldrich
	dichloromethane	DCM	ACS reagent	Sigma Aldrich
	tetrahydrofuran	THF	Anhydrous	Acros Organics
	Toluene	/	ACS reagent	Sigma Aldrich
	isopropanol	IPA	Certified ACS plus	Fisher Scientific

3.2 Morphological analysis of the obtained films

We were interested in the three dimensional appearance of the features that was resulted from the process. As compared to optical microscope (OM), scanning electron microscope (SEM) is more appealing to use since some of the microstructures we concerned are in size smaller than the diffraction limit of OM and the topography of the films resulting from the process and from the subsequent preparation requires sufficient depth of field. Herein, in this study, SEM has been extensively exploited for the obtained films. Three models of SEM have been employed at different stages of this study including a low vacuum scanning electron microscope (LV-SEM) (6840LV, JEOL) and two field emission scanning electron microscopes (FE-SEM) (Zeiss, Supra 60; JEOL JSM-7401F). The obtained films after removing all entrapped solvent were mounted on a SEM stub and then coated with a thin layer of gold. The cross-section of the films was prepared by either snapping samples under liquid nitrogen after soaking for sufficient amount of time or simply cutting with scissors at room temperature (RT). The obtained SEM images were then analyzed using ImageJ (National Institute of Health, USA). All reported results were the average values from multiple images taken at different regions of the sample films.

In particular, geometric parameters of the BF structured films, including perimeter, diameter, circularity, and surface coverage of the pores, and wall thickness between the pores, as well as FFT analysis were performed with ImageJ on converted binary images. Specifically, the circularity of the pores was calculated according to,

$$\text{circularity} = 4\pi \times \frac{\text{area}}{\text{perimeter}^2} \qquad \text{Eqn 3.1}$$

and equals 1, 0.907, and 0.785 in the case of a circle, hexagon, and square, respectively. Wall thickness was calculated from averaging at least 100 measurements. In addition, the degree of order was analyzed with a Voronoi polygon construction with Matlab (MathWorks) (an example is shown in Figure 3.3) and the entropy of pore packing is estimated using,[85,118,119]

$$\xi = -\sum_{m} F_m \ln F_m \qquad \text{Eqn 3.2}$$

where m is coordination number of every pore and F_m is the fraction of every coordination m. To think of two extreme cases, the boundaries of ξ can be obtained: in a defect free system having hexagonal close packing $F_6 = 1$, therefore $\xi = 0$; while, a system with a randomly distributed array of pores, $\xi = 1.71$[84,118]. Consequently, the estimated value of our BF films is $0 < \xi < 1.71$ and the smaller ξ means a more regular BF film.

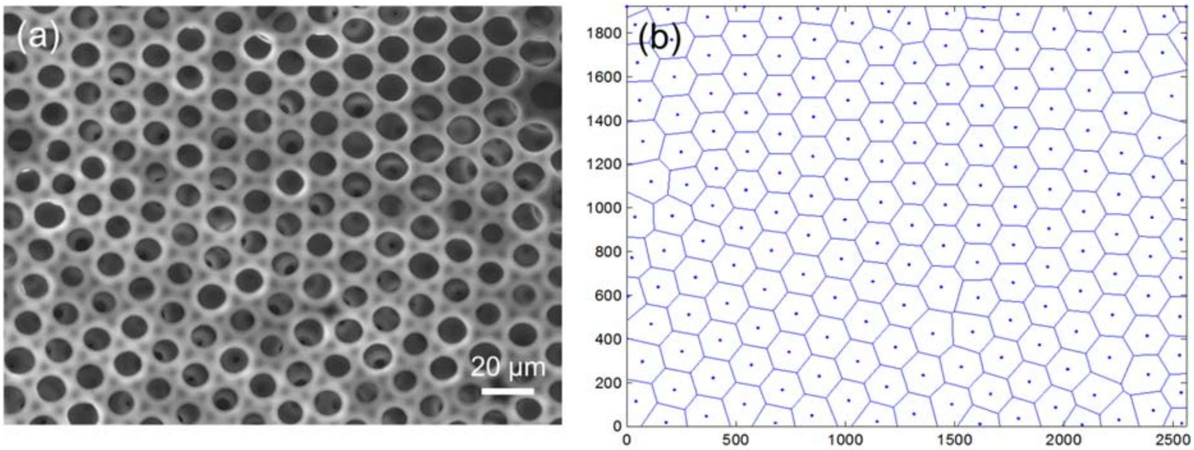

Figure 3.3 An example of constructing Voronoi polygon (b) using SEM image of BF film (a).

3.3 Characterizations of the chemical and physical properties

Attenuated total reflectance Fourier transform infrared spectroscopy (ATR-FTIR, Nicolet 4700, Thermo Scientific Corporation) was used to determine the monomer conversion during the process. On the other hand, the temperature of the solution drop during the process was monitored by a thermocouple and a data acquisition unit (Agilent 34980A). The presence of the thermocouple affected neither the spreading of the drop nor the photopolymerization process, as the exposed thermocouple tip was sufficiently small (< 1 mm, as compared to solution drop diameter of ~ 16 mm). However, it is known that the temperature within a fast evaporating solution drop is non-uniform,[69–72] as we discussed in Section 2.1.2. Therefore, the temperature monitored in this work only corresponded to central regions of the casted-drops.

3.3.1 Hierarchical films characterizations

An atomic force microscope (AFM, Bruker DI 3100) was used to examine the topography of the film surface. The measurements were performed in tapping mode under ambient conditions using silicon cantilever probes (Veeco, RTESP) with spring constants ranging between 20 and 80 N/m, as specified by the manufacturer.

Gel permeation chromatography (GPC) was used to determine the molecular weight of the PNIPAm formed and the corresponding conversion of the NIPAm monomer at different processing time. The samples were dissolved in THF (ChromAR grade, Micron Fine Chemicals) at 0.5 wt.% for the GPC measurements. The GPC consists of a Viscotek GPCmax module, a differential refractometer (VE3580) and a set of two Viscotek Viscogel columns (7.8 × 30 cm). The flow rate of the effluent through the GPC column was 1 mL/min. The GPC was calibrated with 12-monodispersed polystyrene (PS) standards prior to use.

Differential scanning calorimetry (DSC 204 F1 Phoenix, NETZSCH) was employed to (a) quantify the amount of unreacted NIPAm monomer, (b) measure the glass transition temperature (T_g) of the PNIPAm formed, and (c) determine the volume-phase transition (VPT) of the PNIPAm particles in DI water. For tasks (a) and (b), the obtained samples (after drying) were directly measured with DSC, at a scan rate of 10 °C/min. The amount of the unreacted NIPAm monomers was determined by analyzing melting enthalpy of the crystalline NIPAm monomers during the 1st heating scan. T_g of the PNIPAm was extracted from the midpoint of the endothermic stepwise change during the 2nd heating scan. For task (c), a piece of as-cast film (1.85 mg) was first equilibrated in DI water for at least 24 h. An aqueous mixture containing 9 wt.% PNIPAm was then transferred to a DSC crucible, and scanned with a heating rate of 5 °C/min. The value of VPT temperature was extracted from intersection of the baseline and the leading edge of the endothermic peak, *i.e.* as the onset of the VPT.

3.3.2 Honeycomb microporous film characterizations

Chemical degradation of the honeycomb porous films was examined by thermogravimetric analyzer (TGA7, Perkin Elmer). The crosslinked films, along with PET substrate, were characterized by TGA with temperature increased from 40 °C to 500 °C under a constant heating rate of 10 °C/min. Water contact angles (CA) on the porous films were determined with a home-built apparatus. For each measurement, 2 μL DI water was deposited by a micro-syringe onto the sample surface and the profile of the sessile droplet was immediately captured by a video camera. Five measurements across the sample surfaces were carried out, and the average values and their corresponding standard deviations were reported here.

The T_g of the porous films was determined by a nanoscale-thermal analysis (nano-TA). Detailed description of the nano-TA techniques and its application to determine T_g of supported polymer thin films can be found elsewhere.[120] Briefly, nano-TA is an AFM (Bruker DI 3100)-based nanoscale-thermal analysis technique (Anasys, Inc.) that utilizes a custom-made thermalever^{TM} probe to measure the softening temperature of a material with a spatial resolution of ~ 100 nm. In particular, the thermlever^{TM} probe is placed on top of the sample surface and the deflection of the cantilever is monitored as the temperature of probe in contact with the polymer surface increases. The T_g value is obtained as the temperature when the tip penetrated into the surface as it is softened during the glass transition, which induced a clear change in the tip deflection. All the nano-TA measurements were carried out with a heating rate of 60 °C/min. The reported T_g value for a given sample was the statistical average of five measurements at different locations across the surface. For comparison, bulk non-porous samples having identical compositions were prepared by direct photocrosslinking without solvent.[121] T_g of these samples was characterized by both nano-TA and dynamic mechanical analysis (DMA, TA Q800). The DMA measurements were performed in a strain sweep mode at 1 Hz with a static force of 0.01 N, with temperature ranging from 25 to 180 °C at a rate of 2 °C/min, and the T_g values were extracted from the peak of tangent delta plot.

4 FORMATION OF HIERARCHICAL FILM UNDER DRY N_2 FLOW

4.1 Introduction

Reaction induced phase separation (RIPS) of polymers is a process during which polymerization reaction of one component within a homogenous mixture, leads to the separation between the reacting phase and the inert phase. UV curable precursors are one classical matrix-forming system for RIPS, while the inert phase can be either organic solvents or polymers. The morphologies and physical properties of the resulting composite materials can be tailored by controlling the thermodynamic and/or kinetic factors, which has attracted broad interest from applications in liquid crystal composites[122–124], nano to micron-sized particles[125,126], foaming[127], toughening of thermosets[110,128] and porous hydrogels[129–134].

When a solvent is used as the “inert” phase, its evaporation during the RIPS is normally neglected. Most often, the domains of the organic solvent are removed after the RIPS process has completed, which can be used to create porous crosslinked polymers.[26–28] In comparison, the phase evolution of photoinduced crosslinking during simultaneous solvent evaporation has been studied scarcely. Guenthner et al. showed that RIPS in evaporative solvents can yield sparse three-dimensional networks without significant structural collapse, which is characteristic for RIPS in non-evaporative solution.[111] Therefore, the coupling between photocrosslinking and fast evaporation of the solvent may lead to a plethora of film morphologies. Understanding this process can thus open an avenue for creating unique film structures, beyond that achieved in the non-evaporative solvent, and is important for applications such as solution-based photoactive coatings.

However, the interplay between photocrosslinking and solvent evaporation brings significant challenges. Firstly, during the process, the fast evaporation of solvent at the air-surface interface generates a concentration gradient within the casted drop. Secondly, UV intensity is attenuated due to the absorption by the solution (photoinitiator, precursor, forming polymers and solvent), leading to the non-uniform polymerization rate across the solution thickness. Thirdly, the instability flow (a.k.a. temperature induced Marangoni convection) further complicates the system and is responsible for the heat and mass transfer in the lateral directions.

The goal of this chapter herein is to elaborate the mechanisms of the photocrosslinking of precursors during the fast evaporation of solvents, *via* both theoretical and systematic experimental efforts. We found that for the first time a crosslinked polymer skin layer was obtained after the process, in contrast to that occurred during the drying of non-crosslinked polymer solutions. The growth of the skin layer could be interrupted by the particle-formation due to the RIPS of the solution capped underneath the skin layer. The morphologies of both the skin layer and the particle phases depend on the parameters of the photocrosslinking/evaporation process, as examined in detail. We further show that we can use this technique to create microstructured hydrogel films from a couple of common monomers. The precursor system used allowed us to systematically examine the compositional and morphological evolutions throughout the film-forming process.

Table 4.1 Important physical properties of the solvents used in the study.[135–137]

	HEX	CS_2	acetone	chloroform	DCM	THF	toluene	IPA
Solubility parameter, δ @25 °C $(MPa)^{1/2}$	14.9	20.5	20.0	19.0	20.3	19.4	18.2	23.5
Dispersion component, δ_d $(MPa)^{1/2}$	14.9	20.5	15.5	17.8	18.2	16.8	18.0	15.8
Polar component, δ_p $(MPa)^{1/2}$	0	0	10.4	3.1	6.3	5.7	1.4	6.1
Hydrogen bonding component, δ_h $(MPa)^{1/2}$	0	0.6	7	5.7	6.1	8.0	2.0	16.4
$100f_d$	100	97	47	67	59	55	84	41
$100f_p$	0	0	32	12	21	19	7	16
$100f_h$	0	3	21	21	20	26	9	44
$100f_p + 100f_h$	0	3	53	33	41	45	16	59
Density (g/cm^3)	0.66	1.26	0.79	1.48	1.32	0.88	0.87	0.78
Molecular weight (g/mol)	86	76	58	119	85	72	92	60
Viscosity @25 °C (cP)	0.31	0.36	0.33	0.57	0.44	0.55	0.59	2.0
Boiling point (°C)	69	46	56	61	40	66	110.6	82
Vapor pressure @21 °C (mmHg)	128	309	194	169	376	133	23.2	35.1
Evaporation rate (butyl acetate = 1)	8.4	10.9	5.6	N/A	25	6.3	2.0	1.5
Heat of vaporization, H_v (cal/mol)	6880	6460	7076	7021	6715	6664	7985	9540

4.2 Material systems applicable

Table 4.2 Summary of precursor/solvent pairs examined whether they formed opacity: "Yes" indicates opacity formed, "/" indicates films were transparent upon completion of the process, "ND" indicates precursor did not dissolve in that solvent, and "NT" indicates the precursor/solvent pair was not studied. Parenthesis besides the name of monomers, if any, encloses the solubility parameter δ in unit of $(\mathrm{MPa})^{1/2}$ of corresponding polymers.[138] Experiments were conducted with a solution drop of 100 μL containing 15 vol.% precursor (precursor is a mixture of monomer and 0.6 wt.% initiator) on a cover glass under a dry N_2 flow of 1 L/min and 50 mW/cm^2 UV intensity for duration of 10 min.

		HEX	CS_2	Toluene	Chloroform	DCM	THF	Acetone	IPA
non-polar	MMA (18.3)	NT	/	/	/	/	/	/	Yes[1]
	BMA (18.4)	NT	/	/	/	/	/	/	/
	tBA	NT	/	/	/	/	/	/	/
	Styrene (22.5)	NT	/	/	/	/	/	/	/
polar	HEMA	NT	Yes[1]	Yes	/	/	/	/	/
	NIPAm (22.8)	NT	Yes	/	/	/	/	NT	NT
	AAm	NT	ND	NT	/	/	Yes	Yes	NT
	AAc	NT	Yes	Yes	Yes	Yes	/	/	/
	NOA65	Yes	Yes	/	/	/	/	/	ND

[1] the films showed a tiny opacity in the center (< 10 % surface coverage)

We here examined the precursor/solvent pairs under a process of simultaneous photopolymerization and solvent evaporation at dry N_2 flow, using the setup shown in Chapter 0 (Figure 3.1). We employed eight common solvents including HEX, CS_2, toluene, chloroform, DCM, THF, acetone, IPA. The important physical properties of these solvents were tabulated in Table 4.1. Experimentally, a 15 vol.% precursor mixture containing one of the monomer such as MMA and 0.6 wt.% DMPA (as photoinitiator) was dissolved in one of these solvents (Table 4.1), except NOA65, which was premixed when received. A drop of 100 μL homogenous solution was then pipetted onto a cover glass (22 × 22 mm) under a dry N_2 flow of 1 L/min and 50 mW/cm^2 UV intensity (320 - 500 nm). After 10 min, we stopped the process and observed whether the films resulted from the given precursor/solvent pair appeared opaque, which was indicative of the occurrence of phase separation during the process. Table 4.2 summarizes the experimental results: the pairs that showed opacity were assigned "Yes" whereas those formed transparent films were assigned "/".

From Section 2.3, it is known that the phase separation in solution undergoing simultaneous photocrosslinking and solvent evaporation may be resulted from 1) reaction rate dominating over the evaporation rate: reaction promotes phase separation (x) while evaporation suppresses ($\emptyset_1$); 2) χ-induced syneresis: the miscibility between the solvent and growing polymers reduces significantly. Herein, we first examined the influence of solvent evaporation rate on the phase separation. To quantify the degree of volatility of a solvent, we used the term, relative evaporation rate, determined from experiment, referencing to butyl acetate = 1.[139] As shown in the Table 4.1, relative evaporation rate of solvents are in the descending order of DCM > CS_2 > HEX > THF > acetone > toluene > IPA. The relative evaporation rate of chloroform is not available from the handbook, but should be comparable to acetone, and larger than toluene and IPA, because of its relatively large vapor pressure.

Judging from both HEMA and AAc, the solvent evaporation rate did not seem to be a determining factor for phase separation (Table 4.2). For example, four solvents including CS_2, toluene, chloroform and DCM were in favor of phase separation with AAc precursor. These solvents have a relative evaporation rate ranging from 2 to 25 (Table 4.1). THF and acetone have relative evaporation rate of 6.3 and 5.6 respectively, both of which are within the range, but neither underwent phase separation with AAc precursor.

We then look at the miscibility of a solution using solubility parameter δ. From Table 4.1, δ of the eight solvents is in the range of 19 – 21 (MPa)$^{1/2}$ except HEX (14.9) and IPA (23.5). We compared δ_s of a solvent to δ_p of a polymer (which, if any, is shown in the parenthesis besides the name of corresponding monomers in Table 4.2). However, the comparison results are not conclusive. First of all, the term, $(\delta_s - \delta_p)^2$, which signifies the miscibility gap between a solvent and a polymer, is almost same for almost any solvent/polymer combinations in Table 4.2. Secondly, NOA65, as example, underwent phase separation with CS_2, which has a δ close to that of DCM. Another example is AAc that phase separates with CS_2, toluene, chloroform and DCM, all of which have δ ranging from 18.2 to 20.5 (Table 4.1). However, THF and acetone both having a δ within this range did not phase separate with AAc. Clearly, it is insufficient to predict whether phase separation occurs or not based on the solubility parameter. More importantly, some solvents and monomers we studied here are somehow polar in nature. With this consideration, we thereafter resorted to Hansen solubility parameters by partitioning of the overall solubility parameter. Specifically, δ is an ensemble of dispersion component (δ_d), polar component (δ_p) and hydrogen bonding component (δ_h):

$$\delta^2 = \delta_d^2 + \delta_p^2 + \delta_h^2 \qquad \text{Eqn 4.1}$$

Furthermore, the polarity of a substance can be described by the concept of Teas parameters (a.k.a. fractional parameters), defined as:

$$f_i = \frac{\delta_i}{\delta_d + \delta_p + \delta_h} \qquad \text{Eqn 4.2}$$

where subscript i = d, p, h. Thereafter, we assigned the nonpolar contributions of a substance f_d, whereas polar contributions $f_p + f_h$. As we can see from Table 4.1, solvents like CS_2 and HEX expectedly have small $f_p + f_h$ due to their symmetric chemical structures; on the contrary, the other solvents have appreciable polarity due to the existence of strongly electronegativity atoms such as O and Cl and/or the asymmetric molecular structures.

Before we interpret the results using Hansen solubility parameters, it is worthwhile to elaborate the way we arranged Table 4.2. Firstly, we arranged the solvents in the top row of Table 4.2 in the order of increasing polarity (f_p + f_h). In terms of column arrangement, we categorized the monomers as "non-polar" and "polar". Specifically, (meth)acrylate family including tBA, MMA, BMA, altogether with styrene, is classified as category "non-polar". In contrast, hydrogel-forming monomers including HEMA, NIPAm, AAc and AAm are recognized to be polar based on the fact that they all bear polar groups such as –OH, $–NH_2$, –COOH. The last precursor, NOA65, reportedly consists of trimethylolpropane dially ether, trimethylolpropane tris thiol, isophorone diiscocyanate ester, and benzophenone photoinitiator.[140–142] The existence of –SH moiety may render NOA65 "polar". Therefore four hydrogel forming monomers and NOA65 together are grouped "polar".

Judging from the results summarized in Table 4.2, there are some interesting findings. Among the "non-polar" category, only MMA/IPA formed opaque films (surface coverage < 10 %). IPA has largest f_p + f_h among all solvents used in this study (Table 4.1). In contrast, monomers from "polar" category with nonpolar solvents formed opaque films in general. AAm is somehow exceptional: AAm only with THF and acetone, both of which are relatively polar, formed opaque films.

These interesting findings enabled us to draw a conclusion that in order to have a precursor/solvent pair to phase separate under the processing condition we specified here, a polar (nonpolar) precursor requires a nonpolar (polar) solvent. Premise must be met that the polar (nonpolar) precursor and nonpolar (polar) solvent must be miscible prior to the process in the first place. As the processing progresses rapidly, the immiscibility gap between a polar (nonpolar) precursor and a nonpolar (polar) solvent becomes more prominent, thus causing phase separation which accounts for the opacity we have seen in the as-cast films. In the following, we show detailed studies on morphological evolutions for systems that underwent phase separation during the process, including NOA65/CS_2 and NIPAm/CS_2.

4.3 Photocrosslinking-induced phase separation in NOA65/CS_2 solution: formation of skin layers and microspheres

To study the morphology of as-cast films and its dependence on casting parameters, we here used NOA65/CS_2 precursor solution as the model system. All the deposited NOA65/CS_2 solution drops were able to quickly spread over almost the entire area of the supporting glass slides (～2 cm^2), which resulted in puddle-like sessile drops, with slight curvatures in the vicinity of the three phase contact lines.[68] For a given sessile drop, the strong outward flow induced by the surface tension gradient during the solvent evaporation caused the concentrations of the precursors and/or polymers around the peripheral area to be much higher than that in the center area.[143] As a result, transparent crosslinked films were observed near the peripheral areas for all samples, as schematically shown in Figure 4.1a. In stark contrast, the solution around the central area maintained an overall low concentration of the precursors at the early stage of the process, which subsequently developed into a hierarchical morphology as illustrated in Figure 4.1a. In this study, we focus on the morphology at the central area of the films, where the photocrosslinking and mass transfer are highly coupled while the lateral mass transfer is not dominant.

As schematically illustrated in Figure 4.1a, the crosslinked NOA65 films obtained from photocrosslinking during the CS_2 evaporations were often composed of two distinctive structural features: a crosslinked dense skin layer on top of a crosslinked micron-sized particle layer. Figure 4.1b shows a representative cross-sectional SEM image of a NOA65 film, revealing such a hierarchical structure. The thickness of the skin layer was relatively uniform, and the interface between the skin layer and the particle layer appeared to be sharp (Figure 4.1b). The air-side surface of the skin layer was smooth, with an RMS roughness of less than 5 nm, according to the AFM measurements (Figure 4.1c). The thicknesses of these layers as well as the size and distribution of the particles were highly dependent on the processing conditions, which is described in detail in the following. Note that the SEM images do not reveal the overall thickness of the films (skin layer plus the microsphere layers) as some microsphere layers were left on the glass slides side when we peeled the films off.

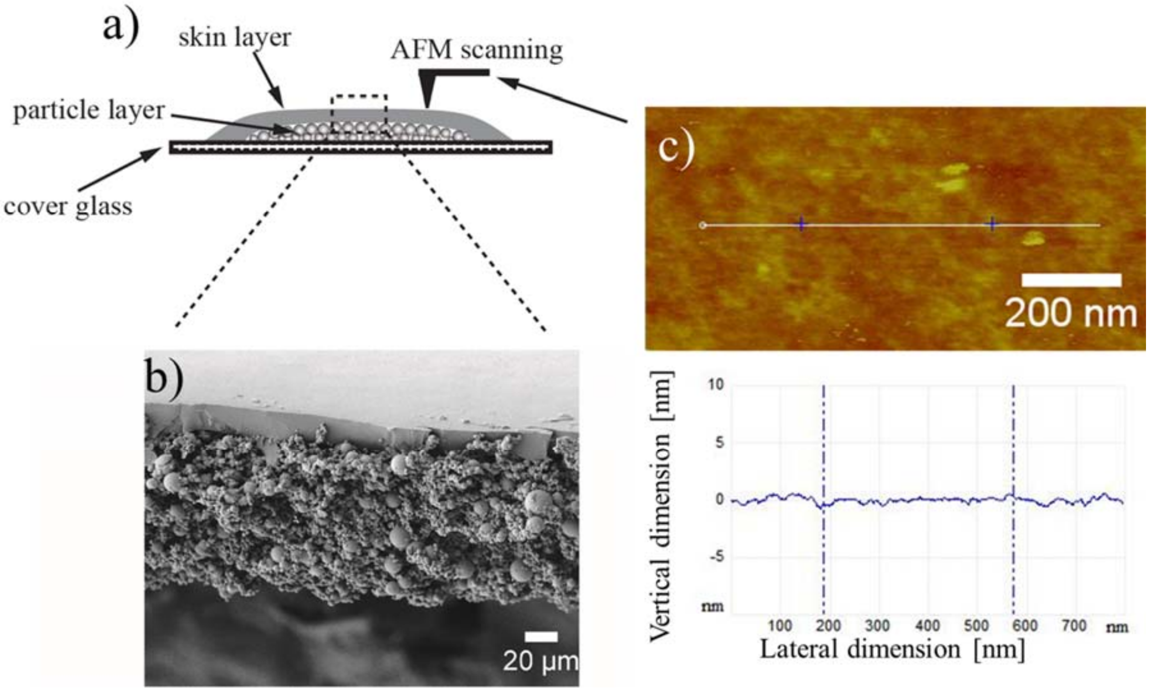

Figure 4.1 (a) Schematic illustration of the typical hierarchical structure of films formed by photocrosslinking of NOA65 during the evaporation of CS_2. (b) Representative SEM image of the cross-section of the film, showing a smooth skin layer on top of a particle layer. (c) Topographic AFM image of the skin layer (top) and the corresponding cross-sectional profile (bottom). The processing parameters for this representative sample are: 10 wt.% NOA65 in CS_2, a UV intensity of 50 mW/cm^2, and a N_2 flow rate of 1 L/min.

First, we examined the influence of the N_2 flow rate on the final morphology of the films. Figure 4.2 shows the cross-sectional images of the photocrosslinked NOA65 films obtained under N_2 flow rates ranging from 0 to 5 L/min. When the N_2 flow rate was 0, *i.e.* the evaporation of CS_2 was free convection, the skin layer was hardly discernible and appeared granular (inset of Figure 4.2a). From the top to the bottom of the film, a particulate structure was observed: the particles were tightly connected and displayed a uniform distribution in size (diameter ~ 2.5 μm). This type of a particulate morphology sometimes is referred to as "connected-globule" or "string of pearls" structure, which might have resulted from phase separation *via* a classical spinodal decomposition (SD) mechanism.[109,110]

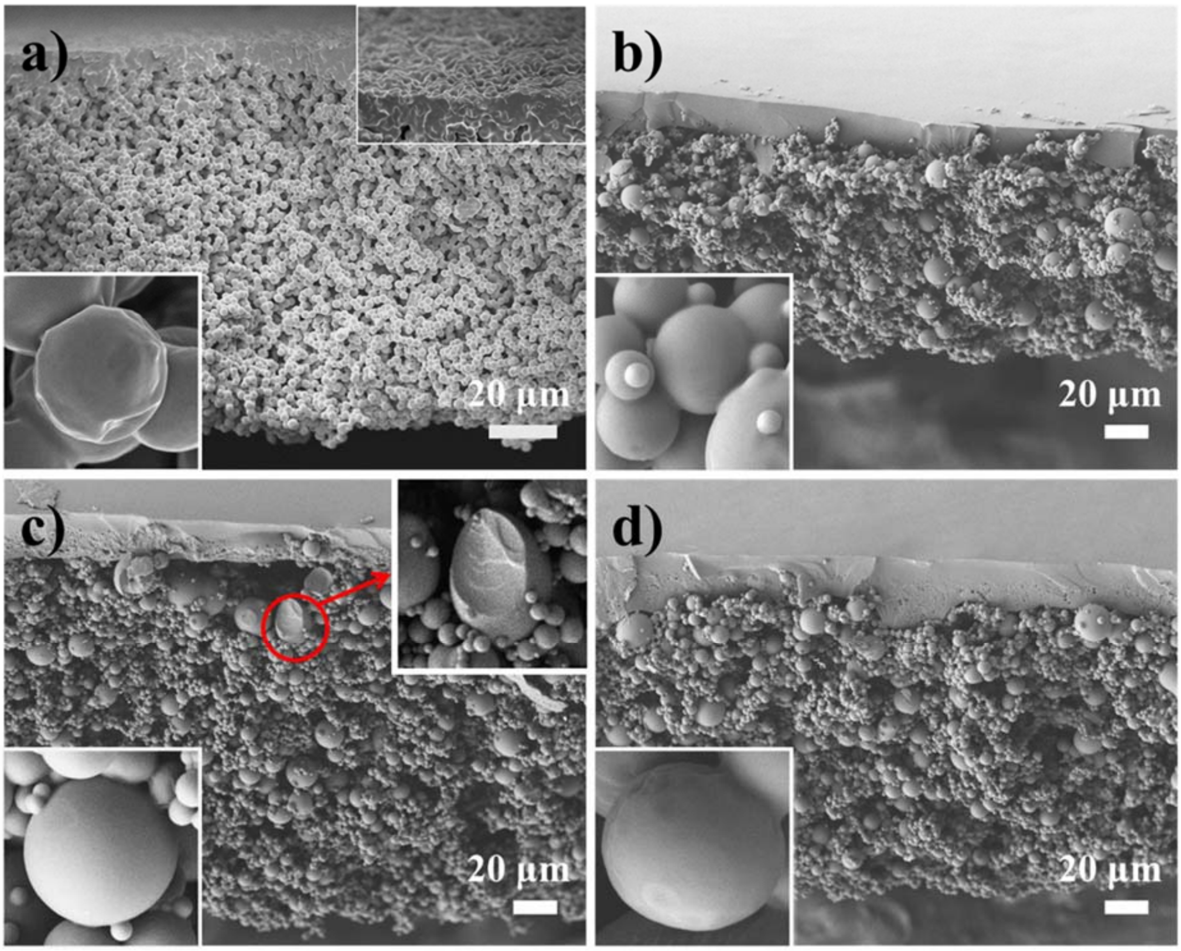

Figure 4.2 Cross-sectional SEM images of the crosslinked films prepared with 10 wt.% NOA65 in CS_2 under an UV radiation intensity of 50 mW/cm^2 at varying N_2 flow rates: (a) 0 L/min, (b) 1 L/min, (c) 3 L/min, and (d) 5 L/min. The inset in the upper right of (a) is the magnified view of the top surface of the skin layer, and of (c) is the magnified view of the cross-section of the fractured particle. The insets shown at the lower left corners of (a–d) are the magnified view of individual particles.

Once the polymerization of the precursors pushed the mixture into the unstable region of the phase diagram, concentration waves occurred spontaneously. The fastest growing wave, with a wavelength of Λ_m (a function of quench depth), became the dominant structure. Normally, one of the two continuous phases, namely polymer-rich and solvent-rich, broke into droplets due to the interfacial fluctuations. Hence, the uniform particle size was reminiscent of the dominant spinodal wavelength Λ_m. Because the particles were (partially) crosslinked during the phase separation, the subsequent coalescence of the particles was limited. Furthermore, the higher resolution SEM image (inset of Figure 4.2a) revealed that all of these particles were wrinkled. This phenomenon is consistent with the SD process. The effective concentration in both of the continuous phases kept evolving towards equilibrium, meaning that even after the phase separation, there was appreciable solvent left within the crosslinking polymer phase. The volume shrinkage of these crosslinked particles during the final evaporation of these solvents can induce such wrinkled structures.[144]

Under controlled N_2 flow rates, the structures of the films were similar, consisting of a skin layer and a particulate layer (Figure 4.2b–d), both of which were different from those found in films without N_2 flow (Figure 4.2a). The skin layers were extremely smooth on the air-surface side, and the interfaces were sharp between the skin layers and the particulate layers (Figure 4.2b–d). Correspondingly, the thickness of the skin layers increased from 17, 19 to 27 μm, as the N_2 flow rates increased from 1, 3, to 5 L/min. In contrast, the morphology of the particulate layers for films obtained under different N_2 flow rates appeared nearly identical. These microspheres were more spherical, less connected, and had broader distributions in sizes, compared with the ones in Figure 4.2a. None of these particles showed wrinkles on the outer shell (insets of Figure 4.2b–d).

All these morphological features suggest that these particles were a result of phase separation *via* the nucleation and growth (NG) mechanism. Due to the random nucleation in the solution, the crosslinked polymer particles had a broad distribution in size (sub-microns to tens of microns) caused by the difference in their nucleation time, and were not tightly connected together. The composition of these spheres, once nucleated, reached nearly the equilibrium composition, containing very low concentrations of solvent (CS_2). Thus the volume shrinkages of these particles were small when CS_2 diffused out during the complete drying of the films, which did not lead to any wrinkling of the particle shells. From the microsphere that was accidentally fractured during the cross-sectioning of the film (upper right inset of Figure 4.2c), the sphere was nearly solid, confirming that there were no pores left due to the entrapped CS_2 domains.

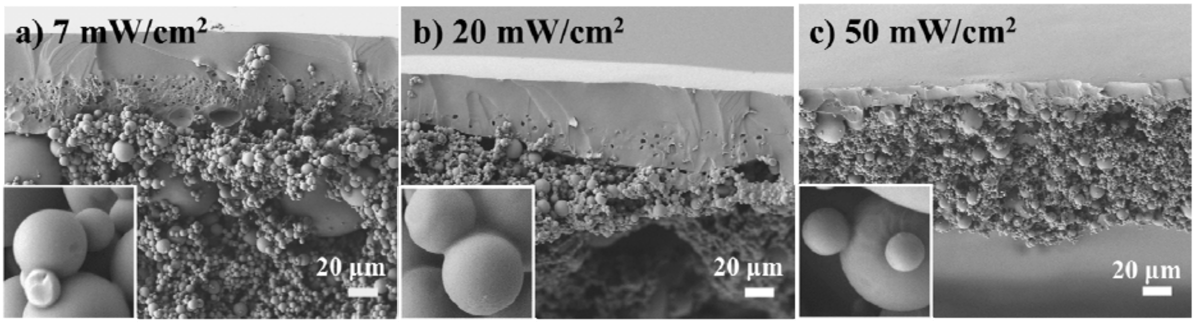

Figure 4.3 Cross-sectional SEM images of crosslinked films prepared with 10 wt.% NOA65 in CS_2 at a N_2 flow rate of 1 L/min under varying UV intensities: (a) 7 mW/cm^2, (b) 20 mW/cm^2, and (c) 50 mW/cm^2. The insets at the lower left corners of (a–c) are the magnified view of selected individual particles.

Figure 4.3 presents the SEM images of the cross-sections of the films obtained under a constant N_2 flow rate (1 L/min) but varying UV intensities. The overall film morphologies were similar to those obtained in Figure 4.2b–d. However, the variation of UV intensity had a stronger effect on the thickness of the skin layer than the N_2 flow rate, within the range studied. Specifically, the thickness of the skin layer decreased from 72, 52, to 15 μm as the intensities of the UV radiation increased from 7, 20, to 50 mW/cm^2, correspondingly. For all three samples, the particulate layers clearly showed a NG type of phase separation mechanism, similar to that discussed above. The samples obtained under 7 mW/cm^2 UV radiation intensity showed the broadest distribution in particle size among the three (Figure 4.3a).

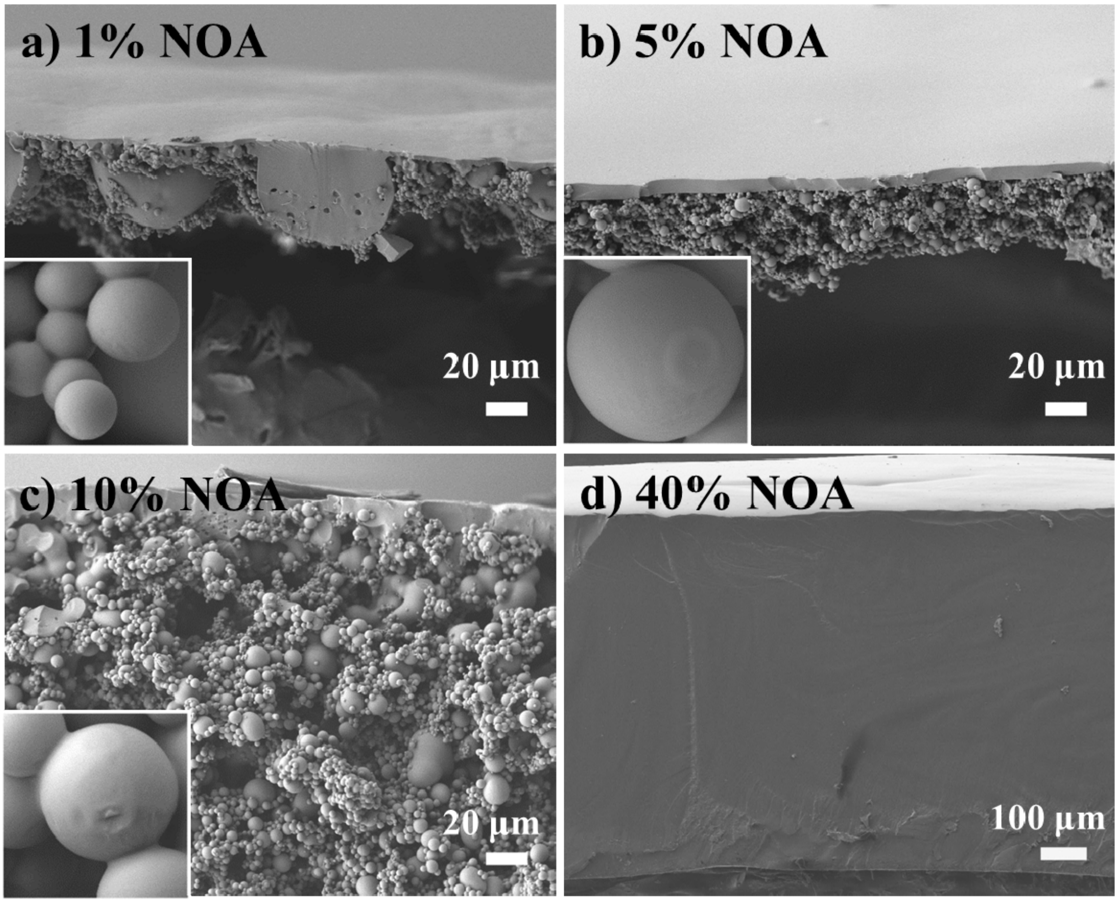

Figure 4.4 Cross-sectional SEM images of crosslinked films prepared at a N_2 flow rate of 1 L/min under a UV intensity of 50 mW/cm^2, with varying initial concentrations of NOA65: (a) 1 wt.%, (b) 5 wt.%, (c) 10 wt.%, and (d) 40 wt.%. The insets shown at the lower left corners of (a–c) are the magnified view of selected individual particles.

Figure 4.4 shows the cross-sectional morphologies of the films prepared using NOA65/CS_2 solutions containing a NOA65 weight fraction of 1 %, 5 %, 10 %, and 40 %, respectively. For 1 – 10 % NOA65/CS_2 solutions, the morphologies of the films were similar to the above-discussed ones. The skin layer thickness increased from 2.4, 6.4, to 16 μm as the concentration of NOA65 in the solution increased from 1 %, 5 % to 10 %. The structural characteristics of the microspheres indicate that the governing mechanism for forming these spheres was NG. However, for the solution containing 40 % NOA65 precursor, the photocrosslinked film showed no morphological signs of RIPS, but rather a dense crosslinked film (Figure 4.4d).

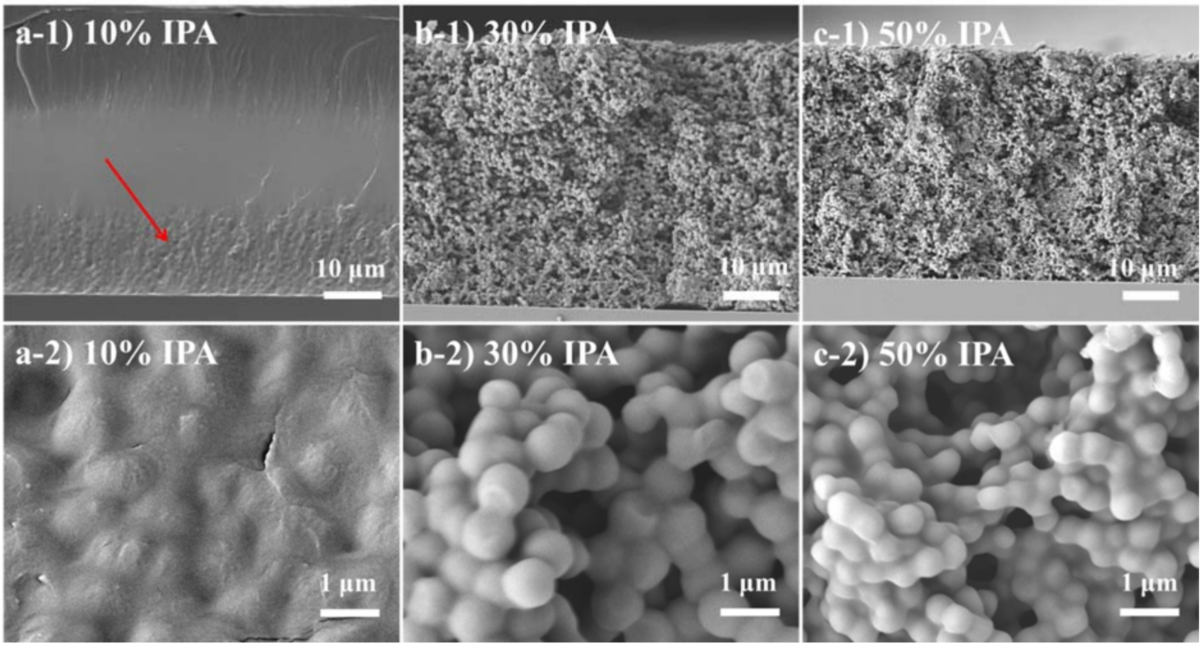

Figure 4.5 Cross-sectional SEM images of crosslinked NOA65 films, using IPA and CS_2 as co-solvents, the respective IPA to CS_2 ratios were: (a-1) 1 : 8, (b-1) 3 : 6, and (c-1) 5 : 4. (a-2), (b-2) and (c-2) are the magnified view of (a-1), (b-1), and (c-1). The NOA65 concentration was kept constant at 10 wt.%, while the UV intensity and N_2 flow rate were 50 mW/cm^2 and 1 L/min, correspondingly.

At last, we examined the co-solvent, by mixing IPA with CS_2. IPA is a non-solvent for NOA65, even prior to the polymerization,[111] which was confirmed experimentally from the phase separation in NOA65/IPA after vigorous mixing. Co-solvents containing 10 wt.%, 30 wt.%, and 50 wt.% IPA in the total solution were investigated. Note that since the NOA65 concentration was kept constant at 10 wt.%, CS_2 concentrations in the solution were 80 wt.%, 60 wt.%, and 40 wt.%, correspondingly. All the three IPA/CS_2 co-solvents were able to dissolve the NOA65 precursors. Figure 4.5 shows the cross-sectional morphology of the films obtained from photocrosslinking under the evaporation of the IPA/CS_2 co-solvents. The film that resulted from a co-solvent with 10 wt.% IPA showed that the majority of the film from the top surface was solid and dense (Figure 4.5a-1). Near the bottom (in contact with the glass substrate), some phase-separated structures were evident (indicated by the arrow in Figure 4.5a-1, and amplified in Figure 4.5a-2). However, these structures indicate that the phase separation was frozen at the early stage of the RIPS.

As the IPA composition increased to 30 wt.%, a characteristic “connected-globule” structure of crosslinked NOA65 was observed (Figure 4.5b-1 and b-2). The average diameter of the crosslinked NOA65 “particles” was ~ 890 nm. With the IPA composition in the solution further increased to 50 wt.%, a similar morphology was observed with smaller NOA65 “particles” (~ 560 nm) (Figure 4.5c-1 and c-2). For both 30 wt.% and 50 wt.% IPA, no skin layers were observed in the final films. This trend is consistent with that observed in Figure 4.2a: SD-dominated phase separation occurred in the absence of skin layers. The smaller NOA65 particle size in higher IPA concentration could result from the larger “quenching depth” in the phase diagram that predicts a smaller Λ_{m}.[109]

4.3.1 Mechanisms for the formation of the skin layer and the particulate layer

For the process of interest here, namely, photocrosslinking of precursors during the evaporation of a volatile solvent, crosslinked skin layers were observed for the first time (Figure 4.1, Figure 4.2, Figure 4.3, Figure 4.4), which remained in the final film morphology. Note that the formation of the crosslinked skin layer did not prevent the continuous evaporation of the solvent, similar to that in the non-reactive system. The solvent can readily diffuse through the swollen skin layer into the vapor phase. Here, we describe the mechanistic aspects of the skin layer formation in such a dynamic system by modifying the current theoretical descriptions of a non-crosslinked polymer solution.

Figure 4.6 illustrates the height (or thickness) of the solution puddle as a function of processing time. The quick evaporation of the solvent, aided by the convective mass transfer, cannot be balanced by the solvent diffusion and causes a steep concentration gradient of monomers (or oligomers) near the solution–air interface. Under UV radiation, this concentrated monomer layer polymerizes/crosslinks rapidly *via* the free-radical mediated step growth polymerization of NOA65[113,114], resulting in a gelled skin layer at the surface. The thickness of the layer grows from the air–solution surface downwards into the solution by coagulating/polymerizing with adjacent monomers/oligomers. In the following, we derive the growth rate of this crosslinked skin-layer.

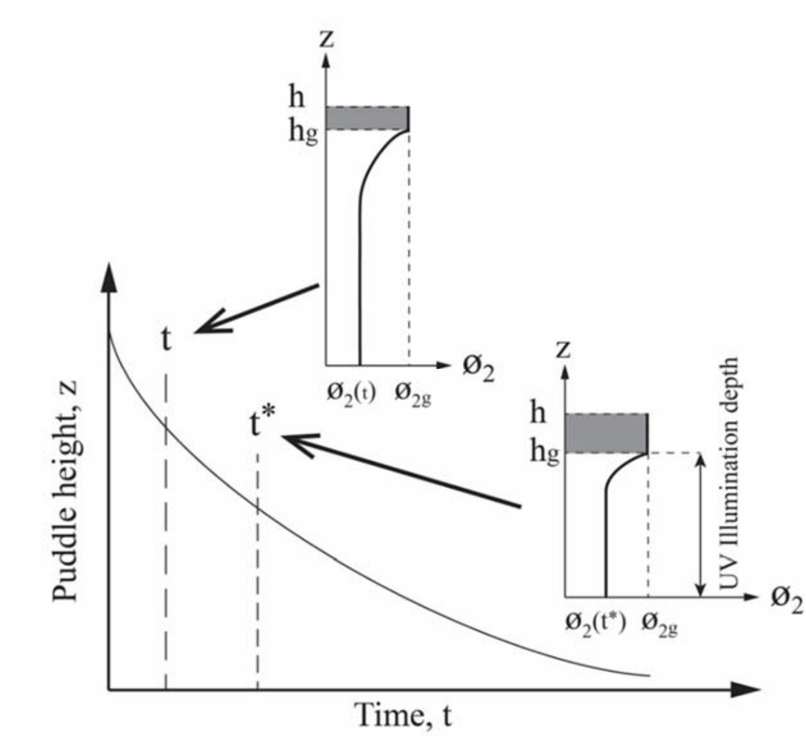

Figure 4.6 Schematic illustration of the evolution of puddle height as a function of drying time. The insets show the concentration profiles of the precursor/polymers at different times.

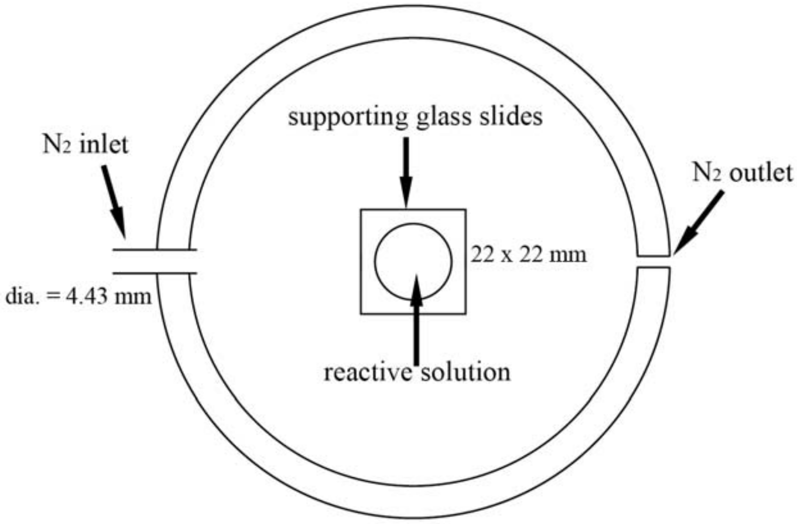

Figure 4.7 Aerial view of the reaction chamber from Figure 3.1 showing basic geometric information.

We start by examining the mass transfer at the top surface of the evaporating solution drop. The Reynolds number (Re) of the N_2 flow over the solution drop in the reaction chamber can be estimated by assuming that the N_2 flow velocity approaching the leading edge of the glass substrate was approximately equal to the inlet velocity (Figure 4.7). Re can be estimated for a given N_2 flow rate (u) used, Re = uL / ν, where L is the length of the casting glass substrate in the flow direction and ν is the kinematic viscosity. Quantitatively, Re varied between ~ 1600 and ~ 8000 for the different N_2 flow rates used, which indicates that the flow was dominantly laminar.[145] Therefore, the average mass transfer coefficient for laminar flow, $\overline{k_c}$ can be extracted from Sherwood number,

$$\mathrm{Sh_L} = \frac{\overline{k_c}L}{D_c} = 0.664\mathrm{Re}^{1/2}{S_c}^{1/3} \qquad \text{Eqn 4.3}$$

where D_c is the diffusion coefficient of CS_2 into N_2 and $S_c = \nu / D_c$ is the Schmidt number, manifested as the ratio of momentum diffusivity to mass diffusivity. Thus, $\overline{k_c}$ is a constant for a given N_2 flow rate. We can now estimate the evaporation flux of the solvent, J, by

$$J = \overline{k_c}(\psi - \psi_\infty) \qquad \text{Eqn 4.4}$$

where ψ and ψ_∞ are the concentration of solvent just above the air-solution interface and at a distance infinitely far away from solution, respectively. ψ_∞ can assume to be zero. Applying the ideal gas law, $\psi = P_g/RT$, where P_g is the partial vapor pressure of solvent right above the interface, we have

$$J = \frac{\overline{k_c} P_g}{RT} \qquad \text{Eqn 4.5}$$

Local equilibrium at the free surface of a solution drop can be established by applying Henry's law,

$$\frac{P_g}{P^*} = \emptyset_{1h} = 1 - \emptyset_{2h} \qquad \text{Eqn 4.6}$$

where P^* is the vapor pressure of the pure solvent. Note that Eqn 4.6 is valid only if initial precursor solution is dilute and a good solvent is used (Flory-Huggins interaction parameter, $\chi = 0$). For more accurate expression of local equilibrium at interface, please refer to Eqn 2.2 in Section 2.1. Regardless, Eqn 4.6 is adequate for the following discussions. Combining Eqn 4.5 and Eqn 4.6, we have,

$$J = \frac{\overline{k_c} P^*}{RT}(1 - \emptyset_{2h}) \qquad \text{Eqn 4.7}$$

Now, we can estimate the growth rate of the top skin layer, r_{skin}, by incorporating Eqn 4.7 into Doi's model,[59]

$$r_{\text{skin}} = \dot{h} - \dot{h}_g = \frac{\overline{k_c} P^*}{RT} \frac{\emptyset_{2i}(1 - \emptyset_{2g})}{\emptyset_{2g} - \emptyset_{2i}} \qquad \text{Eqn 4.8}$$

where $\dot{h}$ is the velocity of the solution surface boundary, $\dot{h}_g$ is the velocity of the interface between the remaining solution and the skin layer, $\emptyset_{2i}$ is the initial monomer volume fraction, and $\emptyset_{2g}$ is the critical monomer or polymer fraction above which the skin layer is formed. Here we assume that $\emptyset_{2g}$, P^* and T are constants for all processing conditions, although P^* is indeed a function of T that is also dependent on the varying external airflow.[36]

In non-crosslinked polymer solution, the growth of the skin layer continues until the entire film turns into a gelled state, resulting in a uniform dried film. The skin layer cannot be extracted, because once the evaporation of the solvent is stopped, the skin layer will be re-dissolved. However, for the photocrosslinking of monomers during the solvent evaporation, the skin layer growth can be interrupted, and the skin layer be obtained without the re-dissolution due to the crosslinking. Here, the process that limits the growth of the skin layer is the RIPS of the remaining solution capped underneath the skin layer, as schematically drawn in Figure 4.6.

The instantaneous thermodynamics of the reacting solution can be expressed as,[106,107]

$$\begin{aligned}\frac{\Delta\mu_1}{RT} = \ln a_1 = \ln(1-\emptyset_2) + \emptyset_2\left(1-\frac{1}{x}\right) + \chi\emptyset_2^2 \\ + v_e\bar{V}_1\left(A(\emptyset_{2n})^{2/3}\emptyset_2^{1/3} - B\emptyset_2\right)\end{aligned} \qquad \text{Eqn 4.9}$$

where $\Delta\mu_1$ is the chemical potential change of solvent after mixing, a_1 is the activity of the solvent, $\emptyset_{2n}$ equals to the volume fraction of the polymer at network formation, x is the ratio of molar volumes of the polymers to solvent, v_e is the concentration of elastically active network chains in a volume unit, $\bar{V}$ is the molar volume of the solvent, and A and B are front factors depending on the specific network models. Note that the last term in Eqn 4.9 only contributes to the solvent activity when the three dimensional network has already formed. Eqn 4.9 reveals $\emptyset_2$ that negatively contributes to the change of solvent activity, whereas x positively.

All the organic components in the solution (solvent, precursors, and polymers formed) absorbed UV radiation and therefore UV intensity attenuated as moving deeper in the solution.[146–148] At the early stage of the evaporation, the top surface of the solution has the largest initiation rate, which corresponds to the largest intensity. For this thin region near the top surface, the increase in a_1 due to the molecular buildup (x) was balanced by a rapid mass loss of solvent due to the evaporation ($\emptyset_2$). Therefore, no phase separation took place, and a gelled skin layer was formed. In other words, as the polymerization moved the phase diagram up, the fast evaporation of the solvent kept the effective concentration increased and remained in the one-phase region. As mentioned earlier, at the peripheral region of the deposited droplet, the crosslinked films obtained were also transparent, as a result of the significantly high concentration of monomers/polymers due to the strong outward flow.

Once the skin layer formed, the evaporation rate in the bulk solution was slowed down, meaning that the solution capped beneath the skin layer did not have a strong concentration gradient (Figure 4.6).[62,66,67] During this stage, the skin layer kept growing and the particulate-morphology started to form *via* the NG. The UV radiation induced a crosslinking reaction in the entire capped solution (Figure 4.6). In this case, the increase of molecular weight (x) dominated the mixing free energy of the system, as $\emptyset_2$ remained low, which caused a net gain of solvent activity (Eqn 4.9). In other words, polymerization moved the phase diagram of the solution up, while the overall concentration was kept rather constant. Furthermore, the evaporation of the solvent caused the temperature of the solution to drop appreciably. Due to both the photo-crosslinking reaction and the cooling effect of the solvent evaporation, RIPS occurred within the solution entrapped by the skin layer and led to the observed particulate layers. It appears that for all the samples that formed the skin layer, NG was the dominant mechanism for the RIPS.

Most significantly, the RIPS in the capped solution effectively imposes a finite time, t^*, to the skin layer growth, which determines the thickness (b) of the crosslinked skin layer,

$$\int_0^{t^*} r_{\text{skin}}\,\mathrm{d}t = \frac{\overline{k_c}P^*}{RT}\frac{\emptyset_{2i}\left(1-\emptyset_{2g}\right)}{\emptyset_{2g}-\emptyset_{2i}}t^* \qquad \text{Eqn 4.10}$$

t^* here is experimentally determined by observing the onset time of opacity which is an indication of phase separation.

Therefore, the formation of the hierarchical structure was dictated by the competition between solvent evaporation and RIPS induced by photocrosslinking. Dayal and Kyu reported that by controlling the relative rates of solution evaporation to phase separation in polymer solution, fiber morphologies including skin-core, uniform fiber surface with phase separated core, and porous fiber can be readily obtained.[149] In the current system, RIPS is used to limit the skin layer thickness rather than the traditional phase separation. In the following, we use the theoretical framework obtained in Eqn 4.10 to elaborate the influence of processing parameters on the different film morphologies observed in Figure 4.2, Figure 4.3 and Figure 4.4.

A higher N_2 flow rate leads to a larger $\overline{k_c}$, which in turn produces a higher growth rate of skin layer (Eqn 4.8). Experimentally, we observed t^* is almost similar (~ 5 s) for all N_2 flow rates. As a result, skin layer thickness increases with increase of N_2 flowrate (Eqn 4.10), which was in a good agreement with experimental results (Figure 4.2). When the N_2 flow rate is zero, the concentration gradient at the solution surface is low, *i.e.* diffusion of solvent can more or less balance the loss of solvent caused by evaporation. Therefore, effectively, no skin layer is formed. Instead, the overall concentration of the puddle remains rather homogeneous and increases over time. Finally, RIPS of the entire solution gave rise to the connected-globule morphology (Figure 4.2a). Studies by Sharma *et al.* have shown that the temperature of the solution decreases with the decrease of the evaporation rate, counterintuitively.[36] Therefore, the phase separation of the colder solution without N_2 flow is more likely to occur in the unstable region (the SD mechanism), while that of the other solutions under N_2 flow occur in the metastable region (the NG mechanism).

At a fixed N_2 flow rate (1 L/min), the growth rate of the skin layer of a given solution is constant (Eqn 4.8), and the thickness of the skin layer is thus dependent on the growth time, t^*. With the increase of UV intensity, we observed a reduced t^* (~ 5 s at ~ 50 mW/cm^2 vs. ~ 35 s at ~ 6 mW/cm^2), which could be attributed to increased polymerization/crosslinking rate in the trapped solution. Hence, the skin layer thickness decreases with the increase of UV intensity according to Eqn 4.10, which was indeed experimentally observed (Figure 4.3).

At both constant N_2 flow rate (1 L/min) and UV intensity (~ 50 mW/cm^2), the skin layer formation also depends on the initial concentration of the precursors. Eqn 4.8 clearly predicts that an increase in $\emptyset_{2i}$ results in an increase of growth rate of the skin layer, in the range of $0 < \emptyset_{2i} < \emptyset_{2g}$. Furthermore, t^* was experimentally found to be similar with different $\emptyset_{2i}$ (~ 5s). Both factors suggest that an increase of the initial precursor concentration would lead to an increase in skin layer thickness (Eqn 4.10). This predication was again consistent with the experimental findings (Figure 4.4). For the 40 % NOA65 solution, no phase separated structure was observed throughout the film, suggesting that the solution capped beneath the skin layer did not enter the two-phase region of the phase diagram, due to its high concentration.

4.4 Kinetic study of the process using NIPAm/CS_2 precursor solution: compositional and morphological evolutions

Understanding the kinetics of the fabrication process is crucial for desired fabrication of polymer structure *via* the method of simultaneous photocrosslinking reaction and solvent evaporation. To this end, we studied the kinetics of processing regarding the compositional and morphological evolutions under experimental conditions. Figure 4.8b shows the final cross-sectional morphology of the films prepared from a NOA65/CS_2 solution: a ~ 17 μm thick dense skin layer atop of a particulate layer. Such morphology was already developed after 30 s (Figure

4.8a), showing similar skin layer thickness and size/distribution of the particles. This fast structural formation is attributed to the fast reaction rate of the NOA65 systems. Guenthner et al., observed fast phase separation (~ 20 s) of NOA81 in the co-solvents of acetone/isopropanol, regardless of the mixing ratio of the two components.[111] Unfortunately, NOA65 precursors are not ideal candidate, both due to the proprietary chemistry and the fast reaction rate mentioned above. We therefore try to find an alternative solution by revisiting the results in Table 4.2.

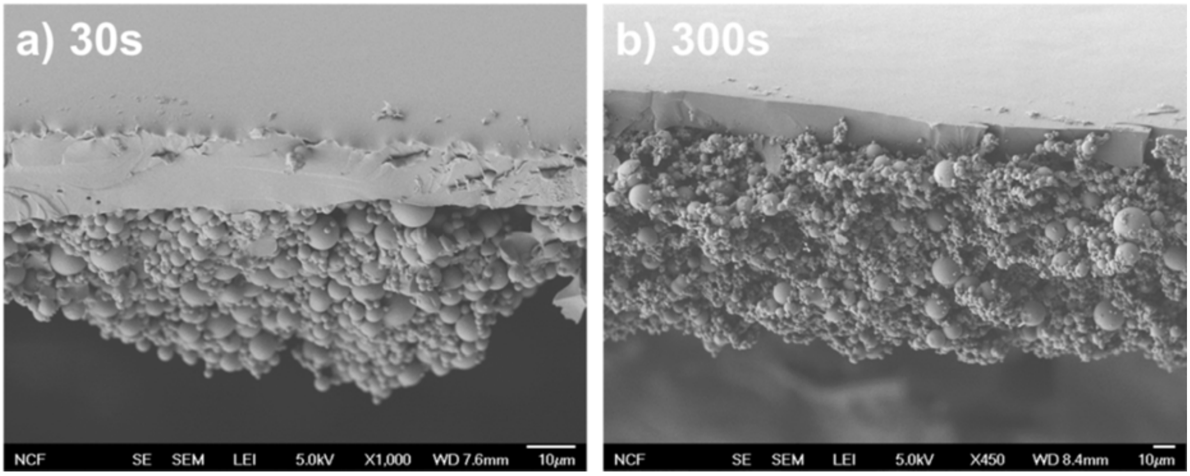

Figure 4.8 Cross-sectional SEM images of the NOA65 films, prepared using 10 wt.% NOA65/CS_2 solution at a N_2 flowrate of 1 L/min under UV intensity of ~ 50 mW/cm^2 after (a) 30 s, and (b) 300 s processing time.

Figure 4.9 presents the cross-sectional morphology of the films obtained from NIPAm/CS_2 precursor solution after 300 s, showing the similar skin layer/particulate morphology as that of NOA65/CS_2 system. The transition regions between the skin layers and the particulate layers appeared reasonably sharp (Figure 4.9a). The particles were spherical and uniform with diameters in the range of 1 - 3 μm (Figure 4.9b). For this system, this particulate morphology was likely a result of the SD of the precursor solution capped underneath the skin layer. Overall, the film morphology of PNIPAm solution is similar to that of NOA65. Therefore, in the following, NIPAm/CS_2 precursor system is used as a model solution to elaborate the compositional and morphological evolutions of the fabrication process.

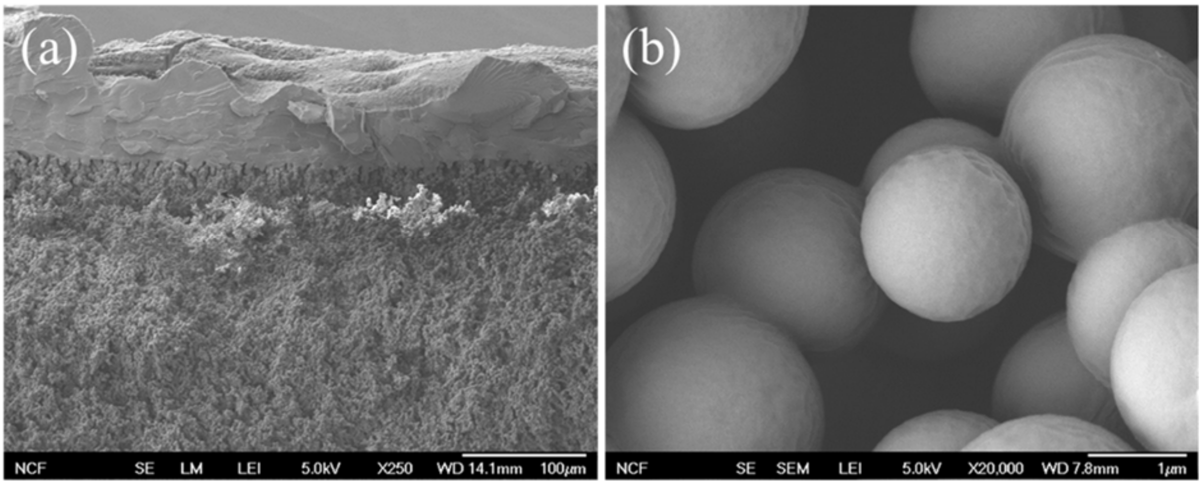

Figure 4.9 Cross-sectional SEM images of the films obtained from 20 wt.% precursor containing NIPAm/PEGDMA/DMPA in CS_2. (b) is a magnified view of the particulate layer in (a). The weight ratio of NIPAm to PEGDMA was 40:1, and DMPA was 0.6 wt.% of the precursor. Films were obtained after 300 s in a N_2 flowrate of 1 L/min under UV intensity of ~ 50 mW/cm^2.

Figure 4.10a shows the video images of the NIPAm/CS_2 solution drop at varying processing time. Within the first 5 s upon UV radiation, small pieces of solid (flake)-like films appeared at the surface of the drop, indicating the formation of pieces of the PNIPAm skin layer. The surface of the solution drop was almost entirely covered by the skin layer by ~ 30 s, and the solution drop became opaque by ~ 60 s, indicating significant phase separation within the skin-layer capped solution. The overall appearance of the film remained similar after ~ 90 s.

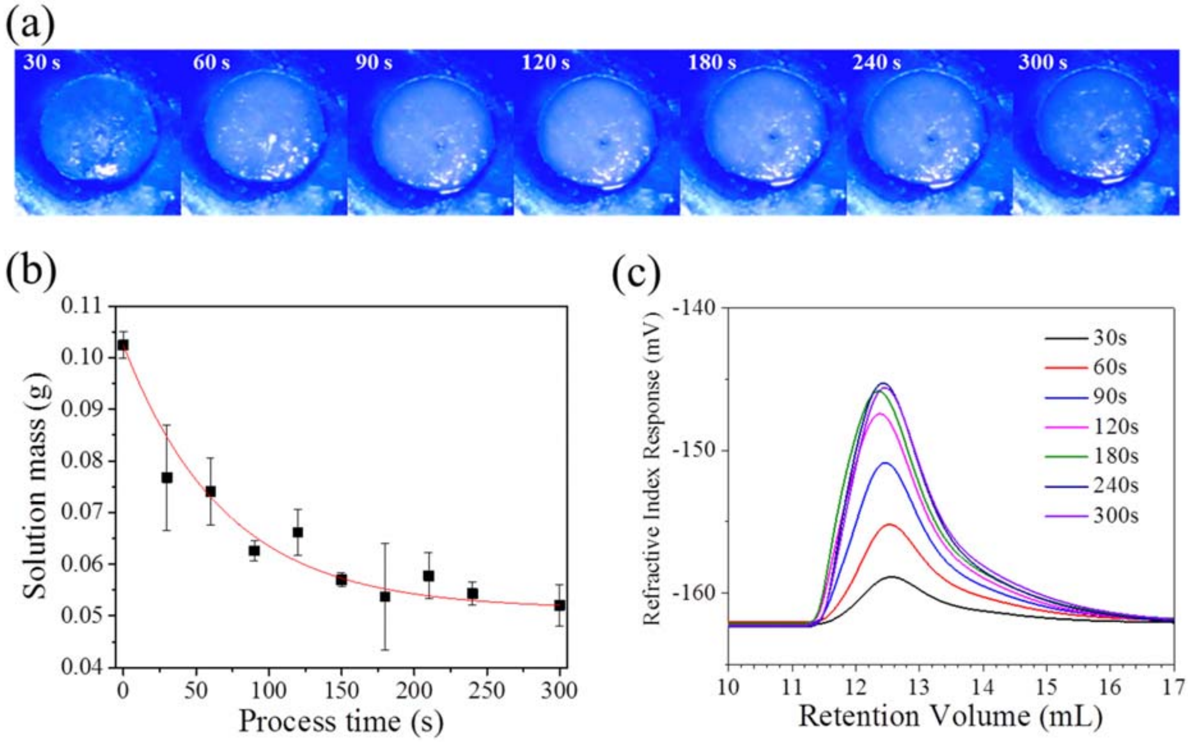

Figure 4.10 a) Video images of a 20 wt.% NIPAm/CS_2 solution, cast at a N_2 flowrate of 1 L/min under UV intensity of ~ 50 mW/cm^2, at different processing time as marked. The diameter of the drop was ~ 16 mm. b) Solution mass, measured *ex situ* after stopping the process at different time. The error bars represent standard deviation from three replicates. c) GPC measurements of the samples (without the crosslinker) obtained after different processing time.

Figure 4.10b presents the solution mass as a function of processing time, showing the evaporative mass loss of CS_2. The solution mass was obtained, *ex situ*, by weighing the solution immediately after stopping the process at a given time (e.g. 30 s). Overall, the mass of the solution drop decreases exponentially, similar to that observed during the drying of a polymer solution.[36,66] At the early stage (0 – 30 s, Figure 4.10b), diffusion of the solvent molecules in the solution is fast, and the mass transfer at the solution/vapor interface is the rate-limiting step. As the solution concentrates, particularly near the surface of the solution drop, the transport of the solvent to the solution surface becomes the rate-limiting step, which causes a significant slowdown of the evaporation.[60] Combining the video images and the mass loss, it appears that skin-layer formed up to ~ 60 s during the fast evaporation of CS_2, and afterwards appreciable phase separation occurred within the capped solution which prevented the further thickening of the skin layer. From Figure 4.10b, even after 300 s, there was ~ 48.6 wt.% solvent remained in the as-cast film, presumably capped under the skin layer.

To understand the polymerization/phase separation kinetics, molecular weight of the polymers in the samples after varying processing time was determined by GPC. Note that the NIPAm system used here did not contain any crosslinker (PEGDMA) as required by the GPC measurements, which otherwise should have similar polymerization characteristics as the ones did contain PEGDMA (the ratio of PEGDMA/NIPAm was 1:40). Figure 4.10c presents the GPC elution graphs for samples with varying processing time. For all the samples, the molecular weight of the PNIPAm, indicated by the elution volumes corresponding to the peaks in Figure 4.10c, were similar. Based on the PS-standard calibration, the number average molecular weight of the PNIPAm was ($\overline{M}_N$) = 20,900 g/mol, with a polydispersity index (PDI) = 2.5. As summarized elsewhere[150], PNIPAm polymerized *via* thermal initiation in both aqueous and organic solvents have weight-averaged molecular weight ranging from 10^4 to 10^7 g/mol. The molecular weight of the PNIPAm obtained using this method falls into the lower bound of this range.

The integral response (peak area) of an elution peak is given by, $W = H \times (\mathrm{d}n/\mathrm{d}c) \times c$, where H is refractometer constant, $(\mathrm{d}n/\mathrm{d}c)$ is the refractive index increment that is chain length dependent, and c is the polymer concentration in THF.[151,152] As the molecular weight of the PNIPAm obtained at different processing time was identical (Figure 4.10c), $(\mathrm{d}n/\mathrm{d}c)$ remains invariant. Thus, $W_i/W_j = c_i/c_j$, where i and j denote different samples. Furthermore, assuming 100 % conversion at 300 s, the monomer conversion as a function of processing time was thus obtained. It is worth noting that the conversion we calculated based on GPC peak areas is a relative value and higher accuracy is possible to achieve (*i.e.* using a tracer in the eluent as a normalizing reference). As summarized in Figure 4.11b, the monomer conversion increases with processing time and becomes invariant after ~ 180 s.

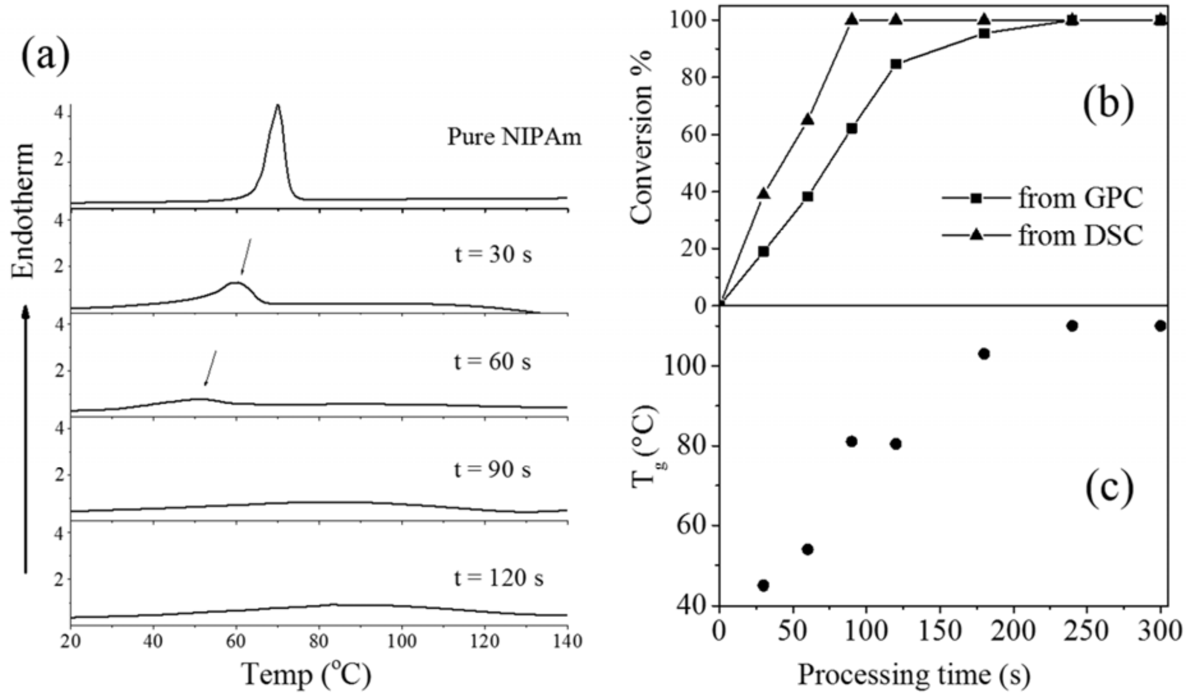

Figure 4.11 (a) DSC curves for samples obtained at varying processing time. (b) Monomer conversion as a function of process time, obtained from GPC (squares) shown in Figure 4.10c and DSC measurement (triangles) shown in a). Both methods assume conversion at 300 s was 100 %. (c) T_g of samples obtained from the midpoint of the endothermic stepwise change in the 2^{nd} heating scan of DSC.

The monomer conversion can also be estimated by DSC measurements with the samples obtained after different processing time. Note that the during the DSC scan, remaining NIPAm monomers can further polymerize upon heating and/or disperse into the PNIPAm. Therefore, only the first heating scan was used for analyzing the monomer content. As shown in Figure 4.11a, pure NIPAm monomer shows a melting temperature T_m = 65 °C with a melting enthalpy of 137.4 J/g. For the samples obtained after 30 s and 60 s, melting of residual NIPAm monomers was observed at 51 and 30.7 °C, with a melting enthalpy of 82.8 J/g and 47.5 J/g, correspondingly. Both the broadening of the melting peak and melting point depression indicate the increase of impurity (PNIPAm) in the crystalline NIPAm domain. From the melting enthalpy, the monomer conversion was estimated to be ~ 61 % and 35 % for the samples obtained after 30 s and 60 s (Figure 4.11b). For all other samples, no melting transitions were detected from DSC. Clearly, DSC only detected the crystalline portions of the remaining NIPAm, and thus overestimated the conversion of the monomer, as shown in Figure 4.11b.

Figure 4.11c shows that the T_g of the PNIPAm, obtained from the 2nd heating scan of the DSC measurements, increased with the increase of processing time and reached asymptotic value of ~ 110 °C, which was slightly lower than the reported T_g value (135 - 144 °C) of PNIPAm.[153–156] After "post-curing" in a vacuum oven at 70 °C for 4 h, the T_g of the as-cast film (300 s sample) increased from 110 °C to 132.5 °C, which could be attributed to the reaction of residual carbon-carbon double bonds and/or removal of residual CS_2. The increase of T_g with the processing time was associated with the decrease of unreacted monomer (a plasticizer for the polymer) within the sample, as revealed from the monomer conversion.

Figure 4.12a shows the ATR-FTIR spectra of the samples at varying processing time. Because the calculated penetration depth of the ATR-FTIR was about 1-5 μm in the wavelength region of interest, the IR spectra shown in Figure 4.12a were mostly contributed from the skin layer. From Figure 4.12a, the signal of the C=C bond at ~ 1620 cm^{-1} decreased with processing time, but remained visible even for the 120 s sample, which indicates the presence of NIPAm monomers within or in the vicinity of the skin layer. Because of the miscibility of these NIPAm monomers with the PNIPAm, DSC could not detect their presence even after 60 s (Figure 4.11a).

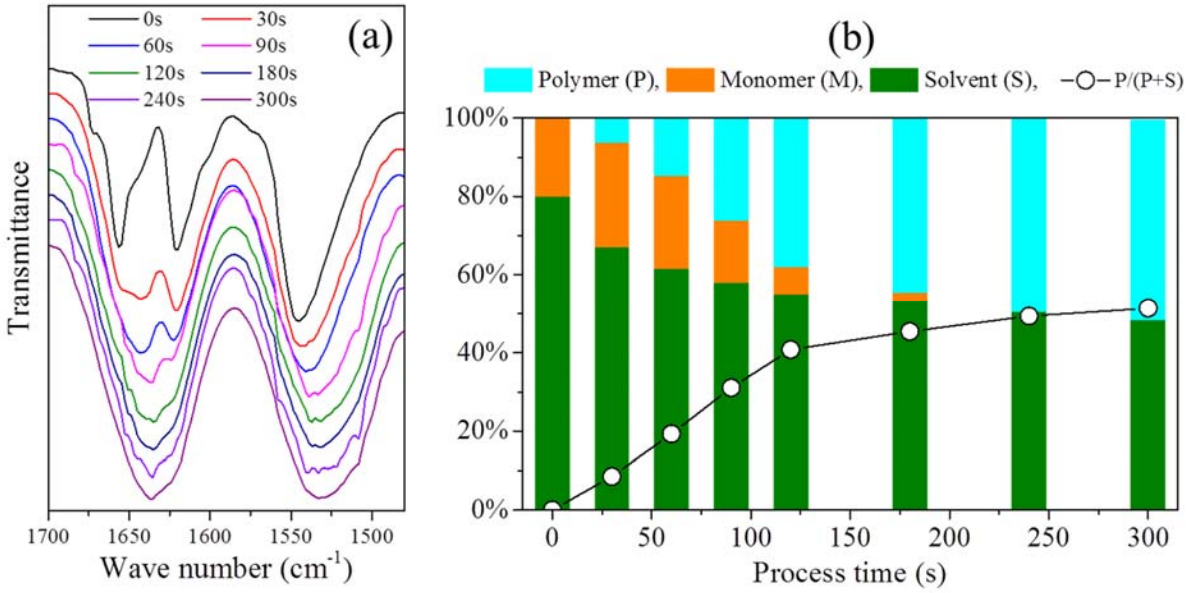

Figure 4.12 a) ATR-FTIR spectra of the samples obtained with different processing time. b) Evolution of the effective composition (monomer, polymer, and solvent) of the solution drop, obtained from the Figure 4.10b and Figure 4.11b

Combining Figure 4.10b and Figure 4.11b, the average composition of the solution drop as a function of processing time can be extracted, as shown in Figure 4.12b. The effective composition allows us to estimate the total enthalpy within the solution drop, by ignoring the dynamics associated with the respective processes. The evaporation enthalpy (ΔH_v) of CS_2 is ~ 6.5 kcal/mol[135], while the polymerization enthalpy (ΔH_c) of NIPAm (PEGDMA is negligible) is ~ 19.8 kcal/mol[157]. As shown in Figure 4.13a, for a 100 µL of 20 wt.% NIPAm/CS_2 solution used in this work, the cooling effect caused by the CS_2 evaporation is roughly balanced by the polymerization enthalpy, particularly after ~ 120 s. The temperature within the solution drop (Figure 4.13b), measured by a single probe at the center of the solution drop, showed a minimum of 6.7 °C at ~ 8 s, after which the temperature rose up quickly. At the very early stage, the fast evaporation of CS_2 caused appreciable cooling and a concentration gradient of monomers at the solution surface, which quickly polymerized into a skin layer (Figure 4.10a). In addition, from Figure 4.13b, the phase separation of the capped NIPAm/CS_2 occurred around at around 18 – 23

°C. The solubility of linear PNIPAm in CS_2 within the temperature range shown in Figure 4.13b was examined using a PNIPAm with a $\overline{M}_N$ = 15,525 g/mol and with a PDI =2.2, which was synthesized according to ref.[158]. This molecular weight is slightly lower than that obtained *via* casting (Figure 4.10c). From 4 – 40 °C, PNIPAm/CS_2 systems with composition of 1 %, 5 %, 10 % and 20 % (by weight) were all immiscible.

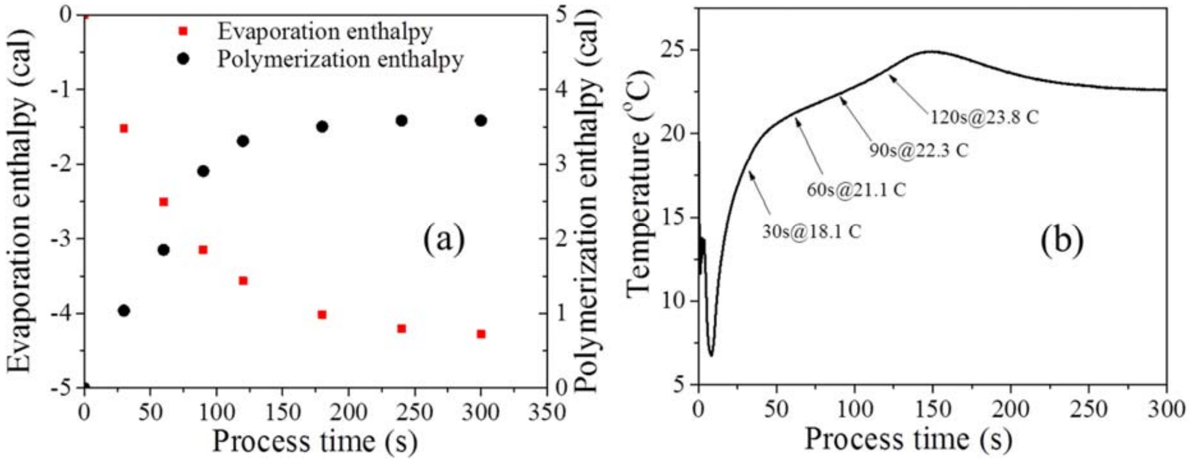

Figure 4.13 a) Enthalpy associated with CS_2 evaporation and NIPAm polymerization, and b) solution temperature as a function of process time.

A detailed picture of morphological evolution of NIPAm/CS_2 solution was presented as follows (Figure 4.14). Immediately after the process started, the fast evaporation of solvent led to a gradient of monomer concentration at the drop surface, which quickly polymerized into a skin layer. By ~ 20 – 30 s, an almost complete surface coverage had been achieved, followed by a reduced evaporation rate within the capped solution, which turned into a particulate layer since 30 s, and stopped the growth of the skin layer. After ~ 180 s, high conversion of NIPAm monomer was achieved. The solvent (CS_2) rich-domain formed during the RIPS remained underneath the skin layer, even after 300 s when all the polymerization was almost completed. Due to the low solubility of PNIPAm in CS_2 and some low degree of crosslinking, the hierarchical morphology formed during this process was maintained throughout the process.

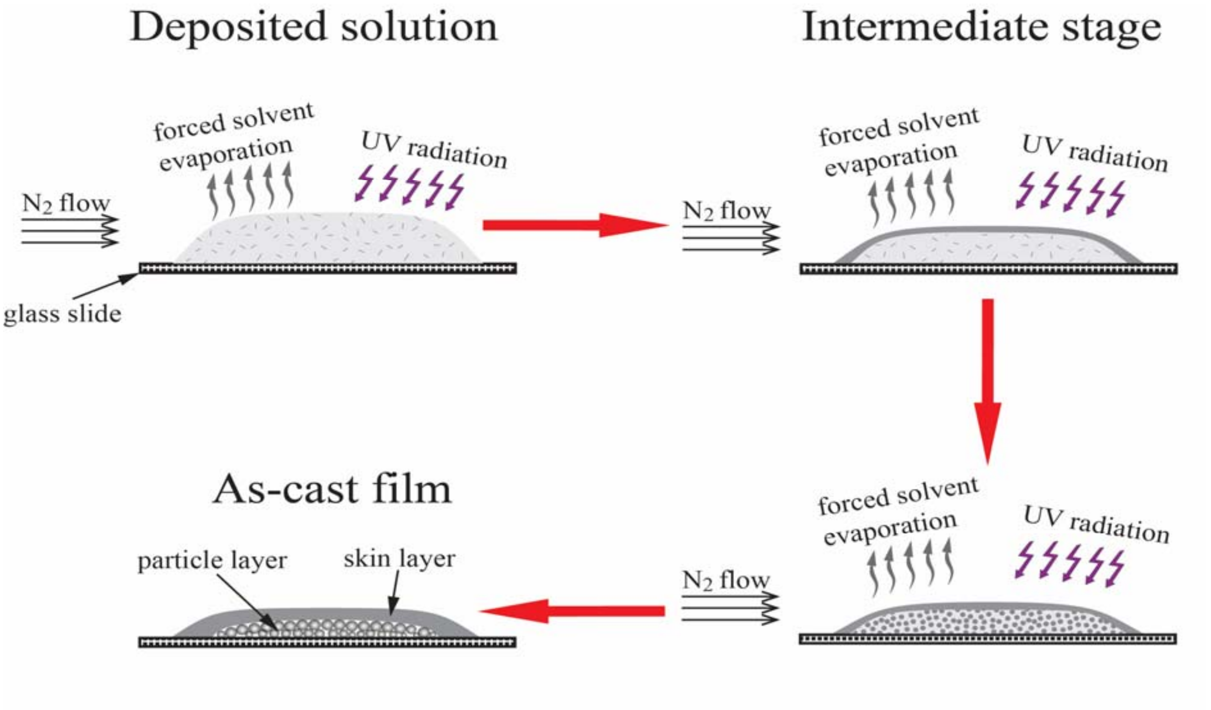

Figure 4.14 Schematic illustration of morphological evolution of a NIPAm/CS_2 solution.

The kinetic study above suggests the final film morphology is dictated by the interplay between two processes, namely photopolymerization reaction and solvent evaporation. In the following, we show that changing kinetics of one of the processes can indeed alter the film morphology. We use same NIPAm/CS_2 precursor solution but with addition of a small fraction of UV absorber, Tinuvin 328 (T328, Ciba Specialty Chemicals). We believe the reaction kinetics will be greatly slowed down while evaporation rate remains same. Figure 4.15 shows the monomer conversion of precursor solutions with and without T328 as a function of processing time, by measuring the crystalline peak areas of samples using DSC, which is same as what we have done in Figure 4.11. Apparently, the addition of small fraction of T328 (0.08 wt.%) can significantly retard the reaction (black square), *i.e.* even at 900s conversion was still not 100% and there was discernable crystalline peak in the first DSC scan (image not shown), as compared to the conversion of precursor solution without T328 (red circle). On the other hand, Gayla et al.

reported that the presence of a small dosage of T328 in the precursor solution lead to the limited UV penetration depth.[159] This implies that in our case UV may be unable to illuminate the whole thickness of solution with T328 in the beginning; thus the reaction may take place layer by layer from top to bottom until the completion of the process.

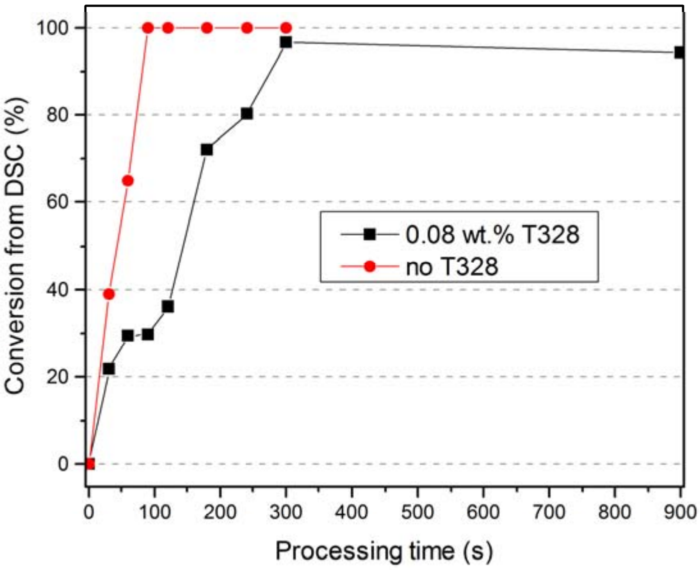

Figure 4.15 Monomer conversion as a function of process time, obtained from DSC measurement, for precursor solution without (red circle) and with 0.08 wt.% T328 (black square). Both precursor solutions were casted with drop volume of 100 µL under 50 mW/cm^2 UV intensity and 1 L/min dry N_2 flow.

Due to both the reduced reaction rate and limited penetration depth, interesting film morphology is obtained, as shown in Figure 4.16. In terms of hierarchy, the morphology is similar to that without T328 (Figure 4.9a), featuring a dense skin layer atop of a particulate layer. However, the thickness of skin layer in Figure 4.16a is measured 136.7 ± 0.7 µm, which is much thicker than that prepared without T328 in Figure 4.9a (84.6 ± 18.6 µm). As we learn from Figure 4.3: increasing UV intensity increases reaction rate, which leads to the delayed onset of phase separation thus larger skin layer thickness. Similarly, the addition of T328 also reduces reaction rate, hence larger skin layer thickness.

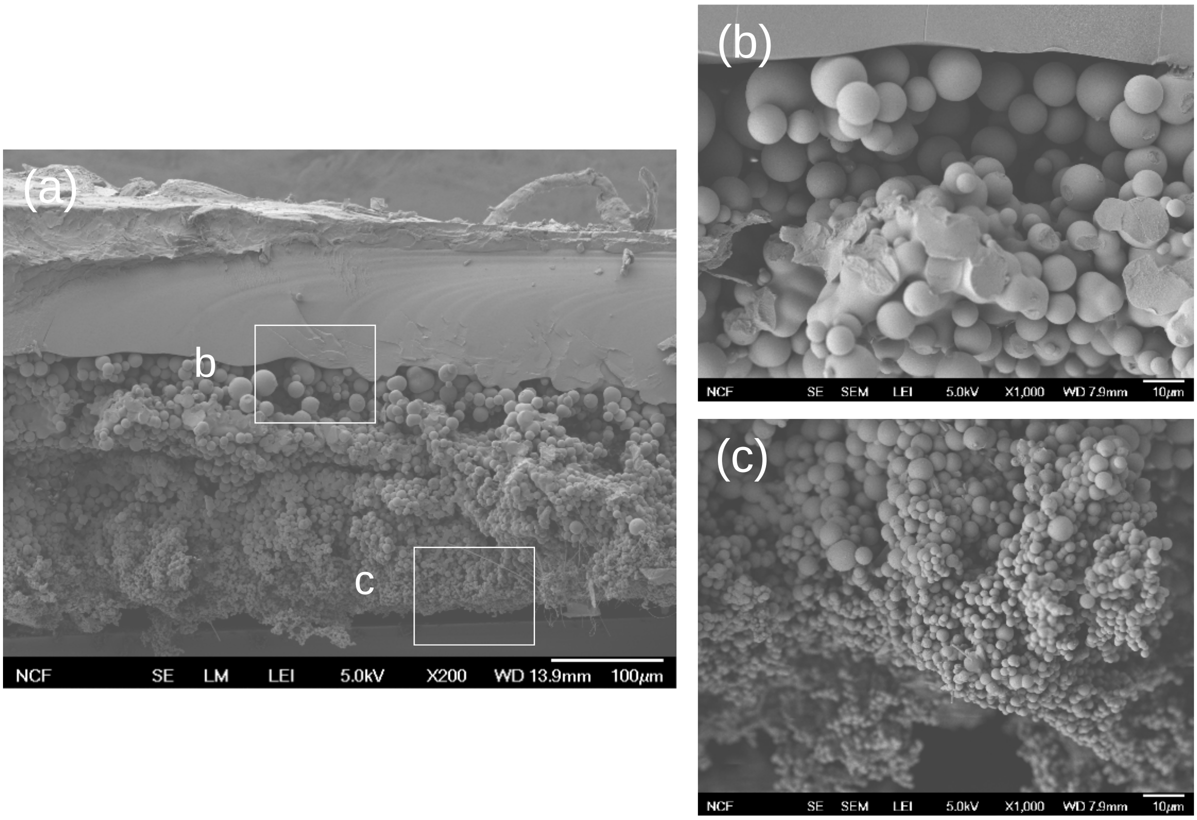

Figure 4.16 Cross-sectional SEM images of the films obtained from 20 wt.% precursor containing NIPAm/T328/DMPA in CS_2 (T328 and DMPA were 0.08 wt.% and 0.12 wt.% of solution, respectively). (b) and (c) are magnified view SEM images taken at the locations indicated by the boxes in (a). Films were obtained after 900 s in a N_2 flowrate of 1 L/min under UV intensity of ~ 50 mW/cm^2.

In terms of particulate morphology, the film prepared from precursor solution with T328 consists microparticles with a gradient of particle size, with particles closer to skin layer being the largest (Figure 4.16b and c). In contrast, the film prepared without T328 (Figure 4.9) shows relatively uniform particles in the particulate layer. During the processing, the non-uniform temperature in the direction of solution thickness as result of moving reaction front (limited penetration depth in the presence of T328) leads to different quenching depth and Λ_m, thus different particle sizes across the thickness. This unique film morphology with gradient particle size suggests the addition of UV absorber provides an avenue to further engineer hierarchical structures.

4.5 Applications of polymer microstructures

As we discussed in the Chapter 1, the microstructured polymer films have a wide range of potential applications. The usefulness of these films are further enhanced when the polymer itself is functional *i.e.* hydrogel polymers. In the following, we present some applications of our method and of the resulting films.

4.5.1 Preparation of microporous hydrogels and microparticles

The microstructured hydrogels are promising as substrates for tissue and cellular engineering[160,161], vehicles for drug delivery[162], and biosensor.[163] Both particulate and porous hydrogels films are advantageous because of the reduced water transport time during swelling or de-swelling processes. Conventionally, such hydrogels usually has been synthesized *via* RIPS in the presence of water whose initial content in the precursor solution must be higher than the equilibrium water uptake of the formed hydrogel for ensuring the occurrence of phase separation.[132–134] In recent years, more efforts were spent on non-aqueous mediums. Zhang et al. reported the synthesis of highly porous PNIPAm gels by the use of mixed solvents of water and THF, which had improved de-swelling and re-swelling kinetics.[129] Bailey et al. found the poly(ethylene glycol) diacrylate hydrogel polymerized in DCM showed enhanced modulus and degradation rate compared to that polymerized in aqueous solution.[130] The adoption of non-aqueous solvent also facilitated dissolution of some chemicals that are insoluble in water and therefore led to the better dispersion.[131] Nonetheless, all these solvents used are merely served as an inert medium and their overall concentrations are kept constant throughout the process. The morphologies of PNIPAm prepared from NIPAm/CS_2 solution in Figure 4.9 suggests we may utilize the method of simultaneous photocrosslinking and solvent evaporation to create microstructured hydrogels.

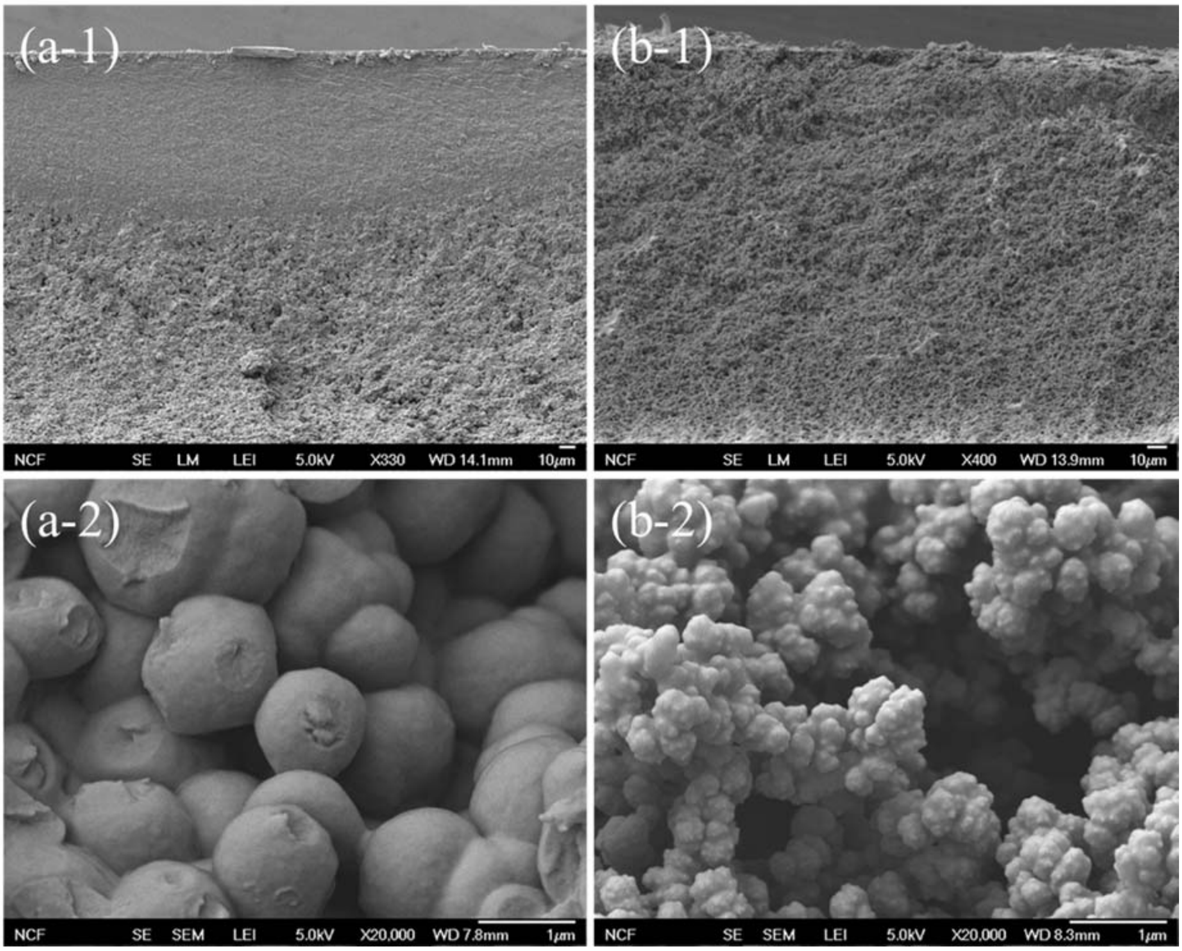

Figure 4.17 Cross-sectional SEM images of the crosslinked films, prepared by the photocrosslinking under evaporating solvents, (a) from 20 wt.% precursor containing HEMA/PEGDMA/DMPA in CS_2, (b) from 15 wt.% precursor containing AAm/PEGDMA/DMPA in acetone. (a-2) and (b-2) are the magnified view of (a-1) and (b-1) respectively. Note that weight ratio of monomer to PEGDMA is 40, and DMPA is 0.6 wt.% of the precursors. All cast solutions were processed for 5 min in a N_2 flowrate of 1 L/min under UV intensity of ~50 mW/cm^2.

In addition to microstructured PNIPAm hydrogel prepared as shown in Figure 4.9, Figure 4.17 presents the morphologies of as-cast PHEMA and PAAm films. Microscopically, the morphology of as-cast PHEMA film comprised a skin layer and a particulate layer from top to bottom (Figure 4.17a-1), similar to the PNIPAm film (Figure 4.9a). However, the particles of PHEMA were less spherical (Figure 4.17a-2) and particle surface was relatively rougher compared to those of PNIPAm films. On the other hand, the cross-section of PAAm casted from acetone revealed only a particulate layer without a capping skin layer. This particulate layer appeared to be a coagulum of (much smaller) primary particles that is different from HEMA or NIPAm systems under the same processing conditions. Moreover, the connectedness of particles was higher. The same morphology was found in PAAm prepared using THF as solvent (image not shown). This irregularity in terms of particle shape may be attributed to the agglomeration of microgels shortly after reaction started due to absence of surfactants that stabilized the microgels, similar to the precipitation polymerization in supercritical carbon dioxide.[164–167]

In the following, we characterized the VPT of PNIPAm films and further demonstrated the possibility of dispersing and harvesting microparticles from the particulate layer of PNIPAm film (Figure 4.9). As compared to other methods of synthesizing hydrogel particles, such as emulsion[12], suspension[13], precipitation[14] polymerization, and photolithography[16], which requires long preparation time, our method is fairly facile and straightforward. PNIPAm is a well-known thermally responsive system that undergoes VPT, at *ca.* 31 °C in water.[168] Below VPT temperature, PNIPAm hydrogel swells by absorbing water; while above VPT temperature, it de-swells by expelling water out. The mechanism associated with the enthalpic change accompanying VPT is rather complicated. Otake et al. reported that enthalpic change is a result of two processes, namely restructuring water molecules around the hydrophobic groups of PNIPAm and association of PNIPAm chains after dehydration.[169] On the other hand, Grinbery et al.[170] and Cho et al.[171] suggested there might be a third process, which is the dissociation of hydrophilic groups of PNIPAm (*i.e.* C=O and N-H) with surrounding water molecules.

Nonetheless, all processes happen simultaneously, resulting in one single endothermic peak around the VPT temperature. As shown in Figure 4.18, the as-cast PNIPAm in our study showed a VPT temperature of 30.8 °C and an endotherm of 1.8 J/g out of PNIPAm aqueous solution respectively, both of which are in good agreement with that reported in literature.[129,169]

The occurrence of VPT of our microstructured PNIPAm hydrogels can also be verified by simply observing the turbidity of the solution at various temperatures. In this experiment, discrete PNIPAm microparticles were dispersed in water by sonication. At 23 °C, a clear, transparent solution was observed in the left inset of Figure 4.18, as the PNIPAm microparticles were swollen with water, which caused the refractive index matching between the swollen gel and the water. When the same vial was heated up to 45 °C, the solution became turbid as shown in the right inset of Figure 4.18. As phase separation occurred, the difference in the refractive indices of PNIPAM particles and water results in the scattering of light, and hence the turbidity. This transition was reversibly observed during the multiple cycles of heating and cooling past the VPT temperature, which indicated the integrity of PNIPAm particles during these thermal cycles.

The dispersion of PNIPAm microparticles in water by sonication suggests that we may be able to harvest these microparticles. The dispersed particle in the solution shown in the inset of Figure 4.18 was re-deposited on silicon wafer by dip coating. From Figure 4.19, isolated, single particles (encircled in red) were loosely deposited on the surface of silicon wafer and magnified view of a single particle can be seen in the inset. A closer examination of this particle found that it had wrinkles on the outer shell, which may be resulted from the swelling/de-swelling cycle during the sonication step. Clusters of particles can still be seen in Figure 4.19, indicating that more efforts are needed to achieve highly dispersed solutions with separated particles. Additional processing techniques such as centrifugation and microfiltration can be potentially adopted to harvest more homogenous hydrogel microparticles. These efforts are beyond the scope of the current study.

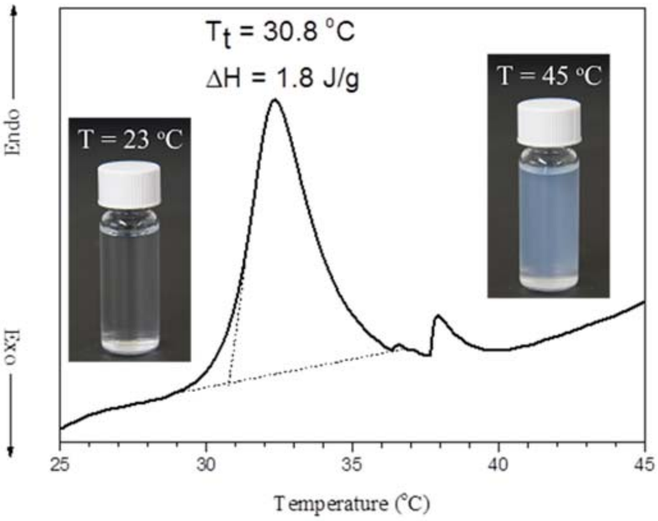

Figure 4.18 DSC thermograph of as-cast PNIPAm film in DI water. The insets are: photographs of the as-cast PNIPAm in DI-water at 23 °C (left) and 45 °C (right).

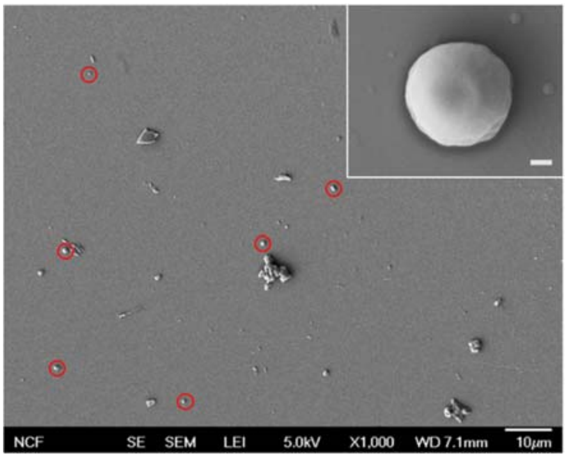

Figure 4.19 SEM image showing harvested PNIPAm particles (encircled in red) lying on surface of untreated silicon wafer by dip coating method. Inset is magnified view of an isolated single particle (scale bar 200 nm).

4.5.2 Porous film as a medium for the study of nanoparticle diffusion

Porous materials are found in many biological systems and technological devices, and mass transport through the pore network is often critical for function. The inherent pore-scale heterogeneity of many natural and synthetic porous materials can make it difficult to model and predict porous transport because the underlying microscopic processes are often poorly understand. To uncover the microscopic mechanisms of porous transport, experiments are needed that track the motion of individual particles from sub-pore to macroscopic length scales. Pioneering work from the Brauchle group used single molecule trajectories to visualize the heterogeneous structure and diffusive dynamics in porous silica.[172,173] Other experiments have focused on high porosity gel networks[174,175], colloidal suspensions[176] or microfabricated models[177,178]. What have been missing are single-particle experiments in three-dimensional porous materials of moderate porosity that go beyond system specific behavior. To address this need, we developed an experimental system that allows imaging of single particle motion deep (~ 20 μm) within a three-dimensional porous polymer film (Figure 4.5c).

The porous NOA65 film we employed was prepared from 10 wt.%/50 wt.%/40 wt.% NOA65/IPA/CS_2 solution (Figure 4.5c). The purpose of using this film lies in the non-skin morphology and relatively uniform globules resulted from SD mechanism. To characterize the void space morphology, we used confocal laser scanning microscopy to image a three-dimensional section of the permeating liquid, which was fluorescently dyed. The confocal data revealed a disordered void network similar to that exposed in the SEM images (Figure 4.5c), albeit a lower resolution (Figure 4.20). Using the two-dimensional confocal sections, we measured the void volume fraction = 0.50 ± 0.07 (*i.e.* porosity), the distribution of minimum chord lengths (*i.e.* confinement lengths), which characterize the length scale of maximum confinement (Figure 4.20). An independent measure of porosity based on the change in sample mass upon saturating with fluid, 0.52 ± 0.02, agreed well with the confocal value.

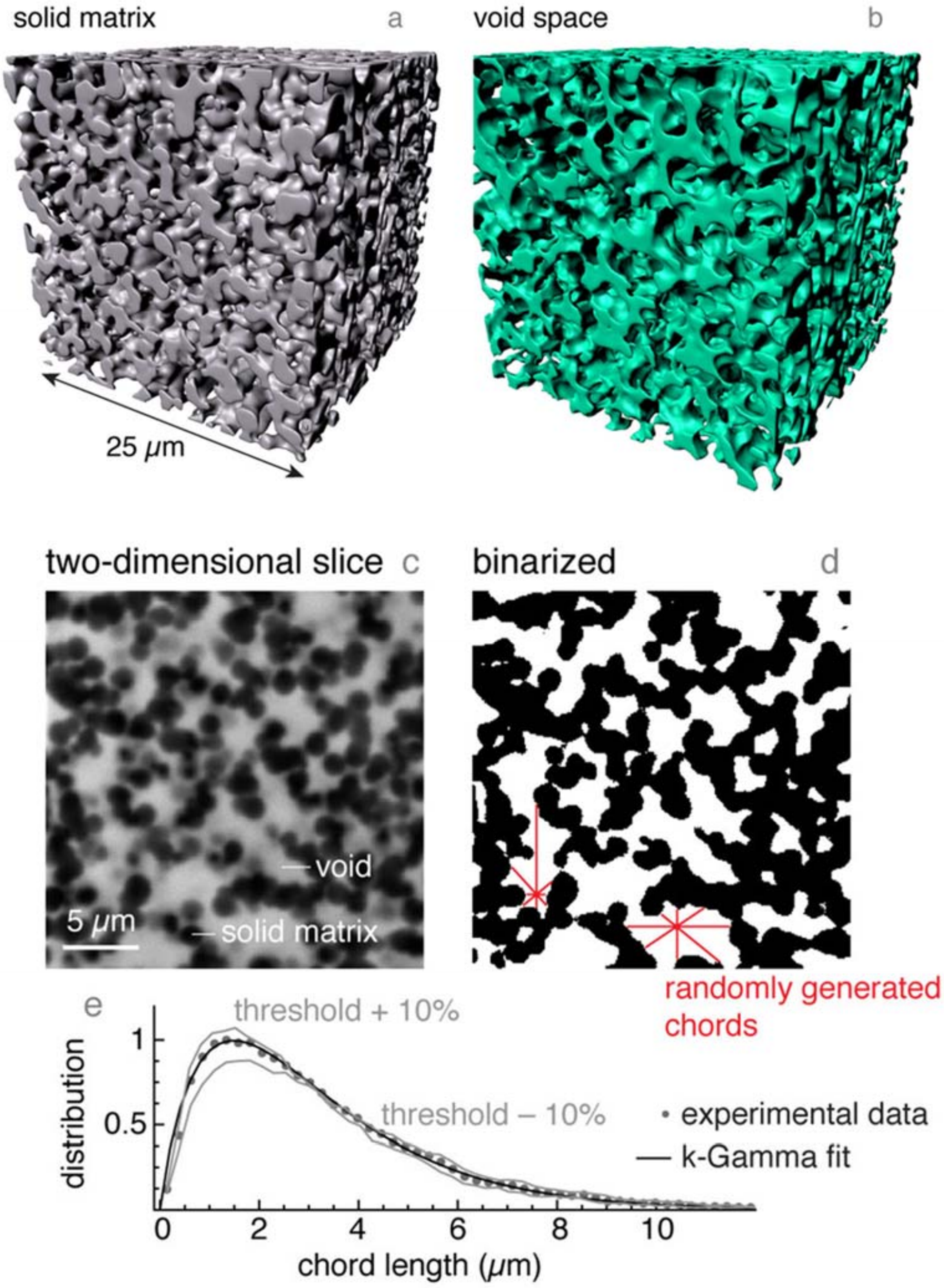

Figure 4.20 Characterization of the porous material using confocal laser scanning microscopy. A rendering of the three-dimensional solid matrix (a) and the conjugate void space (b). (c) A two-dimensional slice showing the voids permeated with fluorescent liquid and the dark solid matrix. After applying an intensity threshold to identify the pore space (d), a chord length analysis was performed, as described in the text, to generate a distribution of chord lengths (e), which characterized the disordered pore sizes.

We imaged the diffusion of sub-micron colloid spheres suspended in a liquid that permeated the void space of this porous polymer films. The colloid spheres were fluorescent PS of three different diameters: 40 nm (dark red, F-8789, Life Technologies) 100 nm (orange, F-8800, Life Technologies) and 200 nm (yellow-green, F-8811, Life Technologies). The particles were dispersed in a 5:1 by volume mixture of thiodiethanol (TDE, Sigma-Aldrich) and Triton X-100 (Sigma-Aldrich). This suspending liquid matched the refractive index of the polymer matrix (n = 1.52, as specified by manufacturer) and prevented particle binding to the pore walls. The particle concentration was sufficiently low (number density $\approx 10^9$/mL) to avoid particle-particle interactions and allow identification of individual particles in the single-particle tracking experiments.

The NOA65 films were first soaked in IPA for 48 h. Before an experiment, the polymer sample was blown dry with N_2 and then sealed in a vacuum desiccator for approximately 1 h. Approximately 50 μL of fluorescent particle suspension was then pipetted onto the top surface of the porous film, allowed to infiltrate the pores and saturated the film (~ 10 min), and then equilibrated for 1 h. After saturating the void space with the fluorescent particle suspension, the porous samples were imaged using a modified epifluorescence microscope (TE-2000, Nikon). Fluorescence excitation was provided by one of three lasers, depending on the particle being imaged: a 491 nm or 532 nm diode-pumped solid state laser (Cobolt AB), or a 640 nm diode-pumped solid state laser (Crystal Laser). Excitation light was delivered and the fluorescence emission collected by a 60×, numerical aperture = 1.2, water-immersion objective (Nikon). The emitted light was passed through a 1.5× relay lens and imaged on an electron-multiplying CCD camera (Andor iXon3), resulting in 145 nm/pixel at the image plane. We imaged particle diffusion 20-30 μm above the polymer-glass interface, near the midplane of the porous film

(Figure 4.21), at a frame rate of 20 Hz for a total of ~ 1 h. To identify and track the motion individual particles in the image sequences, we used custom software that implemented the radial symmetry algorithm.[179] Plotting the accumulated two-dimensional particle trajectories revealed the underlying void space structure (Figure 4.22).

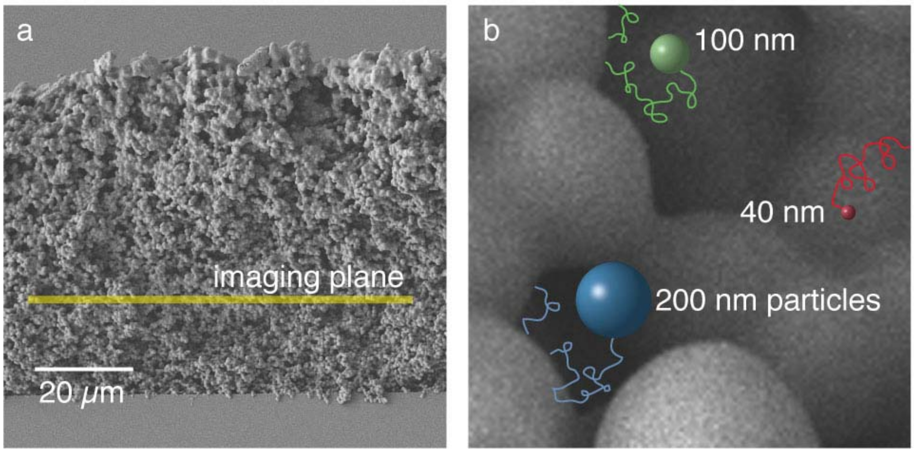

Figure 4.21 Imaging colloid motion in the void space of a porous film. (a) Cross-section SEM image of the crosslinked NOA65 films showing the free surface, the surface in contact with the microscope cover glass and the approximate imaging plane. This film, corresponding to Figure 4.5c, was prepared from NOA65/IPA/CS_2 (10 wt.%/50 wt.%/40 wt.%) solution under UV intensity of 50 mW/cm^2 and 1 L/min N_2 flow rate. (b) A composite illustration showing a higher magnification image of the porous sample and the relative size of the fluorescent tracer particles.

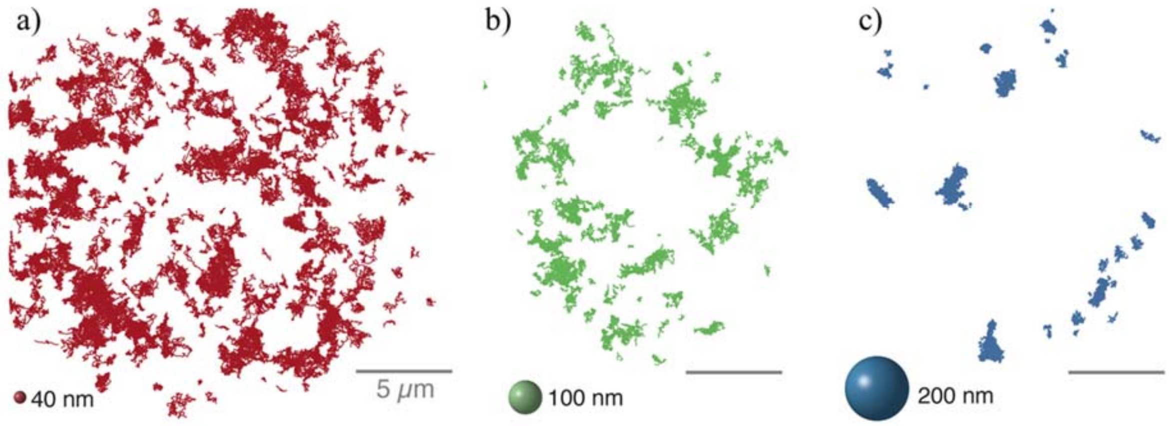

Figure 4.22 Single particle trajectories of (a) 40 nm, (b) 100 nm and (c) 200 nm particles confined to the void space in the NOA65 film corresponding to Figure 4.5c. The absence of trajectories near the perimeter in (a), (b) and (c) is the result of different illuminated areas in the experiments. Scale bar: 5 μm.

4.6 Conclusions

In general, the structure and properties of the polymer films resulted from this process are controlled by the interplay between two dynamic processes, namely, photocrosslinking reaction and solvent evaporation. As a result, three distinct film morphologies can be obtained as illustrated in Figure 4.23. At the early stage, fast evaporation of the solvent at the drop surface, greatly facilitated by the N_2 flow, results in a gradient of precursor concentration, which polymerizes/crosslinks into a skin layer. This skin layer, once formed, will reduce the diffusivity of solvent within the drop to reach the solution/air interface, and thus slows down the evaporation rate. The skin layer can continuously grow downward when no phase separation occurs within the skin-layer capped solution, which results in a homogeneous polymer film (case I in Figure 4.23). In contrast, if phase separation indeed occurs in solution such as NOA65/CS_2 and NIPAm/CS_2, a hierarchical film is obtained, consisting of a phase-separated structure underneath a dense skin layer, as shown in case II in Figure 4.23. Another morphology may be observed as the case III in Figure 4.23, where the skin formation is suppressed and phase separation occurs throughout the entire thickness of the solution, resulting in a particulate film without the capping skin. The suppression of skin in this morphology may be resulted from the reduced overall evaporation rate and/or enlarged miscibility gap, as exemplified by free convection of NOA65/CS_2 solution and NOA65/IPA/CS_2 solution.

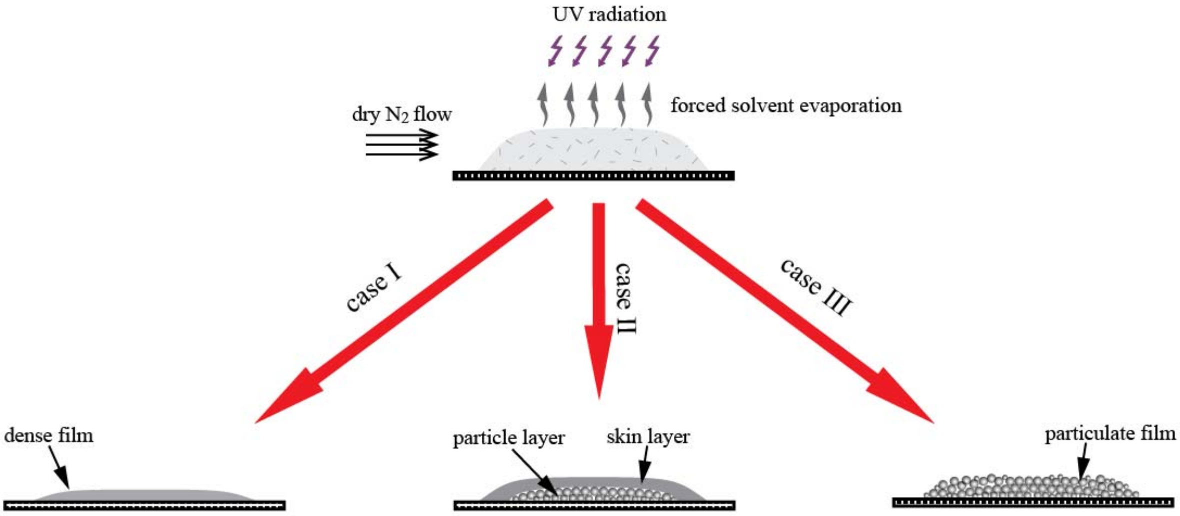

Figure 4.23 Schematic of photopolymerization of precursors in an evaporating solution (upper row) leading to different film morphologies shown as cross-sectional view (lower row).

For the first time, the polymer skin layer formed during the evaporation can be obtained after the evaporation (case II in Figure 4.23), in contrast to the linear polymer solutions. The final thickness of the skin layer is dependent on the processing parameters ranging from the N_2 flow rate, UV intensity to NOA65 concentration. A theoretical model, based on the one for the non-crosslinked polymer solution, is developed that can successfully describe the skin layer formation and its dependence on these processing parameters. These findings provide a mechanistic understanding of the photocrosslinking process under evaporative environments, which is important for its potential applications such as photoactive coatings, separation membranes and drug delivery.

Furthermore, we demonstrate the versatility of this method to create microstructured hydrogels for a range of hydrogel forming precursors such as HEMA and AAm. Moreover, we showed the possibility of dispersing and harvesting microsphere hydrogels from the particulate layer of the resulting films. The acquired PNIPAm microparticles showed excellent VPT in DI water, with comparable transition temperature and enthalpy with that from other methods. These

o

interesting morphologies of hydrogels might have potential uses owing to the enhanced de-swelling and re-swelling kinetics. We also demonstrate the use of the microporous films for single-particle tracking in which we followed the pore-scale diffusion of individual nanoparticles. We observed size-dependent exclusion of particles from different voids, which sheds new light on the possible mechanisms of size exclusion chromatography. Our results suggest that pore-scale diffusion is more heterogeneous and volume accessibility more limited than previous expected.

5 FORMATION OF CROSSLINKED MICROPOROUS FILMS UNDER MOIST AIRFLOW

5.1 Introduction

Macro- or meso- porous films with highly ordered pore-structures have received much attention because of their potential applications in photonics, electronic, and biotechnologies. Top-down lithographic techniques, such as photolithography and contact lithography, can reliably fabricate micro- and nano-structures with high uniformity. However, they usually require multiple processing steps, expensive instruments, and pre-patterned templates or masks. In comparison, bottom-up fabrication approaches become increasingly attractive due to their simplicity, high throughput, and low fabrication cost, often by exploiting self-assembly mechanisms of colloidal particles[7,180–191], emulsions[192–194], and block copolymers[195–197].

Among them, “breath figure template assembly” (BFTA) is one of the most simple and elegant bottom-up assembly techniques to create ordered pores in polymeric films. BF method exploits the nucleation and assembly of water droplets, within an evaporating polymer solution, on solid surfaces under a humid environment. Briefly, the evaporation of the volatile solvent causes a local temperature drop (to below the dew point of water) in the concentrating polymer solution. In the presence of moisture, water will condense in such a cooler surface/film *via* a nucleation and growth process. As the remaining polymer solution continues to concentrate, the water droplets, separated by a layer of polymer/solvent, self-organize into well-ordered honeycomb morphology. Once the polymer solution evolves into a gel-like state, the honeycomb structure is then fixed. Finally, the polymer vitrifies completely, and a polymer film containing honeycomb pores is obtained after the removal of entrapped water droplets.

This “moist-casting” technique, first reported by Widawski et al.[32], has attracted broad interests and has been applied to create porous structures in different types of polymeric materials.[33,105]. The conditions for BF formations highly depend on the material chosen and the underlying mechanisms for BF formation could be different.[33,105] Nevertheless, BF method is of significant interest for a range of potential applications due to its simplicity. Correspondingly, the class of materials that can be used as matrix for the BF formations are continuously expanding.

Compared with their linear counterparts, crosslinked polymers have many advantages, particularly, their resistance against solvent dissolution and extended rubbery regions at high temperature. These make them attractive in applications such as shape memory polymers, dental resins, adhesives and tissue scaffolds. To date, crosslinked polymer films containing BF-templated porous structures were obtained by crosslinking the matrix after the BF formations.[37,40,42–49] This synthesis/processing route requires that the BF-forming polymers contain crosslinkable chemical groups.

In this chapter, we present a simple and convenient one-step method to create BF structures in crosslinked polymer films, by *in situ* photocrosslinking of an evaporating precursor solution in the presence of moisture. We demonstrate this method can be applicable to a range of photocurable precursor solutions including tert-butyl acrylate (tBA)/chloroform, methyl methacrylate (MMA)/carbon disulfide (CS_2) and Norland optical adhesive 65 (NOA65)/CS_2. We further investigate the influence of external conditions and precursor compositions on the surface morphologies of the as-cast films. Detailed characterizations including morphological, chemical and physical properties of the fabricated porous films were carried out, as they are important for potential applications of these materials.

5.2 Effects of gelation and skin effect on BFTA process

In conventional, non-reactive BF-forming process, the gelation that fixes the BF morphology is largely dictated by the solvent evaporation. On the contrary, in our reactive BF process, the BF-fixing gelation may be determined by both the photocrosslinking reaction and solvent evaporation, as illustrated in Figure 5.1. Furthermore, as we discussed in Section 2.1.1, the gelation may occurs *via* two routes, depending on whether skin effect occurs or not. In non-skin scenario, whole solution gets increasingly concentrated throughout the thickness and subsequently turns into a gelled matrix that fixes BF morphology; whereas in skin formation scenario, a gelled skin appears at the surface of the solution first and then grows downwards. Apparently, gelation *via* the latter route results in smaller BF pores since the gelation in forms of skin effect that fixes BF morphology appears much earlier.

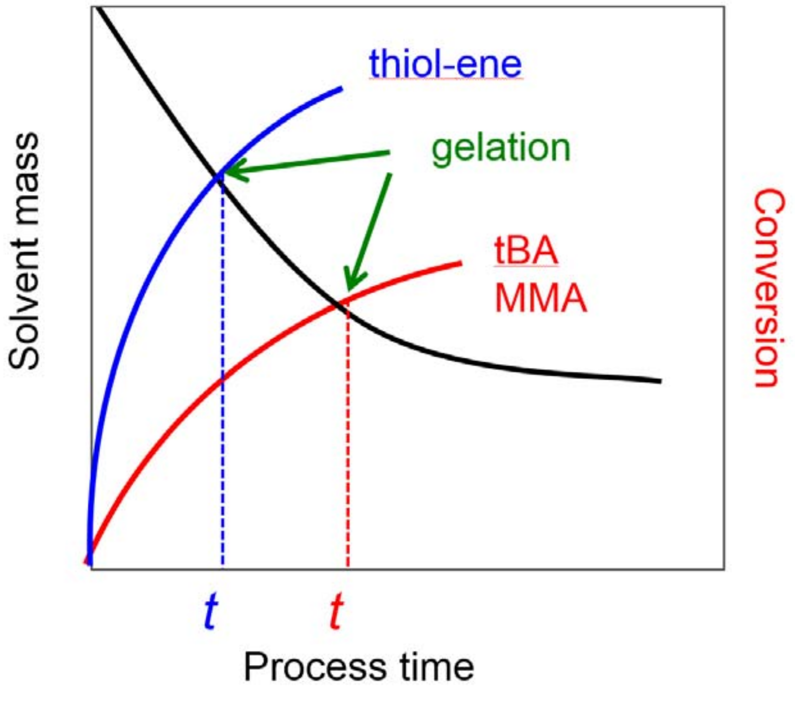

Figure 5.1 Illustration of gelation (a crossover of solvent mass curve and precursor conversion curve) that fixes water droplets, thus forming BF films. Two types of reactive precursors are considered here: thiol-ene (blue conversion curve, free-radical mediated step growth mechanism) vs. acrylate (red conversion curve, free-radical chain growth mechanism).

Since the emergence of skin effect is important to the quality (overall porosity, size and distribution of the pores) of BF films, we first provide a qualitative analysis of whether a skin layer forms, according to[59],

$$\mathrm{Pe} \equiv \frac{h_0 J}{D} > \frac{\emptyset_{2g} - \emptyset_{2i}}{\emptyset_{2i}(1 - \emptyset_{2i})} \qquad \text{Eqn 5.1}$$

where D is mutual diffusion coefficient of the solution, J is the evaporation flux, h_0 is the initial thickness of the polymer solution, $\emptyset_{2i}$ and $\emptyset_{2g}$ are initial polymer volume fraction and polymer volume fraction corresponding to the gel point, respectively. For the sake of simplicity, we here use a non-reactive BF forming system, polystyrene (PS)/CS_2. According to the reference[198], the gelation concentration ($\emptyset_{2g}$) of PS/CS_2 solution within the BF process temperature (see Figure 2.11) is roughly in the range of 10 - 20 %. Using the average $\emptyset_{2g}$ = 15 %, the parameter space described by Eqn 5.1 is shown in Figure 5.2. Specifically, for a skin layer to form, the parameter space ($\emptyset_{2i}$, Pe) must be above the curve. Note that Pe ≡ h_0J / D. Similar to $\emptyset_{2g}$, D is also known for a given polymer solution such as PS/CS_2. Therefore, J, h_0, and $\emptyset_0$ are the only variables we can manipulate for the BF-forming process. To avoid the skin effect, we could either decrease the left-hand side term (Pe) or increases the right-hand side term in the inequality (Eqn 5.1). Therefore it leads to a range of strategies for making a high quality BF-templated porous film: 1) placing the solution in a static environment or under a mild airflow rate (resulting in moderate J), 2) planarizing the solution with external forces *i.e.* blade casting and spin coating to reduce h_0, and 3) using a dilute polymer solution to start with, *i.e.* small value of ($\emptyset_{2i}$).

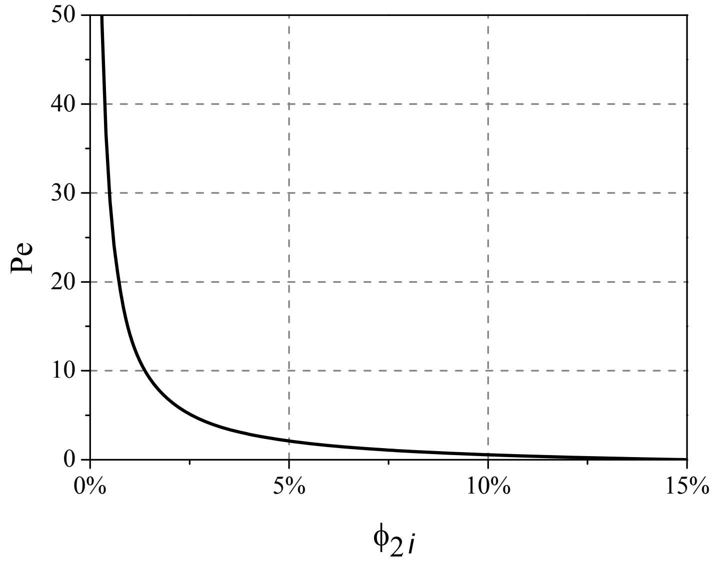

Figure 5.2 Plot of skin formation criterion using Eqn 5.1. Skin layer only forms when a point ($\emptyset_{2i}$, Pe) is above the solid line.[59]

In the following sections, we investigate the film morphology obtained using *in situ* photocrosslinking reaction in an evaporating solution in the presence of a moisturized N_2 flow with two types of photocruable precursors, namely acrylate-based (e.g. tBA and MMA) and thiol-ene (e.g. NOA65). The two acrylate-based precursors, tBA and MMA, photopolymerize *via* free-radical chain growth mechanism, whose reaction kinetics is reportedly much slower than thiol-ene.[113,114] And neither solution (tBA/chloroform and MMA/CS_2) expectedly forms a skin layer during the BF formation process: for the tBA/chloroform system, the initial 2 s spin planarized the solution and consequently h_0 was appreciably reduced; for the MMA/CS_2 system, the suppression of skin layer formation in the solution was attributed to the low initial precursor concentration (5 vol.% = 2.3 wt.%). As a result, the gelation of two precursor solutions (a crossover of solvent mass curve and precursor conversion curve) occurs later, thus permitting longer growth of water droplets and larger BF pores (Figure 5.1). On the other hand, thiol-ene (e.g. NOA65) reacts much faster, *via* free radical mediated step growth mechanism and

NOA65/CS_2 precursor solution is experimentally confirmed to form a skin layer (see Section 4.3). Therefore, the gelation is expected to kick in much earlier (Figure 5.1); in other words, a smaller time prior to the gelation is allowed for the growth of water droplets. As a result, we may expect smaller BF pores upon the completion of the process. In the following sections, we will discuss in detail about how the gelation (determined by both solvent evaporation and photocrosslinking reaction) affects the BF morphology.

5.3 Formation of BF in a reacting solution and morphology characterizations

For BF to form during the process, it is required that the temperature of the solution drop to reach below the dew point. The overall enthalpic energy during the BF/photocrosslinking process is highly dynamic and complex, including UV absorption (ΔH_i), solvent evaporation (ΔH_v), and polymerization enthalpy (ΔH_c). Specifically, ΔH_c of MMA and tBA is ~ 13 kcal/mol[199] and ΔH_c of tetraethylene glycol dimethacrylate (TEGDMA, the crosslinker) is ~ 33 kcal/mol[200]; while ΔH_v of chloroform and CS_2 is ~ 7 and 6.5 kcal/mol respectively (Table 4.1). For a relatively dilute monomer solution, such as a 5 vol.% MMA/TEGDMA in CS_2 used in Section 5.3.2, ΔH_v ranges from 18 to 16 times of ΔH_c as the MMA composition (with respect to MMA/TEGDMA) increases from 50 wt.% to 90 wt.%. Thus, the influence of reaction heat on the BF formation can be neglected at low concentrations. In terms of ΔH_i, heat generated from the UV radiation with an intensity of 5.4 mW/cm^2 is even less than ΔH_c, thus is also negligible. Therefore, for the one-step process reported here, the total heat exchange is still dominated by the solvent evaporation, similar to the conventional BF method in non-reactive solutions, which cools the solution and allows the water droplets to condense. Indirect evidence is that the resulting film casted under identical conditions but a ten times higher UV intensity shows a transparent film without any traces of BF structured pores. On the other hand, the interplay between the two-phase transitions (solvent evaporation and water condensation) and the photo-induced crosslinking reaction is extremely complex and convoluted, limiting the possibility to achieve a quantitative description of the fabrication process. However, as described in the following, successful fabrication of the porous films with a range of precursor solutions was achieved. The systematic experimental work below will provide a correlation between the pore morphology and the process conditions.

Table 5.1 Processing parameters for the reactive systems.

	Acrylate-based/TEGDMA/0.2 wt.% DMPA									NOA65
#	A	B	C	D	E	F	G	H	I	J
Monomer	tBA	tBA	tBA	tBA	MMA	MMA	MMA	MMA	MMA	NOA65
Monomer/crosslinker wt./wt.	80/20	80/20	80/20	80/20	50/50	60/40	70/30	80/20	90/10	/
Precursor concentration vol./vol.	20	20	20	20	5	5	5	5	5	10 wt./wt.
UV intensity (mW/cm^2)	6.0	6.0	6.0	6.0	5.4	5.4	5.4	5.4	5.4	6.0
Collimated UV intensity	/	/	/	/	Yes	Yes	Yes	Yes	Yes	Yes
Flow rate (L/min)	1.6	1.6	1.6	0.8	2	2	2	2	2	5
Initial spin 2 s	Yes	Yes	Yes	Yes	/	/	/	/	/	/
Pre-polymerization under dry N_2 (min)	/	2	/	/	/	/	/	/	/	/
Polymerization under moist N_2 (min)	15	13	1	2	10	10	10	10	10	3
Post-polymerization under dry N_2 min	/	/	14	14	/	/	/	/	/	/

5.3.1 Morphological dependence of as-cast films on external conditions using tBA/chloroform system

We start our discussion with the tBA/chloroform system. Here we used 0.2 wt.% DMPA and 20 wt.% TEGDMA in the precursor as the photoinitiator and crosslinker respectively. Here the concentration refers to DMPA/tBA/TEGDMA composition, not the solution concentration. Note that outside the processing window reported below, the resulting crosslinked films displayed either a continuous smooth film without appreciable BF formation, or a BF-structured film with a broad distribution in the size of the water droplets, which were completely disorganized and inhomogeneous. Following these considerations, concentration of the precursor (tBA/TEGDMA/DMPA) in chloroform of 20% v/v was found to be the optimal. The enthalpy calculation revealed that ΔH_v is still ~ 3.4 times higher than ΔH_c, agreeing well with the previous discussion that solvent evaporation ΔH_c has to be predominant in order to form BF films. Furthermore, a polyethylene terephthalate (PET) film (~ 200 μm thick) was chosen as the casting solid substrate, instead of cover glass. The monomer solution showed nearly complete spreading (wetting) on the cover glass, not allowing good control over the volumes of solution. On the PET film, instead, the deposited drops of the monomer solution showed limited spreading. Both small drops (40 μL) and larger ones (100 ‒ 200 μL) on PET films yielded good BF formations in the crosslinked films, but larger volumes led to larger area of homogeneous BFs, especially when the solution was evenly distributed over the PET surface. The optimal spreading of the monomer solution was obtained simply by spinning the sample for 2 s time before the initiation of the reaction, with a spinning rate between 100 and 200 RPM. In this way, we were able to reduce the surface curvature of the solution drop. In addition, a long wave UV lamp (Black-Ray, B-100AP) without collimating adaptor was used. Regardless, the measured the intensity profile of this lamp as a function of distance from the center is not appreciably non-uniform over the surface area of the solution drop. Therefore, the possible variation of film morphologies due to the intensity profile should not be an issue here.

For the tBA/chloroform system, the controlled exposure of the monomer solution to either moist or dry N_2 at different stages of the polymerization was examined, and four samples (A-D) obtained with different procedures are listed in Table 5.1. In the following, we describe the detailed morphology of the porous films obtained. Best results in terms of BF packing density, shape regularity, size distribution and local ordering, were obtained *via* performing the polymerization at higher flow rates (1.6 L/min) of moist N_2 (sample A), using relatively large (100 µL or 200 µL) drops, with 2 s spinning before the whole process. Figure 5.3 presents the representative SEM images for sample A, revealing relatively homogeneous distribution of the pores (after removing the water) in terms of both shape and size. Most pores appear to deviate from a perfect circle, with a circularity = 0.79 ± 0.09. Their average diameters equal to 8.1 ± 1.3 µm, with a perimeter equal to 25.4 ± 4.0 µm. Apparently, the size of these pores is relatively large, probably due to the contemporary growth of the water droplets and the polymer chains, which leads to appreciable growth and/or coalescence of smaller droplets. Overall, the pores tend to pack in honeycomb structure with closed cells, as shown by the FFT image (Figure 5.3a, inset). In addition, the pores cover 60.0 % of the film surface and the thickness of the cell walls between neighboring droplets is equal to 1.4 ± 0.3 µm. The geometric parameters extracted from SEM images of sample A, and all other samples discussed below, are summarized in Table 5.2.

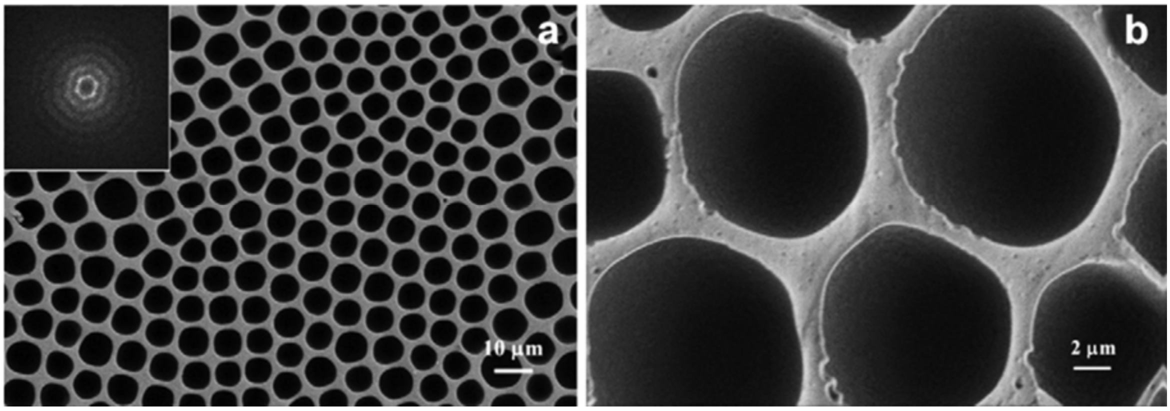

Figure 5.3 SEM images of sample A with a) a larger view and b) a close view. Inset in a) is the FFT image of the SEM image.

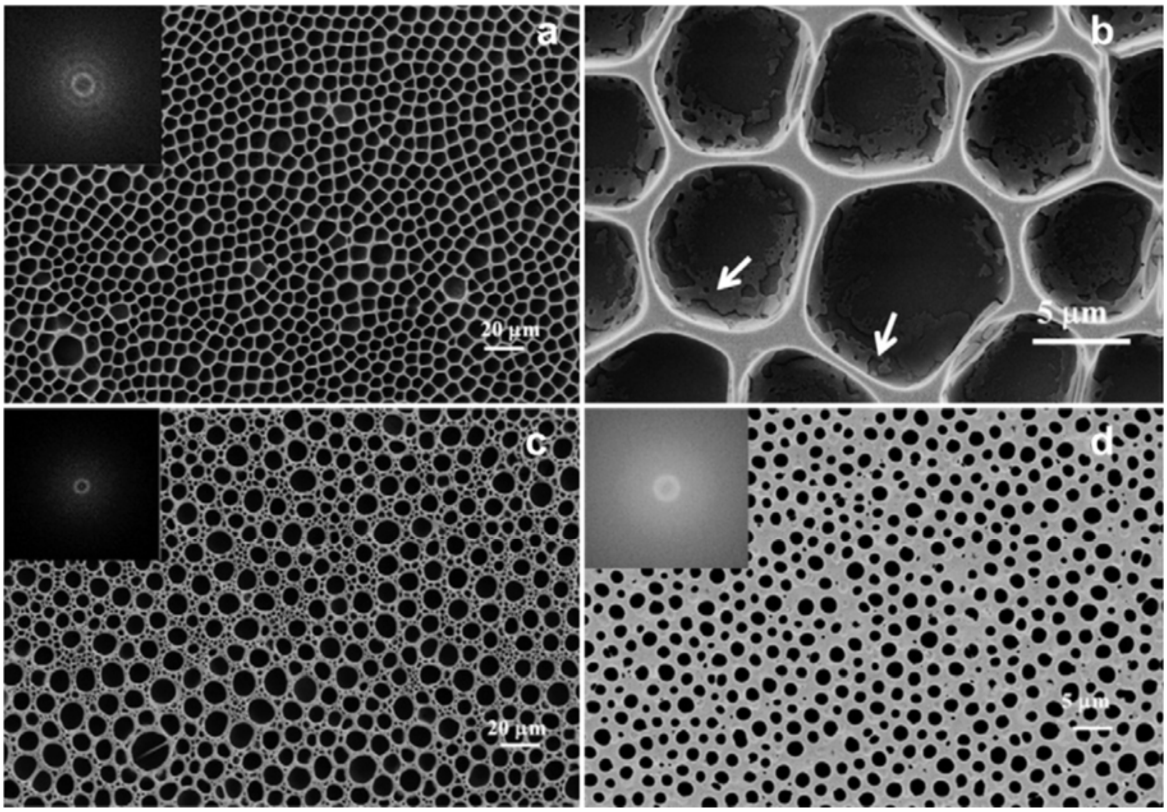

Figure 5.4 Representative SEM images for sample B with a) a large view and b) closer view, sample C c) and sample D d). The insets are the FFT images of the corresponding SEM images.

To increase the volume fraction of the water droplets and/or their degree of packing, a pre-polymerization time was imposed. The monomer solution was first exposed to UV radiation under dry N_2 atmosphere (or flow) for 2 min before being exposed to the moist N_2. In this case, we expect BF start to form when the polymer chains were partially formed and the overall concentration (or viscosity) was increased compared with sample A. The SEM images of the resulting porous films (sample B) are shown in Figure 5.4a and b. Clearly, non-through pores (as visible in Figure 5.4b) are packed closer than those in sample A. However, the degree of ordering is noticeably lower as confirmed by FFT analysis (Figure 5.4a, inset).

Both the size and distribution of the pores in sample B are slightly larger than that in sample A, but the surface coverage of the pores has increased to 68.3 % (Table 5.2). The cell wall thickness of sample B has reduced to 1.1 ± 0.2 μm, noticeably lower than that of sample A, consistent with a concomitant increase in packing density. These pores are even further deviated from the round shape compared with sample A, with a circularity = 0.64 ± 0.13. Moreover, it is evident that there are randomly distributed and isolated larger pores (Figure 5.4a), due to the localized coalescence between the smaller droplets. Such coalescence is more likely to occur as the cell wall thickness separating neighboring droplets gets thinner. From Figure 5.4b, the inner walls of the pores appear to be less smooth than that in sample A, as indicated by the arrows, and were commonly observed for most samples.

Figure 5.4c shows the representative SEM images for sample C, obtained after a shorter exposure to moist N_2, *i.e.* the moist N_2 flow is switched to dry N_2 after only 1 min (Table 5.1). In this case, the porous film resulting from the BFs is highly inhomogeneous, displaying a bi-modal distribution of the pore diameters as shown in Figure 5.4c. However, reasonably high density of BFs was still achieved. The SEM images reveal the coexistence of large diameter pores (with average diameter 9.7 ± 1.9 μm), surrounded by a cloud of small pores (average diameter 0.5 μm). Such bi-modal distribution of pores is probably related to the fact that the introduction of dry N_2 in the chamber hinders the continual growth of the droplets, while, at the same time, coalescence among droplets continues to occur. As a result, bigger droplets can continue to increase in size by engulfing the nearby smaller drops, until the polymerization/crosslinking is completed (or the system is completely gelled).

Table 5.2 Geometric parameters obtained from the SEM images for all samples listed in Table 5.1.

#	Circularity	Diameter (μm)	Perimeter (μm)	Wall thickness (μm)	Surface coverage (%)
A	0.79 ± 0.09	8.1 ± 1.3	25.4 ± 4.0	1.4 ± 0.3	60.0
B	0.64 ± 0.13	8.5 ± 2.2	26.7 ± 7.0	1.1 ± 0.2	68.3
C	0.87 ± 0.05	9.7 ± 1.9	30.6 ± 5.9	3.3 ± 1.4	45.8
D	0.91 ± 0.09	1.6 ± 0.4	5.1 ± 1.3	1.2 ± 0.5	32.9

The average circularity of all the pores for sample C is estimated around 0.87 ± 0.11, higher than both sample A and B. After filtering the small size pores with a threshold diameter of 6 μm, the surface coverage of the remaining larger pores ranges from 45.8 % to 50.4 %. Moreover, the distribution of the circularity of these larger pores is much narrower: 0.87 ± 0.05. This suggests that the lower density packing of the BFs is likely to cause fewer amount of residual stresses within the film during the process, which results in lower degree of deformation of the droplets. On the other hand, the shape of the smaller pores distributed in the interstitial areas of the larger pores (wall thickness 3.3 ± 1.4 μm) significantly deviate from the circular shape (Figure 5.4c), which could be a consequence of the shrinkage stresses within the films and/or the compressive stresses exerted by the growth of the larger pores. Lastly, the FFT analysis (inset of Figure 5.4c) shows only short-range correlations between the pores.

The reduction in degree of BF ordering is even more evident in Sample D, obtained after being exposed to a lower flow rate (0.8 L/min) for a shorter duration (2 min) of moist N_2, which effectively lower the partial vapor pressure or the degree of saturation of the water vapor inside the chamber. In addition, the final stage of the polymerization was completed in dry N_2. Figure 5.4d shows the morphology of the pores in sample D, displaying short-range correlation and low-density packing. Overall, these pores are more circular in shape, with the circularity equals to 0.91 ± 0.09. The average diameter of the pores is only 1.6 ± 0.4 μm, which is significantly lower than all previous samples (A-C), probably due to the limited growth of the droplets during the shorter exposure to moist atmosphere. Correspondingly, surface coverage of the pores drops to only 32.9 % and FFT analysis shows a weak correlation among the pores (Figure 5.4d, inset). Apparently, reduced vapor exposure limits the growth of the nucleated water droplets and thus leads to their smaller diameter, lower surface coverage, and large cell wall thickness. However, such limited growth also produces highly circular pores.

5.3.2 Morphological dependence of as-cast films on precursor compositions using MMA/CS_2 system

Similarly, porous films of another acrylate-based system were also successfully obtained using this method. The system contains MMA as monomer instead of tBA but with identical crosslinker and photoinitiator. To examine the morphological dependence of as-cast films on precursor compositions, we varied MMA/TEGDMA ratios in the precursor from 50 wt.% to 90 wt.% at a 10 wt.% interval. A given MMA/TEGDMA formulation, containing 0.2 wt.% DMPA, was dissolved in CS_2. The concentrations of the precursors (MMA/TEGDMA/DMPA) in the CS_2 were 5 vol.% for all different MMA/TEGDMA ratios. After homogeneous solutions were obtained by vortex mixer, all solutions (regardless of MMA/TEGDMA ratios) were casted under the identical external conditions as specified in Table 5.1. Specifically, a drop of reactive solution (100 μL) was deposited on the PET substrate (same substrate as tBA/chloroform system in the previous section), immediately followed by exposing to both UV radiation of ~ 5.4 mW/cm^2 and a moist N_2 flow of 2 L/min in the reactive chamber for 10 min. To diminish experimental variations, we used a collimated UV spot curing system as mentioned in the Experimental Section 3.1 (same for all the following sections). Additionally, we did not planarize solution with spin, which might result in 1) attenuated UV radiation that initiated reaction sequentially throughout the solution thickness, and 2) Marangoni convection that alter the distribution of pores and materials in the final BF films. Therefore in the following, we will investigate the effect of both precursor compositions and non-spin condition on the morphologies of resulting films.

We first examined the conversion of C=C double bonds from MMA and TEGMDA with ATR-FTIR, and confirmed that high conversions of the C=C double bonds were indeed achieved for all the porous films obtained. Figure 5.5 shows the representative ATR-FTIR spectrum of the obtained porous films with a composition of 50 wt.% MMA. A small but recognizable adsorption peak at ~ 1639 cm^{-1} was observed, which corresponds to the stretching mode of C=C double bond.[201] For bulk methacrylate and other network-forming systems such as thiol-ene polymers, such a low fraction of unreacted double bonds in the crosslinked samples is commonly observed, due to the restricted mass transport at the later stage of the crosslinking reaction.[202]

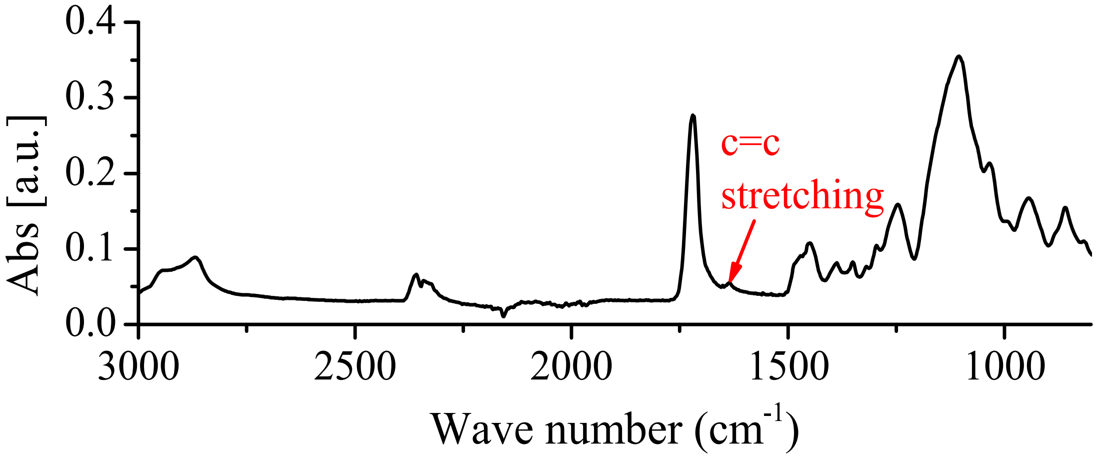

Figure 5.5 Representative ATR-FTIR spectrum for the porous films obtained, with an MMA/TEGDMA weight ratio of 50/50. The arrow marks the absorption peak corresponding to the unreacted carbon-carbon double bonds.

Unlike the morphology prepared from tBA/chloroform in the previous section, for all the porous films the morphology prepared from MMA/CS_2 at the peripheral area is noticeably different from that at the center area. For samples with MMA composition ranging from 50 wt.% to 80 wt.%, the morphology of the porous films was similar. Figure 5.6 shows the representative top-down view SEM images of the porous film containing 80 wt.% MMA at the peripheral area (Figure 5.6a) and at the center area (Figure 5.6b). At the peripheral area, honeycomb like ordered pores with uniform sizes, were observed. In comparison, the pores formed at the center of the films were evidently less ordered and the size distribution was much broader than that at the peripheral area. Further, it appears that there were pores underneath the first layer of pores at the peripheral area, as marked by the arrow in Figure 5.6a. This is more clearly shown in the cross-sectional image (Figure 5.6c), revealing randomly distributed pores underneath the close-packed top layer. In stark contrast, at the center of the film, there appears to be only one layer of pores (Figure 5.6d). In literature, multilayered structures of uniformly ordered honey-comb films were demonstrated by the BF method using linear polymers.[32,35,203]

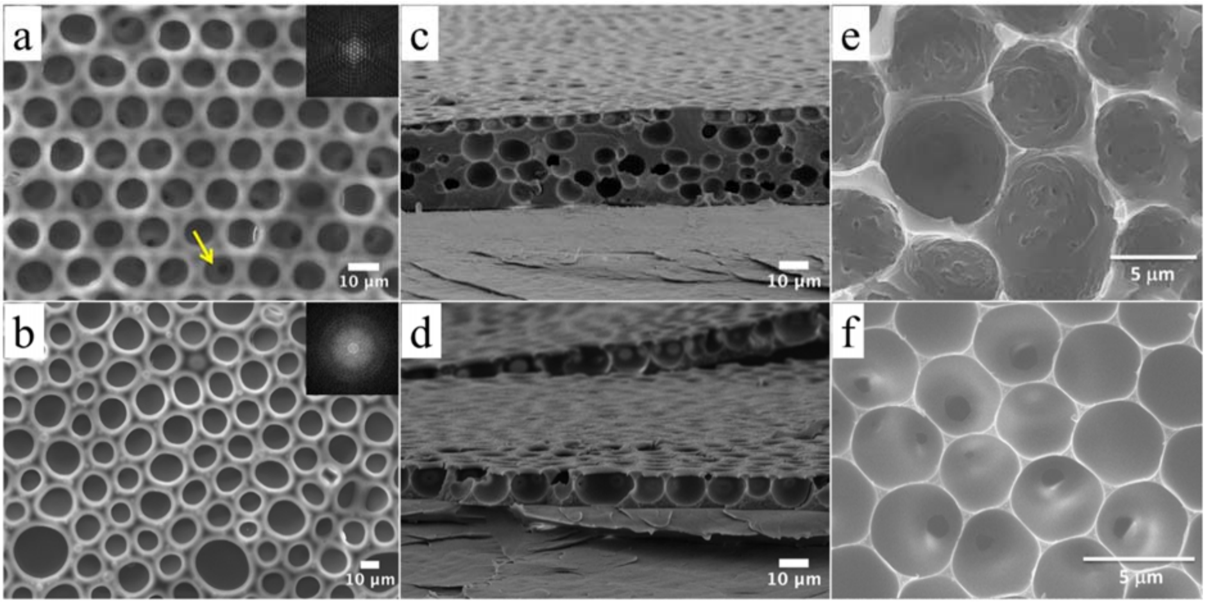

Figure 5.6 Top-down view SEM images of pore morphology for a porous film, prepared from 5 vol.% MMA/TEGDMA (MMA/TEGDMA = 80/20 wt./wt.) in CS_2 using BF methods under simultaneous ~ 5.4 mW/cm^2 UV radiation and 2 L/min moisturized N_2 flow, at the peripheral (a) and at the center regions (b). The insets are the FFT of the SEM image. (c) and (d) are the cross-sectional view SEM images at the peripheral and center regions, corresponding to (a) and (b). (e) and (f) are the top-down view SEM image of the pores after peeling off the top mesh for our crosslinked film and for a porous PS film.

From Figure 5.6c and d, it is also clear that the porous film thickness was much larger at the peripheral area than at the center, which was observed for all samples. We further examined the thickness distribution of non-porous films obtained by photocrosslinking under dry N_2 (Figure 5.7). Similarly, the thickness measured by the profilometer at the peripheral area was larger than that at the center region. Furthermore, the side (right hand side of the film in Figure 5.7) that was the closest to the inlet of N_2 had the largest film thickness. The above observed differences, in both the thickness and the pore morphology, between the peripheral and center regions are resulted from the non-spin condition, as described below.

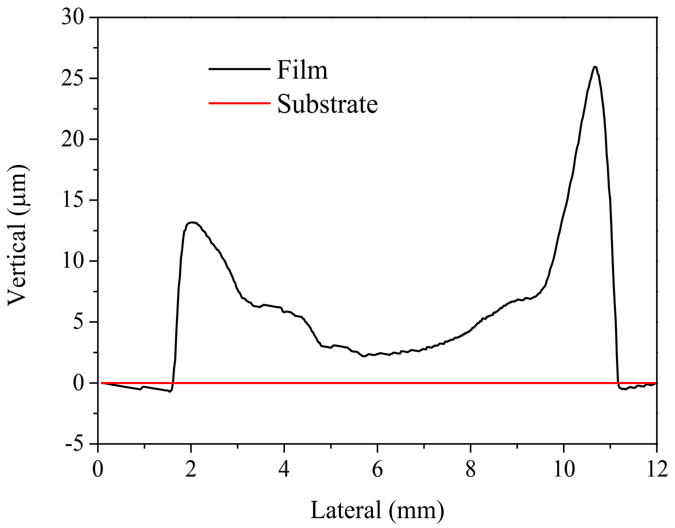

Figure 5.7 Representative thickness profile of non-porous film prepared by photocrosslinking 5 vol.% MMA/TEGDMA/DMPA in CS_2 (MMA/TEGDMA = 50/50 wt./wt.) at ~ 5.4 mW/cm^2 UV intensity under 1 L/min dry N_2 flow. The right hand side of the film shown is the side closest to the inlet of N_2.

The UV intensity attenuates exponentially with the penetration depth, as governed by Beer-Lambert law.[146–148,204] For photocrosslinking system like the MMA/TEGDMA used here, studies have shown that microgels will form at the early stage of the reaction.[205–209] The higher reactivity of divinyl crosslinker (TEGDMA in this study) causes appreciable cyclization reaction at the beginning stage, which leads to internal crosslinked microgels. Some of these microgels are accumulated around the nucleated water droplets as schematically illustrated in Figure 5.8. Because the density of water droplets (1.0 g/cm^3) is lower than that of CS_2 (1.26 g/cm^3), they would not normally sink into the evaporative solution to form the random pores observed in the Figure 5.6c. However, during the fast evaporation of the CS_2, Marangoni convection can actively transport most of the microgels together with the water droplets from center to edge of the solution drop. Thus the effective concentration of the microgels is higher near the contact lines than that at the center of the solution drop.

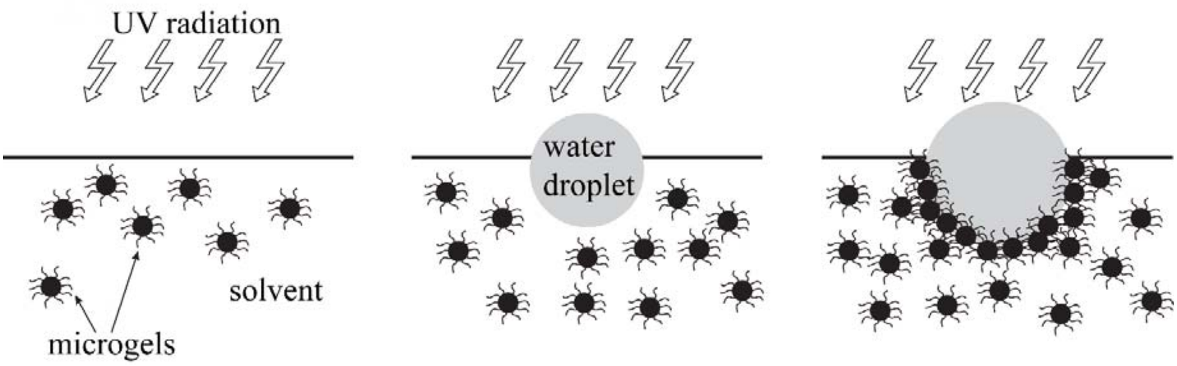

Figure 5.8 Schematic illustration of the simultaneous photocrosslinking of the MMA/TEGDMA and the condensation of water droplets.

During the evaporation of CS_2, the contact line of the solution is pinned, possible due to both surface roughness of the substrate and the deposition of the microgels.[69,210] The pinning effect depends on the initial contact angle of the deposited solution on the PET substrate.[211] It is the combination of higher polymer (microgels) concentration, the pinning effect, and fast evaporation at the peripheral area that leads to thicker films than the center of the drop, similar to that observed in other evaporated polymer films.[52] Correspondingly, the faster vitrification at the peripheral region also helps to limit the growth and coalescence of the trapped water droplets.[212,213] In contrast, the delayed gelation/vitrification at the center region results in more growth and coalescence of the water droplets, and thus the larger and polydisperse pores.[213,214]

Figure 5.6e shows that the inner surfaces of the crosslinked pores, obtained after peeling off the top layer film with a scotch tape, were rough, which is similar to that resulted from tBA/chloroform solution (Section 5.3.1). For comparison, we prepared a BF film using PS/CS_2. Interestingly, the inner surfaces of the honeycomb pores of PS films fabricated by the BF technique were smooth (Figure 5.6f), indicating that the rough inner surface of MMA/TEGDMA and tBA/TEGDMA (Section 5.3.1) pores was unlikely caused by the shrinkage stress induced by the solvent evaporation. The more plausible reason is that the initial crosslinked polymers surrounding the water droplets were likely resulted from the coagulation/reaction of microgels as discussed above. It is worth noting that during the vitrification, *i.e.* the coagulation and reaction of the microgels (which contains reactive centers), only pendant vinyls at the microgel surfaces reacted because of steric hindrance[205], leading to the residual unreacted vinyl groups in fabricated films (Figure 5.5).

For the samples containing 90 wt.% MMA, the morphology of the pores was much less uniform than that of the other compositions. At the peripheral region of the films, fibrous structures with highly opened pores were obtained (Figure 5.9a). At the center of the films, hierarchical fibrous structures were obtained with a broad distribution of pore sizes. It is known that the crosslinker, TEGDMA, has a higher reactivity than the MMA[205,206]. With the increase of MMA composition, the overall photo-induced polymerization rate is reduced[205,206], which allows significant condensed the water droplets. Consistently, similar morphology was observed for a formulation with 100% MMA, using the current technique (image not shown). Since the center of the films gelled/vitrified much slower than the edges, some water droplets grew into nearly 100 μm in diameter (Figure 5.9b).

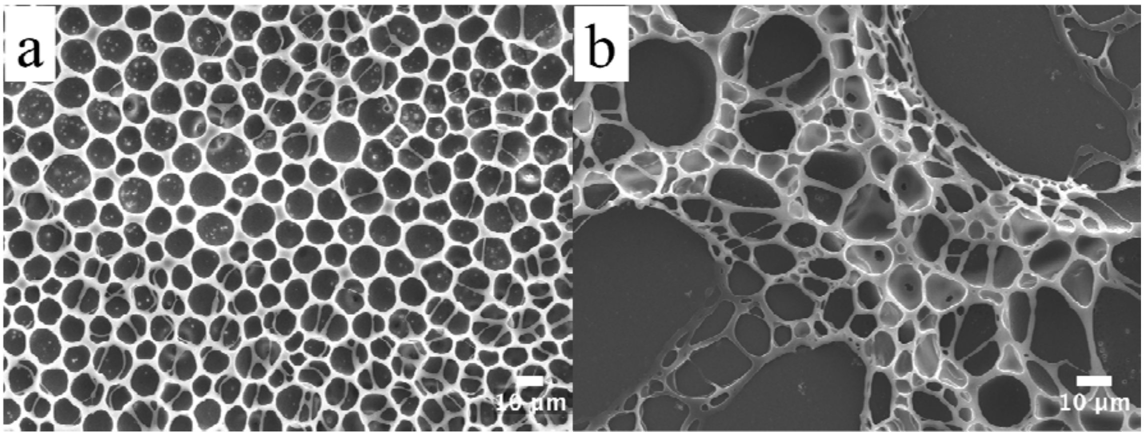

Figure 5.9 SEM images of the fabricated film with a 90/10 wt./wt. MMA/TEGDMA composition, using BF methods under simultaneous ~ 5.4 mW/cm^2 UV radiation and 2 L/min moisturized N_2 flow, at (a) peripheral and (b) center regions of the film.

Figure 5.10a summaries the geometric information of the pores, including circularity and diameter of the pores, as a function of the MMA composition. Note that the values of the MMA composition correspond to that used in the reaction mixture and are nearly identical to that in the fabricated films because of the high conversion as shown in Figure 5.5. In addition, Figure 5.10b shows the calculated entropy from the Voronoi analysis (see Section 3.2) for all the porous films at the peripheral regions, which characterizes the degree of order of the pores. Clearly, there is no dramatic difference between the pore morphology for MMA composition between 50 wt.% and 80 wt.%. On the other hand, films containing 90 wt.% MMA clearly shows lower circularity and larger entropy.

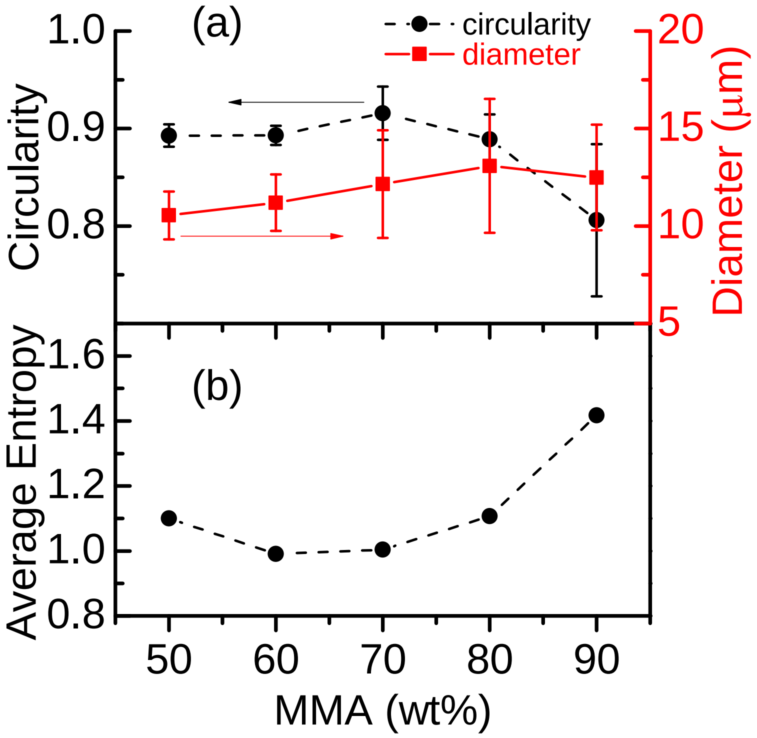

Figure 5.10 (a) Circularity and diameter of the pores for the porous films with varying MMA compositions. The error bars are the standard deviation from averaging over 3 different SEM images. (b) The entropy of the pores for the porous films with varying MMA composition, estimated using the Voronoi method.

The similarity in morphology of the pores for all the samples except that containing 90 wt.% MMA suggests that the fixation of the BF morphology is largely dictated by the solvent evaporation rate. In other words, it is the solvent evaporation that leads to the gelation of the crosslinked film, similar to the non-reactive systems. Since all the samples have identical concentrations, the gelation times are similar. This is different from the conventional gelation time in the crosslinking process of the bulk samples, which is largely controlled by the reactivity of the monomer/crosslinker, and thus is highly sensitive to the monomer/crosslinker ratio.

5.3.3 Hierarchical morphology prepared from NOA65/CS_2 solution system: formation of a BF structured skin layer atop of a particulate layer

In addition to the acrylate-based systems, we also applied this synthesis/fabrication strategy to a commercially available reactive resin, NOA65. For this system, CS_2 was adopted as the solvent for the BF formation, with a NOA65 concentration of 10 % by weight. The processing conditions for this sample are ~ 6 mW/cm^2 UV radiation and 5 L/min moisturized N_2 flow for 3 min (Table 5.1). Despite its significantly different chemical composition, NOA65 also demonstrates successful BF formations during the *in situ* crosslinking of the monomers upon UV radiation. Different from the acrylate-based systems, the processing of the NOA65/CS_2 solutions was carried out on glass slides, to utilize the good adhesion between the glass slides and NOA65 films. From the SEM images, the pores resulted from the BFs appear quite uniform (Figure 5.11). The FFT analysis reveals that the degree of ordering of the pores is high for the NOA65 films (Figure 5.11, insets). The pores of NOA65 film have average diameter of 1.2 ± 0.2 μm, circularity of 0.90 ± 0.03 and surface coverage of ~ 27.2 %. These pores are much smaller and have less surface coverage than that of the acrylate-based systems (see Section 5.3.1 and 5.3.2).

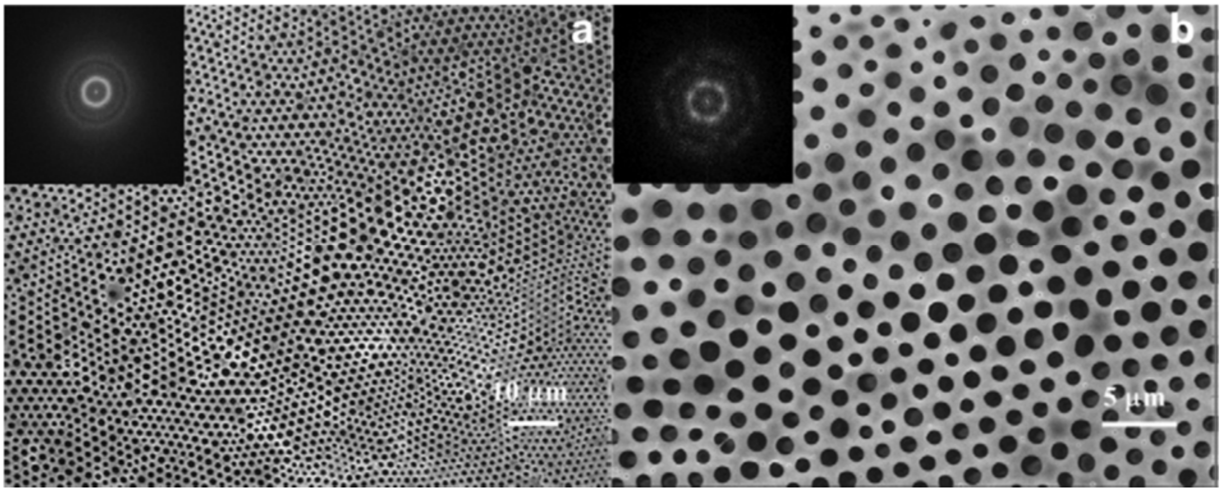

Figure 5.11 SEM images of the porous structures in a crosslinked NOA65 film prepared from 10 wt.% NOA65/CS_2 solution using the BF methods under simultaneous 6 mW/cm^2 UV radiation and 5 L/min moisturized N_2 flow for 3 min, with a) a larger and b) a closer view. Insets are the FFT images of the corresponding SEM images.

Viewing from the cross-section of fractured sample (Figure 5.12), we observed a BF structured skin layer capping atop of an agglomeration of microparticles. This hierarchical structure (skin layer/particulate layer) is same to the NOA65/CS_2 film prepared under the dry N_2 flow in general (Section 4.3). Interestingly, the thickness of skin layer in Figure 5.12 is much smaller (21 µm) than that prepared under similar conditions but dry N_2 flow (see Figure 4.3a, which shows a skin layer of 72 µm). The significant reduction in skin layer thickness can be attributed to the reduced evaporation rate of CS_2 (e.g. Figure 4.2 shows skin layer thickness increases as evaporation rate increases), which is due to its reduced partial vapor pressure in the presence of moisture in the moving N_2. Nonetheless, the skin layer formation, along with the fast reaction rate of NOA65, lead to earlier onset of gelation that significantly limits the growth/coalescence of water droplets. Such characteristics of NOA65/CS_2 precursor solution therefore accounts for the smaller diameter, higher regularity, and lower surface coverage of the pores in Figure 5.11, as compared to BF films prepared from acrylate-based precursors in Section 5.3.1 and 5.3.2.

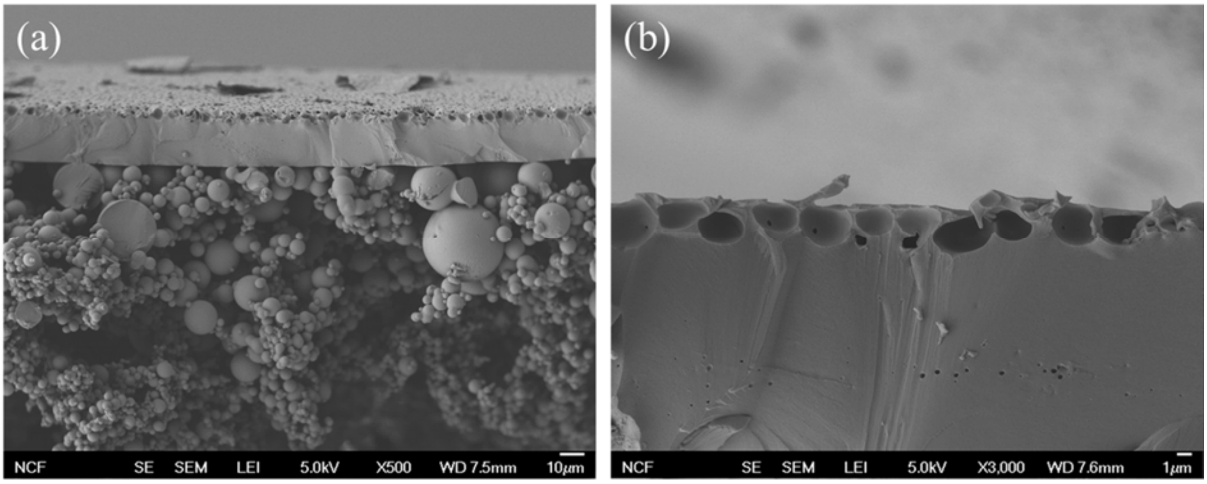

Figure 5.12 Cross-sectional view SEM images of a crosslinked NOA65 film prepared from 10 wt.% NOA65/CS_2 solution using the BF methods under simultaneous 6 mW/cm^2 UV radiation and 5 L/min moisturized N_2 flow for 3 min, with a) a larger and b) a closer view.

5.4 Characterizations of thermo-mechanical properties of the porous films

The BF-templated porous films prepared from linear polymers exhibit enhanced water resistance, thus are promising to be used as water repellent surface.[33,215] In addition, the *in situ* crosslinking reaction incorporated into the BF-templated porous films by our method may exhibit extra advantages such as enhanced solvent and thermal resistance and extended rubbery regions at high temperature. Therefore, in the following, we will present the results regarding the above-mentioned advantages through the characterizations of the thermo-mechanical properties of the crosslinked MMA/TEGDMA films from Section 5.3.2.

The T_g of polymers often defines the temperature range that the materials can be applied to, as their mechanical properties change dramatically as temperature pass across the T_g. Here, the T_g of the crosslinked walls (a few μm wide) between neighboring pores was *in situ* measured with a nano-thermal analysis (Nano-TA) method.[120] As shown in Figure 5.13, with the increase of MMA composition, the T_g of the porous films increased from ~ 97 °C to ~ 113 °C, with the exception of the sample containing 80 wt.% MMA. Figure 5.13 also includes the T_g value of the bulk MMA/TEGDMA films from nano-TA measurements. No statistically significant difference between the porous films and the dense films was observed. Note that these bulk samples were post-cured for 60 min at 90 °C following the UV-induced crosslinking, which is necessary for thick samples[121].

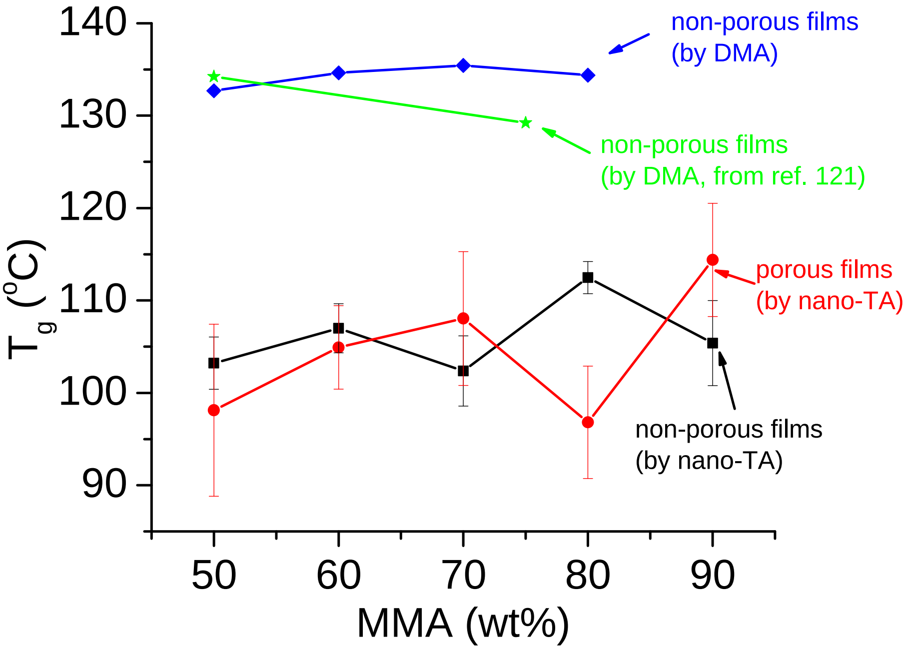

Figure 5.13 T_g of the crosslinked porous films (circle symbols), and of non-porous films (square symbols) as a function of the MMA composition, determined by nano-TA. T_g of the non-porous films (star and diamond symbols) by DMA. The values and error bars represent statistical average from 5 different measurements.

For all porous samples, we did examine the influence of post-curing using the same protocol and did not find any difference in the FTIR spectra of the post-cured samples compared with the as cast ones. This is most likely due to the thickness of porous samples after drying (up to 50 µm) was considered "optically thin", and the UV exposure time used was sufficient to crosslink the film to a high degree. However, the thick samples were "optically thick" which limited the conversion of the monomers and thus required post-curing[121]. The observed similarity in T_g between the thin porous films and that of thick post-cured films is consistent with the observed high conversions of both samples, despite their different crosslinking environments.

However, these T_g values from nano-TA measurement are ~ 30 °C lower than that of the bulk films determined by DMA (Figure 5.13). Note that our DMA-determined T_g values well agree with that reported elsewhere for the same MMA/TEGDMA systems.[121] Such a discrepancy reflects the complex nature of the glass transition process, *i.e.* T_g value highly depends on the characterization methods. From literature, it has been shown that the T_g value of crosslinked epoxy films, obtained from the peak of the loss (tanδ) in the DMA measurement, was more than 20 °C higher than that obtained from thermal expansion and DSC[216]. Nevertheless, Figure 5.13 confirms that the porous films had similar T_g with that of bulk samples obtained directly from photo-polymerization. The result suggests that the photo-induced crosslinking of these reactive mixtures, despite the extremely complex and dynamic environment, does result in films that have similar physical properties to the bulk ones. Note that although the range of T_g for the current MMA/TEGDMA is relatively narrow (Figure 5.13), a much broad range is possible by the use of larger molecular weight EGDMA crosslinkers[121].

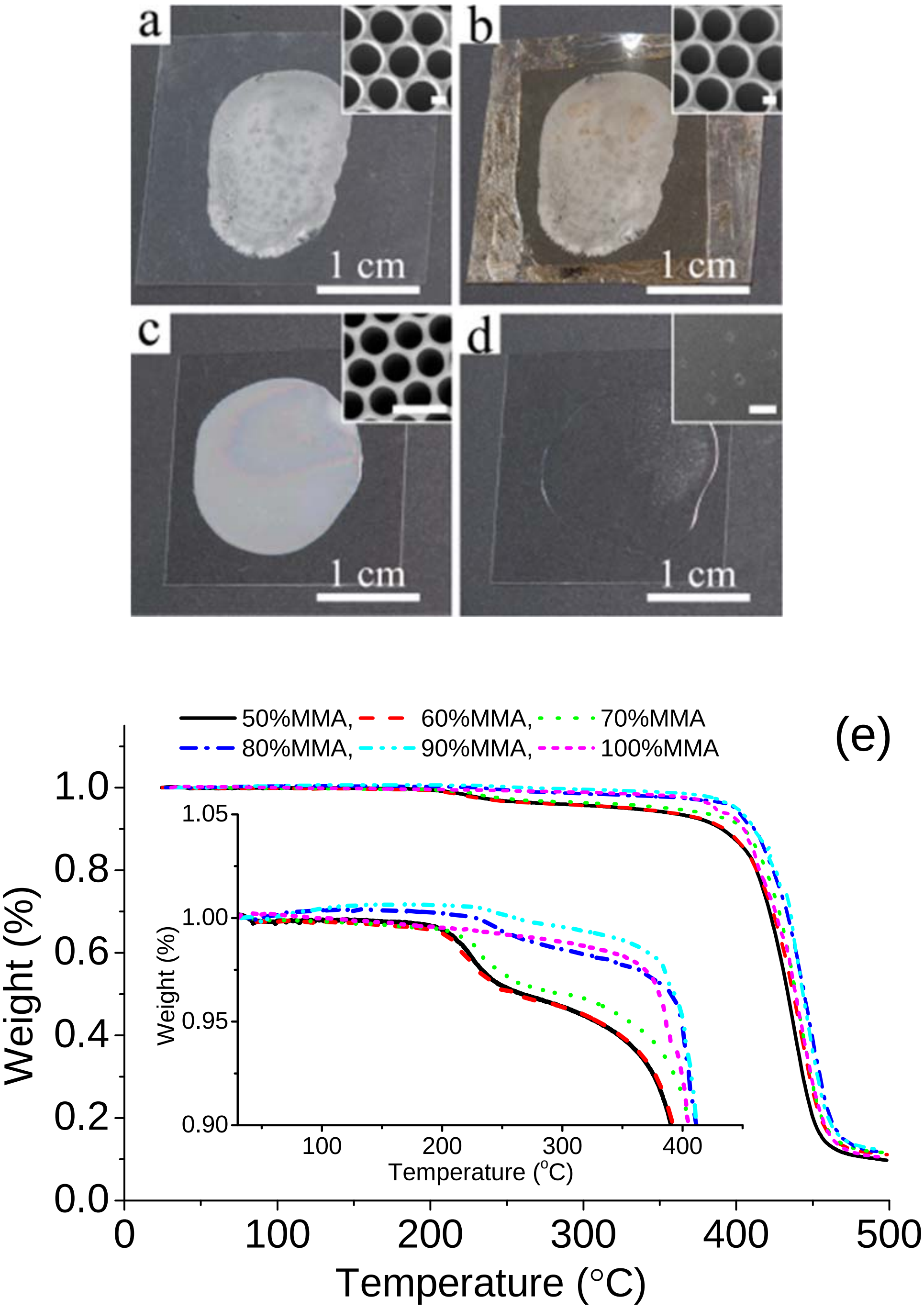

Figure 5.14 Optical images of the crosslinked porous films (a) before, and (b) after being annealed at 220 °C for 30 min. Similarly, (c) and (d) are the images of porous PS films (M_w ~ 50 kg/mol, casted on the microscopic glass slide from 1 wt.% CS_2 solution under 0.5 L/m moist flow) before and after being annealed at 130 °C for 30 min. The insets are the representative SEM images (scale bar: 5 μm). (e) TGA curves of the crosslinked porous films supported on PET, showing the mass of the film as a function of temperature. The inset is the magnified view of the initial portion of the TGA curves.

As stated earlier, porous crosslinked films possess high structural stability in comparison to the non-crosslinked ones. The solvent resistance of the fabricated films were confirmed by soaking them in common solvents for (meth)acrylate polymers including CS_2, chloroform, and toluene, each for 15 min. For all the samples, no noticeable morphological changes were observed both visually and under optical microscope. Furthermore, we heated the porous films supported on the PET on a hot stage (STC200, Instec), from room temperature to 220 °C at a 10 °C/min rate, and remained at 220 °C for 30 min. Both the PET substrate and the double-side tape, used to prevent the curving of PET films during the heating, showed clear chemical degradations judging from their color changes (Figure 5.14b). However, the porous structure remained intact from the SEM measurements (insets in Figure 5.14a and b). In comparison, a honeycomb porous PS film (Figure 5.14c), fabricated using the BF method, was heated to 130 °C at a rate of 10 °C/min, and remained at 130 °C for 30 min (Figure 5.14d). After the thermal annealing, a dense, almost transparent PS film was obtained (Figure 5.14d), and SEM revealed only traces of much smaller pores that were not completely collapsed (inset of Figure 5.14d).

In addition, we examined the degradation of the porous films with thermogravimetric analyzer (TGA), which defines the upper temperature limit for the applications of these films. As shown in Figure 5.14e, two temperature regions of mass loss were observed: one ranged from 200 to 250 °C, and the other started around 380 °C. The higher temperature mass loss is mainly associated with the pyrolysis of PET substrate, consistent with the TGA measurements on pure PET (not shown). The lower temperature mass loss came from the porous MMA/TEGDMA films, whose total mass was much smaller than that of the PET substrate. Therefore, the total amount of mass loss below 300 °C was small. With the increase of MMA composition, the amount of mass loss at this temperature range decreased, which indicates that the chemical degradation is most likely related to the TEGDMA units. For 100% MMA, no mass loss was observed in this region, and degradation started to occur at around 380 - 400 °C, which coincides with that of the PET substrate. Therefore, more TEGDMA in the crosslinked porous films leads to larger degree of degradation at low temperature, which is consistent with literature report on the bulk films[217].

Water contact angle (CA) is commonly used to characterize the surface properties of the BF-templated porous films. Figure 5.15 shows the CA on all the fabricated porous films, measured by the sessile droplet method. In comparison, CA on flat bulk crosslinked films was also determined, which shows slight increase with the increase of MMA composition. Note that the CA on pure PMMA is ~73 °, slightly higher than the film containing 90 wt.% MMA (~ 71 °). This is consistent with the fact that MMA unit is slightly more hydrophobic than the TEGDMA unit that contains four hydrophilic ethylene oxide groups (-CH_2O-). Most significantly, the CA of the crosslinked porous films was more than 50 ° higher than that of the flat films. From literature, the water CAs on the honeycomb polymer films and on the pincushion films obtained after peeling the top film off were correspondingly, 20 – 30 °, and ~ 60 ° higher than that of the flat films.[46,218,219] Such a dramatic increase in the apparent water CA on rough surfaces is often described as the Cassie-Baxter type wetting, where air pockets are trapped between the water and sample surface.[220] Accordingly, we estimated the surface coverage of the pores using Cassie-Baxter equation:

$$\cos\theta = f_s \cos\theta^* - f_{air} \qquad \text{Eqn 5.2}$$

where θ is the apparent water CA on rough surface, θ^* is the intrinsic water CA on a flat surface, f_s and f_{air} are the normalized area of solid-liquid and liquid-air interfaces, respectively. Quantitatively, the, the pore coverage is 0.64 - 0.70 for all the films, which is slightly larger than that estimated from the SEM images (0.5 - 0.7) (Figure 5.6). The slight discrepancies may be caused by distribution of the pores and other roughness.

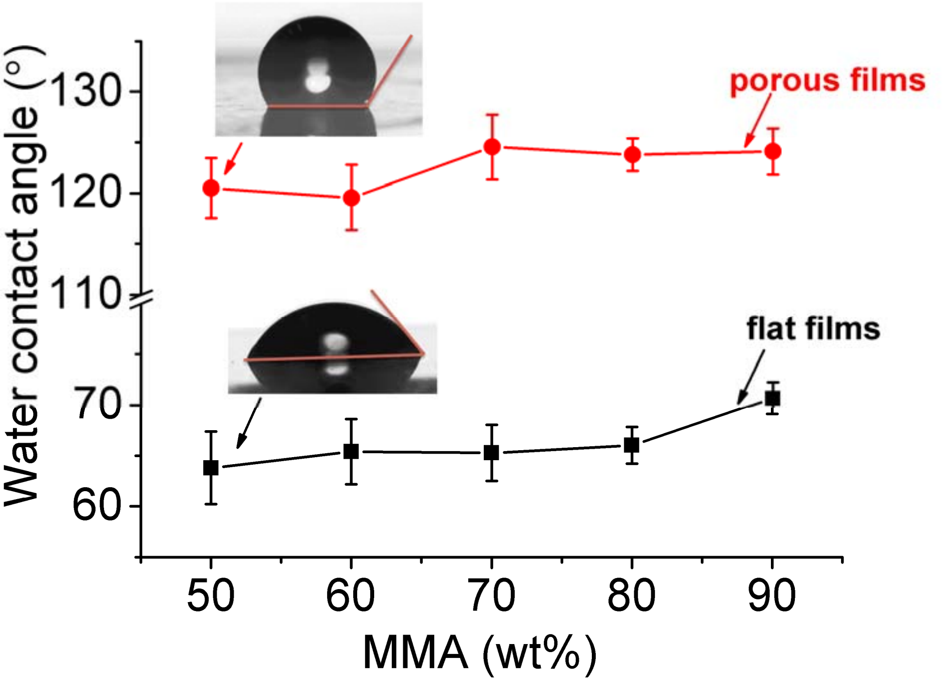

Figure 5.15 Water contact angle on the crosslinked porous films (circle symbols) and the corresponding flat films (square symbols). Insets are the representative images of the sessile water droplets on the surfaces of the sample containing 50 wt.% MMA. The error bars represent the standard deviation from 5 different measurements.

5.5 Conclusions

In this chapter, we demonstrated a new and simple strategy to directly create micro-sized pores with honeycomb like morphology into crosslinked polymer networks. This is achieved by photo-induced crosslinking of reactive monomers within highly evaporative solutions in the presence of water vapor. It is clear that the reaction/crosslink reaction employed has to have a comparable time scale than that of the BF formation, and not to require or generate large amount heat during the reaction. Compared with the earlier-mentioned methods that require post-curing to form crosslinked films, the current method is applicable to a broad range of network-forming materials including tBA in chloroform, MMA in CS_2 and a NOA65 resin in CS_2. The obtained materials showed relatively long-range order and regular BF. The characteristics of the BF-templated film morphology strongly depend on the processing conditions and precursor compositions and thus tunable for targeting specific applications. For the films obtained from BFTA process without initial spin, the pore morphology at the peripheral regions was found more uniform and ordered than that at the center region. Such a difference is attributed to the interplay between the photocrosslinking reaction in solution, the contact line pinning and mass transport within the solution. Therefore a better control on the process variables (*i.e.* the use spin coating or blade cast) could improve the control over the characteristics of the BF formations.

We further characterized the thermo-mechanical properties of the porous MMA/TEGDMA films with varying MMA/TEGDMA ratios. The T_g values of these films were found to be identical to that of the flat dense films with identical compositions, which is consistent with the observed high conversion of the carbon-carbon double bonds. In contrast, the degree of chemical degradation for the porous films did increase with the increase of TEGDMA composition, caused by the lower thermal stability of the TEGDMA compared with MMA units. Regardless of the MMA composition, these porous structures remained intact even after being annealed at 220 °C for 30 min, providing significant improvement in thermal stability over uncrosslinked polymer porous films.

6 SUMMARY AND PROSPECTS

6.1 Summary of research

In this dissertation, we develop a simple one-step fabrication process to create microstructures in crosslinked polymers by *in situ* photocrosslinking of precursors during the evaporation of solvents.

Under forced convection, the fast evaporation of solvent at the air-solution interface generates a concentration gradient which polymerizes/crosslinks into a skin layer. Once this skin layer forms, it greatly reduces the diffusivity of solvent within the drop to arrive at the air-solution interface, therefore slowing down the evaporation rate. This skin layer can continuously grow downwards when no phase separation occurs within the skin-layer capped solution, resulting in a homogeneous polymer film. In contrast, if phase separation indeed occurs between growing polymers and solvent due to the discrepancies in the polarity contributions, *i.e.* a pair of polar (non-polar) precursor and non-polar (polar) solvent, a hierarchical film is formed featuring a dense skin layer atop of a particulate layer.

For the first time, the polymer skin layer formed during the evaporation can be obtained after the evaporation, in contrast to the linear polymer solutions. The final thickness of the skin layer is dependent on the processing parameters including the N_2 flow rate, UV intensity and initial precursor concentration. A theoretical model, based on the one for the non-crosslinked polymer solution, is developed that can successfully describe the skin layer formation and its dependence on these processing parameters. These findings provide a mechanistic understanding of the photocrosslinking process under evaporative environments, which enable us to prepare hydrogels with microstructured morphologies from a variety of commonly used hydrogel-forming monomers including *N*-isopropylacrylamide, 2-hydroxyethyl methacrylate, acrylamide, and acrylic acid.

Extending this method further by switching dry N_2 flow to moisturized N_2 flow, we successfully create micron-sized pores with honeycomb-like morphology into crosslinked polymer networks. This is achieved by photo-induced crosslinking of reactive monomers within highly evaporative solutions in the presence of water vapor. Compared with the earlier-mentioned methods that requires post-curing to form crosslinked films, we demonstrate that this method is applicable to a broad range of network-forming materials such as tert-butyl acrylate and methyl methacrylate systems and thiol-ene based systems. By planarizing solution drop and/or using dilute precursor solution, the emergence of skin layer at the surface was suppressed in favor of formatting high quality breath figure structured pores that showed relatively long rang order. The characteristics of the BF structured pores including pore size, degree of ordering, surface coverage strongly depends on the external conditions. On the contrary, the pore morphology remains similar despite varying precursor compositions, which suggests solvent evaporation is the determining factor for the gelation time that fixes the breath figure morphology, similar to that of conventional non-reactive BF process. For samples prepared without initial planarizing step, the pore morphology at the peripheral areas was found more uniform and ordered than that at the center area, which can be attributed to the interplay between the photocrosslinking reaction in solution, the contact line pinning and mass transport within the solution. In addition, these porous films exhibit enhanced thermal and solvent resistance as compared to linear counterparts.

6.2 Future research directions

The processing method we developed to prepare crosslinked microstructured polymer films, by photocrosslinking of precursors during the evaporation of the solvent, is a highly dynamic, convoluted process. With this dissertation in place, continued work will help further elevate the understanding of this process that enables us to better control the final film morphologies. Therefore, the following research directions are suggested:

(1) The current theoretical framework of the evaporating polymer solution was developed with some simplifications. First of all, the diffusion coefficient of solution is assumed constant, which in reality vary dramatically due to the change of solution concentration and/or evaporation induced temperature change. As the evaporation of solvent progresses, the guiding equation at certain point may be no longer effective. Secondly, a one-dimensional diffusion model is used. In fact, the lateral stress imposed by temperature induced Marangoni convection in some systems may markedly alter diffusion in the vertical direction. Therefore, a modified model addressing all these problems is highly desired.

(2) RIPS in evaporating solvents can form particulate layers *via* nucleation and growth mechanism. We demonstrate the possibility of dispersing and harvesting these particles. Beyond this, we may prepare core-shell or hollow micro-sized particles by addition of nucleating agents in the casting solution. Envisioned nucleating agents include silica particles in tens of nm to hundreds of nm, or crystallizable species (*i.e.* liquid crystals) that can quickly crystallize in the beginning of the process due the cooling effect by solvent evaporation, or even species that forms clusters or micelles (*i.e.* small molecule organogelators) *via* hydrophobic interactions or hydrogen bonding. Since the processing is time dependent, the formation time of a critical nucleus by nucleating agents is significantly important. For an instance, if the crystallization of

nucleating agents is too slow as compared to the formation of polymer nuclei, the crystalizing centers might be bypassed and homogeneous nucleation will take place instead and thus no core-shell structures will form eventually. Once the core-shell particles are obtained, the preparation of hollow particles will be simply by dissolving the core *via* solution elution or calcination. This kind of core-shell or hollow micron-sized particles can be potentially used as drug delivery carriers or sensors.

BIBLIOGRAPHY

1. Nishikawa, T., Nonomura, M., Arai, K., Hayashi, J., Sawadaishi, T., Nishiura, Y., Hara, M. & Shimomura, M. Micropatterns Based on Deformation of a Viscoelastic Honeycomb Mesh. *Langmuir* **19,** 6193–6201 (2003).

2. Beattie, D., Wong, K. H., Williams, C., Poole-Warren, L. A., Davis, T. P., Barner-Kowollik, C. & Stenzel, M. H. Honeycomb-Structured Porous Films from Polypyrrole-Containing Block Copolymers Prepared via RAFT Polymerization as a Scaffold for Cell Growth. *Biomacromolecules* **7,** 1072–1082 (2006).

3. Zhu, Y., Sheng, R., Luo, T., Li, H., Sun, J., Chen, S., Sun, W. & Cao, A. Honeycomb-Structured Films by Multifunctional Amphiphilic Biodegradable Copolymers: Surface Morphology Control and Biomedical Application as Scaffolds for Cell Growth. *ACS Appl. Mater. Interfaces* **3,** 2487–2495 (2011).

4. Oxley, H. R., Corkhill, P. H., Fitton, J. H. & Tighe, B. J. Macroporous hydrogels for biomedical applications: methodology and morphology. *Biomaterials* **14,** 1064–1072 (1993).

5. Lévesque, S. G., Lim, R. M. & Shoichet, M. S. Macroporous interconnected dextran scaffolds of controlled porosity for tissue-engineering applications. *Biomaterials* **26,** 7436–7446 (2005).

6. Cavalieri, F., Chiessi, E., Villa, R., Viganò, L., Zaffaroni, N., Telling, M. F. & Paradossi, G. Novel PVA-Based Hydrogel Microparticles for Doxorubicin Delivery. *Biomacromolecules* **9,** 1967–1973 (2008).

7. Wijnhoven, J. E. G. J. & Vos, W. L. Preparation of Photonic Crystals Made of Air Spheres in Titania. *Science* **281,** 802–804 (1998).

8. Noda, S., Chutinan, A. & Imada, M. Trapping and emission of photons by a single defect in a photonic bandgap structure. *Nature* **407,** 608–610 (2000).

9. Imada, M., Noda, S., Chutinan, A., Tokuda, T., Murata, M. & Sasaki, G. Coherent two-dimensional lasing action in surface-emitting laser with triangular-lattice photonic crystal structure. *Appl. Phys. Lett.* **75,** 316–318 (1999).

10. Hedrick, J. L., Miller, R. D., Hawker, C. J., Carter, K. R., Volksen, W., Yoon, D. Y. & Trollsås, M. Templating Nanoporosity in Thin-Film Dielectric Insulators. *Adv. Mater.* **10,** 1049–1053 (1998).

11. Wan, L.-S., Li, J.-W., Ke, B.-B. & Xu, Z.-K. Ordered Microporous Membranes Templated by Breath Figures for Size-Selective Separation. *J. Am. Chem. Soc.* **134,** 95–98 (2012).

12. Owens, D. E., Jian, Y., Fang, J. E., Slaughter, B. V., Chen, Y.-H. & Peppas, N. A. Thermally Responsive Swelling Properties of Polyacrylamide/Poly(acrylic acid) Interpenetrating Polymer Network Nanoparticles. *Macromolecules* **40,** 7306–7310 (2007).

13. Drummond, R. K., Klier, J., Alameda, J. A. & Peppas, N. A. Preparation of poly(methacrylic acid-g-ethylene oxide) microspheres. *Macromolecules* **22,** 3816–3818 (1989).

14. Pelton, R. H. & Chibante, P. Preparation of aqueous latices with N-isopropylacrylamide. *Colloids Surf.* **20,** 247–256 (1986).

15. Leobandung, W., Ichikawa, H., Fukumori, Y. & Peppas, N. A. Monodisperse nanoparticles of poly(ethylene glycol) macromers and N-isopropyl acrylamide for biomedical applications. *J. Appl. Polym. Sci.* **87,** 1678–1684 (2003).

16. Revzin, A., Russell, R. J., Yadavalli, V. K., Koh, W.-G., Deister, C., Hile, D. D., Mellott, M. B. & Pishko, M. V. Fabrication of Poly(ethylene glycol) Hydrogel Microstructures Using Photolithography. *Langmuir* **17,** 5440–5447 (2001).

17. Diez, M., Mela, P., Seshan, V., Möller, M. & Lensen, M. C. Nanomolding of PEG-Based Hydrogels with Sub-10-nm Resolution. *Small* **5,** 2756–2760 (2009).

18. Rolland, J. P., Maynor, B. W., Euliss, L. E., Exner, A. E., Denison, G. M. & DeSimone, J. M. Direct Fabrication and Harvesting of Monodisperse, Shape-Specific Nanobiomaterials. *J. Am. Chem. Soc.* **127,** 10096–10100 (2005).

19. Xu, S., Nie, Z., Seo, M., Lewis, P., Kumacheva, E., Stone, H. A., Garstecki, P., Weibel, D. B., Gitlin, I. & Whitesides, G. M. Generation of Monodisperse Particles by Using Microfluidics: Control over Size, Shape, and Composition. *Angew. Chem. Int. Ed.* **44,** 724–728 (2005).

20. Singamaneni, S., Bertoldi, K., Chang, S., Jang, J.-H., Young, S. L., Thomas, E. L., Boyce, M. C. & Tsukruk, V. V. Bifurcated Mechanical Behavior of Deformed Periodic Porous Solids. *Adv. Funct. Mater.* **19,** 1426–1436 (2009).

21. Singamaneni, S., Bertoldi, K., Chang, S., Jang, J.-H., Thomas, E. L., Boyce, M. C. & Tsukruk, V. V. Instabilities and Pattern Transformation in Periodic, Porous Elastoplastic Solid Coatings. *ACS Appl. Mater. Interfaces* **1,** 42–47 (2009).

22. Jang, J.-H., Koh, C. Y., Bertoldi, K., Boyce, M. C. & Thomas, E. L. Combining Pattern Instability and Shape-Memory Hysteresis for Phononic Switching. *Nano Lett.* **9,** 2113–2119 (2009).

23. Kang, J.-H., Moon, J. H., Lee, S.-K., Park, S.-G., Jang, S. G., Yang, S. & Yang, S.-M. Thermoresponsive Hydrogel Photonic Crystals by Three-Dimensional Holographic Lithography. *Adv. Mater.* **20,** 3061–3065 (2008).

24. Yang, S., Megens, M., Aizenberg, J., Wiltzius, P., Chaikin, P. M. & Russel, W. B. Creating Periodic Three-Dimensional Structures by Multibeam Interference of Visible Laser. *Chem. Mater.* **14,** 2831–2833 (2002).

25. Simkevitz, S. L. & Naguib, H. E. Fabrication and Analysis of Porous Shape Memory Polymer and Nanocomposites. *High Perform. Polym.* **22,** 159–183 (2010).

26. Kiefer, J., Hilborn, J. G., Månson, J. A. E., Leterrier, Y. & Hedrick, J. L. Macroporous Epoxy Networks via Chemically Induced Phase Separation. *Macromolecules* **29,** 4158–4160 (1996).

27. Okay, O. Macroporous copolymer networks. *Prog. Polym. Sci.* **25,** 711–779 (2000).

28. Luo, Y.-S., Cheng, K.-C., Huang, N.-D., Chiang, W.-P. & Li, S.-F. Preparation of porous crosslinked polymers with different surface morphologies via chemically induced phase separation. *J. Polym. Sci. Part B Polym. Phys.* **49,** 1022–1030 (2011).

29. Hong, S. W., Xu, J. & Lin, Z. Template-Assisted Formation of Gradient Concentric Gold Rings. *Nano Lett.* **6,** 2949–2954 (2006).

30. Xu, J., Xia, J., Hong, S. W., Lin, Z., Qiu, F. & Yang, Y. Self-Assembly of Gradient Concentric Rings via Solvent Evaporation from a Capillary Bridge. *Phys. Rev. Lett.* **96,** 066104 (2006).

31. Han, W. & Lin, Z. Learning from 'Coffee Rings': Ordered Structures Enabled by Controlled Evaporative Self-Assembly. *Angew. Chem. Int. Ed.* **51,** 1534–1546 (2012).

32. Widawski, G., Rawiso, M. & François, B. Self-organized honeycomb morphology of star-polymer polystyrene films. *Nature* **369,** 387–389 (1994).

33. Bunz, U. H. F. Breath Figures as a Dynamic Templating Method for Polymers and Nanomaterials. *Adv. Mater.* **18,** 973–989 (2006).

34. Song, L., Bly, R. K., Wilson, J. N., Bakbak, S., Park, J. O., Srinivasarao, M. & Bunz, U. H. F. Facile Microstructuring of Organic Semiconducting Polymers by the Breath Figure Method: Hexagonally Ordered Bubble Arrays in Rigid Rod-Polymers. *Adv. Mater.* **16,** 115–118 (2004).

35. Srinivasarao, M., Collings, D., Philips, A. & Patel, S. Three-Dimensionally Ordered Array of Air Bubbles in a Polymer Film. *Science* **292,** 79–83 (2001).

36. Sharma, V., Song, L., Jones, R. L., Barrow, M. S., Williams, P. R. & Srinivasarao, M. Effect of solvent choice on breath-figure-templated assembly of. *EPL Europhys. Lett.* **91,** 38001 (2010).

37. Li, L., Li, J., Zhong, Y., Chen, C., Ben, Y., Gong, J. & Ma, Z. Formation of ceramic microstructures: honeycomb patterned polymer films as structure-directing agent. *J. Mater. Chem.* **20,** 5446–5453 (2010).

38. Ma, C.-Y., Zhong, Y.-W., Li, J., Chen, C.-K., Gong, J.-L., Xie, S.-Y., Li, L. & Ma, Z. Patterned Carbon Nanotubes with Adjustable Array: A Functional Breath Figure Approach. *Chem. Mater.* **22,** 2367–2374 (2010).

39. Li, L., Zhong, Y., Li, J., Chen, C., Zhang, A., Xu, J. & Ma, Z. Thermally stable and solvent resistant honeycomb structured polystyrene films via photochemical cross-linking. *J. Mater. Chem.* **19,** 7222–7227 (2009).

40. Li, L., Chen, C., Zhang, A., Liu, X., Cui, K., Huang, J., Ma, Z. & Han, Z. Fabrication of robust honeycomb polymer films: A facile photochemical cross-linking process. *J. Colloid Interface Sci.* **331,** 446–452 (2009).

41. Ding, J., Zhang, A., Bai, H., Li, L., Li, J. & Ma, Z. Breath figure in non-aqueous vapor. *Soft Matter* **9,** 506–514 (2012).

42. Yabu, H., Tanaka, M., Ijiro, K. & Shimomura, M. Preparation of Honeycomb-Patterned Polyimide Films by Self-Organization. *Langmuir* **19,** 6297–6300 (2003).

43. Erdogan, B., Song, L., Wilson, J. N., Park, J. O., Srinivasarao, M. & Bunz, U. H. F. Permanent Bubble Arrays from a Cross-Linked Poly(para-phenyleneethynylene): Picoliter Holes without Microfabrication. *J. Am. Chem. Soc.* **126,** 3678–3679 (2004).

44. Kabuto, T., Hashimoto, Y. & Karthaus, O. Thermally Stable and Solvent Resistant Mesoporous Honeycomb Films from a Crosslinkable Polymer. *Adv. Funct. Mater.* **17,** 3569–3573 (2007).

45. Karthaus, O., Hashimoto, Y., Kon, K. & Tsuriga, Y. Solvent Resistant Honeycomb Films from Photo-Crosslinkable Polycinnamate. *Macromol. Rapid Commun.* **28,** 962–965 (2007).

46. Nakamichi, Y., Hirai, Y., Yabu, H. & Shimomura, M. Fabrication of patterned and anisotropic porous films based on photo-cross-linking of poly(1,2-butadiene) honeycomb films. *J. Mater. Chem.* **21,** 3884–3889 (2011).

47. Yabu, H., Nakamichi, Y., Hirai, Y. & Shimomura, M. Robust anisotropic polymer meshes prepared by stretching and photo-crosslinking of poly(1,2-butadiene) honeycomb films. *Phys. Chem. Chem. Phys.* **13,** 4877–4880 (2011).

48. Li, L., Zhong, Y., Gong, J., Li, J., Huang, J. & Ma, Z. Fabrication of robust micro-patterned polymeric films via static breath-figure process and vulcanization. *J. Colloid Interface Sci.* **354,** 758–764 (2011).

49. Li, L., Zhong, Y., Gong, J., Li, J., Chen, C., Zeng, B. & Ma, Z. Constructing robust 3-dimensionally conformal micropatterns: vulcanization of honeycomb structured polymeric films. *Soft Matter* **7,** 546–552 (2011).

50. Vrentas, J. S. & Vrentas, C. M. Drying of solvent-coated polymer films. *J. Polym. Sci. Part B Polym. Phys.* **32,** 187–194 (1994).

51. Routh, A. F. & Russel, W. B. Horizontal drying fronts during solvent evaporation from latex films. *AIChE J.* **44,** 2088–2098 (1998).

52. De Gans, B.-J. & Schubert, U. S. Inkjet Printing of Well-Defined Polymer Dots and Arrays. *Langmuir* **20,** 7789–7793 (2004).

53. Kawase, T., Sirringhaus, H., Friend, R. H. & Shimoda, T. Inkjet Printed Via-Hole Interconnections and Resistors for All-Polymer Transistor Circuits. *Adv. Mater.* **13,** 1601–1605 (2001).

54. Gennes, P.-G. *Scaling Concepts in Polymer Physics*. (Cornell University Press, 1979).

55. Jung, Y., Kajiya, T., Yamaue, T. & Doi, M. Film Formation Kinetics in the Drying Process of Polymer Solution Enclosed by Bank. *Jpn. J. Appl. Phys.* **48,** 031502 (2009).

56. Guerrier, B., Bouchard, C., Allain, C. & Bénard, C. Drying kinetics of polymer films. *AIChE J.* **44,** 791–798 (1998).

57. Okuzono, T. & Doi, M. Effects of elasticity on drying processes of polymer solutions. *Phys. Rev. E* **77,** 030501 (2008).

58. Gennes, P. G. de. Solvent evaporation of spin cast films: 'crust' effects. *Eur. Phys. J. E* **7,** 31–34 (2002).

59. Okuzono, T., Ozawa, K. & Doi, M. Simple Model of Skin Formation Caused by Solvent Evaporation in Polymer Solutions. *Phys. Rev. Lett.* **97,** 136103 (2006).

60. Okazaki, M., Shioda, K., Masuda, K. & Toei, R. Drying Mechanism of Coated Film of Polymer Solution. *J. Chem. Eng. Jpn.* **7,** 99–105 (1974).

61. Ozawa, K., Okuzono, T. & Doi, M. Diffusion Process during Drying to Cause the Skin Formation in Polymer Solutions. *Jpn. J. Appl. Phys.* **45,** 8817 (2006).

62. Pauchard, L. & Allain, C. Buckling instability induced by polymer solution drying. *EPL Europhys. Lett.* **62,** 897 (2003).

63. Pauchard, L. & Allain, C. Mechanical instability induced by complex liquid desiccation. *Comptes Rendus Phys.* **4,** 231–239 (2003).

64. Shimokawa, Y., Kajiya, T., Sakai, K. & Doi, M. Measurement of the skin layer in the drying process of a polymer solution. *Phys. Rev. E* **84,** 051803 (2011).

65. Arai, S. & Doi, M. Skin formation and bubble growth during drying process of polymer solution. *Eur. Phys. J. E* **35,** 1–9 (2012).

66. Tso, N.-C. Solvent removal from poly (methyl methacrylate)-toluene solution. (Ohio University, 1984).

67. Kajiya, T., Nishitani, E., Yamaue, T. & Doi, M. Piling-to-buckling transition in the drying process of polymer solution drop on substrate having a large contact angle. *Phys. Rev. E* **73,** 011601 (2006).

68. Gennes, P.-G. de, Brochard-Wyart, F. & Quere, D. *Capillarity and Wetting Phenomena: Drops, Bubbles, Pearls, Waves*. (Springer Science & Business Media, 2004).

69. Deegan, R. D., Bakajin, O., Dupont, T. F., Huber, G., Nagel, S. R. & Witten, T. A. Contact line deposits in an evaporating drop. *Phys. Rev. E* **62,** 756–765 (2000).

70. Hu, H. & Larson, R. G. Marangoni Effect Reverses Coffee-Ring Depositions. *J. Phys. Chem. B* **110,** 7090–7094 (2006).

71. Ristenpart, W. D., Kim, P. G., Domingues, C., Wan, J. & Stone, H. A. Influence of Substrate Conductivity on Circulation Reversal in Evaporating Drops. *Phys. Rev. Lett.* **99,** 234502 (2007).

72. Xu, X. & Luo, J. Marangoni flow in an evaporating water droplet. *Appl. Phys. Lett.* **91,** 124102 (2007).

73. Chang, S. T. & Velev, O. D. Evaporation-Induced Particle Microseparations inside Droplets Floating on a Chip. *Langmuir* **22,** 1459–1468 (2006).

74. Maillard, M., Motte, L., Ngo, A. T. & Pileni, M. P. Rings and Hexagons Made of Nanocrystals: A Marangoni Effect. *J. Phys. Chem. B* **104,** 11871–11877 (2000).

75. Hu, H. & Larson, R. G. Analysis of the Microfluid Flow in an Evaporating Sessile Droplet. *Langmuir* **21,** 3963–3971 (2005).

76. Steinchen, A. & Sefiane, K. Self-organised marangoni motion at evaporating drops or in capillary menisci – thermohydrodynamical model. *J. Non-Equilib. Thermodyn.* **30,** 39–51 (2005).

77. Krishnan, M., Ugaz, V. M. & Burns, M. A. PCR in a Rayleigh-Bénard Convection Cell. *Science* **298,** 793–793 (2002).

78. Rayleigh, Lord. On convection currents in a horizontal layer of fluid, when the higher temperature is on the under side. *Philos. Mag.* **32,** 529–546 (1916).

79. Schatz, M. F. & Neitzel, G. P. Experiments on Thermocapillary Instabilities. *Annu. Rev. Fluid Mech.* **33,** 93–127 (2001).

80. Czechowski, L. & Floryan, J. M. Marangoni Instability in a Finite Container-Transition Between Short and Long Wavelengths Modes. *J. Heat Transf.* **123,** 96–104 (2000).

81. Rayleigh. Breath Figures. *Nature* **86,** 416–417 (1911).

82. Rayleigh. Breath Figures. *Nature* **90,** 436–438 (1912).

83. Aitkek, J. Breath Figures. *Nature* **86,** 516–517 (1911).

84. Limaye, A. V., Narhe, R. D., Dhote, A. M. & Ogale, S. B. Evidence for Convective Effects in Breath Figure Formation on Volatile Fluid Surfaces. *Phys. Rev. Lett.* **76,** 3762–3765 (1996).

85. Steyer, A., Guenoun, P., Beysens, D. & Knobler, C. M. Two-dimensional ordering during droplet growth on a liquid surface. *Phys. Rev. B* **42,** 1086–1089 (1990).

86. Knobler, C. M. & Beysens, D. Growth of Breath Figures on Fluid Surfaces. *EPL Europhys. Lett.* **6,** 707 (1988).

87. Pitois, O. & François, B. Crystallization of condensation droplets on a liquid surface. *Colloid Polym. Sci.* **277,** 574–578 (1999).

88. Pitois, O. & François, B. Formation of ordered micro-porous membranes. *Eur. Phys. J. B - Condens. Matter Complex Syst.* **8,** 225–231 (1999).

89. Thomas, E. L., Kinning, D. J., Alward, D. B. & Henkee, C. S. Ordered packing arrangements of spherical micelles of diblock copolymers in two and three dimensions. *Macromolecules* **20,** 2934–2939 (1987).

90. Peng, J., Han, Y., Yang, Y. & Li, B. The influencing factors on the macroporous formation in polymer films by water droplet templating. *Polymer* **45,** 447–452 (2004).

91. Karthaus, O., Cieren, X., Maruyama, N. & Shimomura, M. Mesoscopic 2-D ordering of inorganic/organic hybrid materials. *Mater. Sci. Eng. C* **10,** 103–106 (1999).

92. Barrow, M. S., Jones, R. L., Park, J. O., Srinivasarao, M., Williams, P. R. & Wright, C. J. Physical characterisation of microporous and nanoporous polymer films by atomic force microscopy, scanning electron microscopy and high speed video microphotography. *Spectrosc. Int. J.* **18,** 577–585 (2004).

93. Tian, Y., Jiao, Q., Ding, H., Shi, Y. & Liu, B. The formation of honeycomb structure in polyphenylene oxide films. *Polymer* **47,** 3866–3873 (2006).

94. Hernández-Guerrero, M., Davis, T. P., Barner-Kowollik, C. & Stenzel, M. H. Polystyrene comb polymers built on cellulose or poly(styrene-co-2-hydroxyethylmethacrylate) backbones as substrates for the preparation of structured honeycomb films. *Eur. Polym. J.* **41,** 2264–2277 (2005).

95. Stenzel-Rosenbaum, M. H., Davis, T. P., Fane, A. G. & Chen, V. Porous Polymer Films and Honeycomb Structures Made by the Self-Organization of Well-Defined Macromolecular Structures Created by Living Radical Polymerization Techniques. *Angew. Chem. Int. Ed.* **40,** 3428–3432 (2001).

96. Lord, H. T., Quinn, J. F., Angus, S. D., Whittaker, M. R., Stenzel, M. H. & Davis, T. P. Microgel stars viaReversible Addition Fragmentation Chain Transfer (RAFT) polymerisation — a facile route to macroporous membranes, honeycomb patterned thin films and inverse opal substrates. *J. Mater. Chem.* **13,** 2819–2824 (2003).

97. Stenzel, M. H. & Davis, T. P. Biomimetic Honeycomb-Structured Surfaces Formed from Block Copolymers Incorporating Acryloyl Phosphorylcholine. *Aust. J. Chem.* **56,** 1035–1038 (2003).

98. Stenzel, M. H., Davis, T. P. & Fane, A. G. Honeycomb structured porous films prepared from carbohydrate based polymers synthesized via the RAFT process. *J. Mater. Chem.* **13,** 2090–2097 (2003).

99. Servoli, E., Ruffo, G. A. & Migliaresi, C. Interplay of kinetics and interfacial interactions in breath figure templating – A phenomenological interpretation. *Polymer* **51,** 2337–2344 (2010).

100. Shah, P. s., Sigman, M. b., Stowell, C. a., Lim, K. t., Johnston, K. p. & Korgel, B. a. Single-Step Self-Organization of Ordered Macroporous Nanocrystal Thin Films. *Adv. Mater.* **15,** 971–974 (2003).

101. Su, P. Y., Hu, J. C., Cheng, S. L., Chen, L. J. & Liang, J. M. Self-assembled hexagonal Au particle networks on silicon from Au nanoparticle solution. *Appl. Phys. Lett.* **84,** 3480–3482 (2004).

102. Li, J., Peng, J., Huang, W., Wu, Y., Fu, J., Cong, Y., Xue, L. & Han, Y. Ordered Honeycomb-Structured Gold Nanoparticle Films with Changeable Pore Morphology: From Circle to Ellipse. *Langmuir* **21,** 2017–2021 (2005).

103. Englert, B. C., Scholz, S., Leech, P. J., Srinivasarao, M. & Bunz, U. H. F. Templated Ceramic Microstructures by Using the Breath-Figure Method. *Chem. – Eur. J.* **11,** 995–1000 (2005).

104. Su, Y. S., Kuo, C. Y., Wang, D. M., Lai, J. Y., Deratani, A., Pochat, C. & Bouyer, D. Interplay of mass transfer, phase separation, and membrane morphology in vapor-induced phase separation. *J. Membr. Sci.* **338,** 17–28 (2009).

105. Muñoz-Bonilla, A., Fernández-García, M. & Rodríguez-Hernández, J. Towards hierarchically ordered functional porous polymeric surfaces prepared by the breath figures approach. *Prog. Polym. Sci.* **39,** 510–554 (2014).

106. Dušek, K. & Dušková-Smrčková, M. Network structure formation during crosslinking of organic coating systems. *Prog. Polym. Sci.* **25,** 1215–1260 (2000).

107. Dušková-smrčková, M. & Dušek, K. Processes and states during polymer film formation by simultaneous crosslinking and solvent evaporation. *J. Mater. Sci.* **37,** 4733–4741 (2002).

108. Wang, L., Zhang, Z. & Ding, Y. Photocrosslinking-induced phase separation in evaporative solvents: formation of skin layers and microspheres. *Soft Matter* **9,** 4455–4463 (2013).

109. Inoue, T. Reaction-induced phase decomposition in polymer blends. *Prog. Polym. Sci.* **20,** 119–153 (1995).

110. Yamanaka, K. & Inoue, T. Structure development in epoxy resin modified with poly(ether sulphone). *Polymer* **30,** 662–667 (1989).

111. Guenthner, A. J., Hess, D. M. & Cash, J. J. Morphology development in photopolymerization-induced phase separated mixtures of UV-curable thiol-ene adhesive and low molecular weight solvents. *Polymer* **49,** 5533–5540 (2008).

112. Pinto-Iguanero, B., Olivares-Perez, A. & Fuentes-Tapia, I. Holographic material film composed by Norland Noa 65 (R) adhesive. *Opt. Mater.* **20,** 225–232 (2002).

113. Hoyle, C. E. & Bowman, C. N. Thiol–Ene Click Chemistry. *Angew. Chem. Int. Ed.* **49,** 1540–1573 (2010).

114. Hoyle, C. E., Lee, T. Y. & Roper, T. Thiol–enes: Chemistry of the past with promise for the future. *J. Polym. Sci. Part Polym. Chem.* **42,** 5301–5338 (2004).

115. Decker, C. Photoinitiated crosslinking polymerisation. *Prog. Polym. Sci.* **21,** 593–650 (1996).

116. Decker, C. & Jenkins, A. D. Kinetic approach of oxygen inhibition in ultraviolet- and laser-induced polymerizations. *Macromolecules* **18,** 1241–1244 (1985).

117. O'Brien, A. K. & Bowman, C. N. Impact of Oxygen on Photopolymerization Kinetics and Polymer Structure. *Macromolecules* **39,** 2501–2506 (2006).

118. Weaire, D. & Rivier, N. Soap, cells and statistics—random patterns in two dimensions. *Contemp. Phys.* **25,** 59–99 (1984).

119. Song, L., Sharma, V., Park, J. O. & Srinivasarao, M. Characterization of ordered array of micropores in a polymer film. *Soft Matter* **7,** 1890–1896 (2011).

120. Maruf, S. H., Ahn, D. U., Greenberg, A. R. & Ding, Y. Glass transition behaviors of interfacially polymerized polyamide barrier layers on thin film composite membranes via nano-thermal analysis. *Polymer* **52,** 2643–2649 (2011).

121. Yakacki, C. M., Shandas, R., Safranski, D., Ortega, A. M., Sassaman, K. & Gall, K. Strong, Tailored, Biocompatible Shape-Memory Polymer Networks. *Adv. Funct. Mater.* **18,** 2428–2435 (2008).

122. Nwabunma, D., Kim, K. J., Lin, Y., Chien, L. C. & Kyu, T. Phase Diagram and Photopolymerization Behavior of Mixtures of UV-Curable Multifunctional Monomer and Low Molar Mass Nematic Liquid Crystal. *Macromolecules* **31,** 6806–6812 (1998).

123. Vorflusev, V. & Kumar, S. Phase-Separated Composite Films for Liquid Crystal Displays. *Science* **283,** 1903–1905 (1999).

124. Qian, T., Kim, J.-H., Kumar, S. & Taylor, P. L. Phase-separated composite films: Experiment and theory. *Phys. Rev. E* **61,** 4007–4010 (2000).

125. Traina, M., Galy, J., Gérard, J.-F., Dikic, T. & Verbrugge, T. Synthesis of cross-linked epoxy microparticles: Effect of the synthesis parameters. *J. Colloid Interface Sci.* **368,** 158–164 (2012).

126. Downey, J. S., McIsaac, G., Frank, R. S. & Stöver, H. D. H. Poly(divinylbenzene) Microspheres as an Intermediate Morphology between Microgel, Macrogel, and Coagulum in Cross-Linking Precipitation Polymerization. *Macromolecules* **34,** 4534–4541 (2001).

127. Li, W., Ryan, A. J. & Meier, I. K. Morphology Development via Reaction-Induced Phase Separation in Flexible Polyurethane Foam. *Macromolecules* **35,** 5034–5042 (2002).

128. Siddhamalli, S. K. & Kyu, T. Toughening of thermoset/thermoplastic composites via reaction-induced phase separation: Epoxy/phenoxy blends. *J. Appl. Polym. Sci.* **77,** 1257–1268 (2000).

129. Zhang, X.-Z., Yang, Y.-Y. & Chung, T.-S. Effect of Mixed Solvents on Characteristics of Poly(N-isopropylacrylamide) Gels. *Langmuir* **18,** 2538–2542 (2002).

130. Bailey, B. M., Hui, V., Fei, R. & Grunlan, M. A. Tuning PEG-DA hydrogel properties via solvent-induced phase separation (SIPS). *J. Mater. Chem.* **21,** 18776–18782 (2011).

131. Bailey, B. M., Fei, R., Munoz-Pinto, D., Hahn, M. S. & Grunlan, M. A. PDMSstar–PEG hydrogels prepared via solvent-induced phase separation (SIPS) and their potential utility as tissue engineering scaffolds. *Acta Biomater.* **8,** 4324–4333 (2012).

132. Chirila, T. V., Chen, Y.-C., Griffin, B. J. & Constable, I. J. Hydrophilic sponges based on 2-hydroxyethyl methacrylate. I. effect of monomer mixture composition on the pore size. *Polym. Int.* **32,** 221–232 (1993).

133. Clayton, A. B., Chirila, T. V. & Lou, X. Hydrophilic sponges based on 2-hydroxyethyl methacrylate. V. effect of crosslinking agent reactivity on mechanical properties. *Polym. Int.* **44,** 201–207 (1997).

134. Clayton, A. B., Chirila, T. V. & Dalton, P. D. Hydrophilic Sponges Based on 2-Hydroxyethyl Methacrylate. III. Effect of Incorporating a Hydrophilic Crosslinking Agent on the Equilibrium Water Content and Pore Structure. *Polym. Int.* **42,** 45–56 (1997).

135. Smallwood, I. M. *Handbook of Organic Solvent Properties*. (Wiley, 1996).

136. Burke, J. Solubility Parameters: Theory and Application. *AIC Book Pap. Group Annu.* **3,** 13–58 (1984).

137. Barton, A. F. M. *CRC Handbook of Solubility Parameters and Other Cohesion Parameters, Second Edition*. (CRC Press, 1991).

138. *Polymer Handbook, 2 Volumes Set*. (Wiley-Interscience, 2003).

139. Smallwood, I. M. *Handbook of Organic Solvent Properties*. (Wiley, 1996).

140. Smith, G. W. Cure Parameters and Phase Behavior of An Ultraviolet-Cured Polymer-Dispersed Liquid Crystal. *Mol. Cryst. Liq. Cryst.* **196,** 89–102 (1991).

141. Nephew, J. B., Nihei, T. C. & Carter, S. A. Reaction-Induced Phase Separation Dynamics: A Polymer in a Liquid Crystal Solvent. *Phys. Rev. Lett.* **80,** 3276–3279 (1998).

142. Benmouna, R. & Benyoucef, B. Thermophysical and thermomechanical properties of Norland Optical Adhesives and liquid crystal composites. *J. Appl. Polym. Sci.* **108,** 4072–4079 (2008).

143. Kajiya*, T., Kaneko, D. & Doi, M. Dynamical Visualization of 'Coffee Stain Phenomenon' in Droplets of Polymer Solution via Fluorescent Microscopy. *Langmuir* **24,** 12369–12374 (2008).

144. Li, B., Cao, Y.-P., Feng, X.-Q. & Gao, H. Mechanics of morphological instabilities and surface wrinkling in soft materials: a review. *Soft Matter* **8,** 5728–5745 (2012).

145. Baehr, H. D. & Stephan, K. *Heat and Mass Transfer*. (Springer, 2006).

146. Burdick, J. A., Peterson, A. J. & Anseth, K. S. Conversion and temperature profiles during the photoinitiated polymerization of thick orthopaedic biomaterials. *Biomaterials* **22,** 1779–1786 (2001).

147. O'Brien, A. K. & Bowman, C. N. Modeling Thermal and Optical Effects on Photopolymerization Systems. *Macromolecules* **36,** 7777–7782 (2003).

148. Burdick, J. A., Lovestead, T. M. & Anseth, K. S. Kinetic Chain Lengths in Highly Cross-Linked Networks Formed by the Photoinitiated Polymerization of Divinyl Monomers: A Gel Permeation Chromatography Investigation. *Biomacromolecules* **4,** 149–156 (2003).

149. Dayal, P. & Kyu, T. Porous fiber formation in polymer-solvent system undergoing solvent evaporation. *J. Appl. Phys.* **100,** 043512 (2006).

150. Haraguchi, K., Xu, Y. & Li, G. Poly(N-isopropylacrylamide) Prepared by Free-Radical Polymerization in Aqueous Solutions and in Nanocomposite Hydrogels. *Macromol. Symp.* **306-307,** 33–48 (2011).

151. Bartels, J. W., Cauët, S. I., Billings, P. L., Lin, L. Y., Zhu, J., Fidge, C., Pochan, D. J. & Wooley, K. L. Evaluation of Isoprene Chain Extension from PEO Macromolecular Chain Transfer Agents for the Preparation of Dual, Invertible Block Copolymer Nanoassemblies. *Macromolecules* **43,** 7128–7138 (2010).

152. Levere, M. E., Willoughby, I., O'Donohue, S., Cuendias, A. de, Grice, A. J., Fidge, C., Becer, C. R. & Haddleton, D. M. Assessment of SET-LRP in DMSO using online monitoring and Rapid GPC. *Polym. Chem.* **1,** 1086–1094 (2010).

153. Sousa, R. G., Magalhães, W. F. & Freitas, R. F. S. Glass transition and thermal stability of poly(N-isopropylacrylamide) gels and some of their copolymers with acrylamide. *Polym. Degrad. Stab.* **61,** 275–281 (1998).

154. Zheng, C., He, W.-D., Liu, W.-J., Li, J. & Li, J.-F. Novel One-Step Route for Preparing Amphiphilic Block Copolymers of Styrene and N-Isopropylacrylamide in a Microemulsion. *Macromol. Rapid Commun.* **27,** 1229–1232 (2006).

155. Ifuku, S. & Kadla, J. F. Preparation of a Thermosensitive Highly Regioselective Cellulose/N-Isopropylacrylamide Copolymer through Atom Transfer Radical Polymerization. *Biomacromolecules* **9,** 3308–3313 (2008).

156. Zeng, K., Fang, Y. & Zheng, S. Organic-Inorganic Hybrid Hydrogels Involving Poly(N-isopropylacrylamide) and Polyhedral Oligomeric Silsesquioxane: Preparation and Rapid Thermoresponsive Properties. *J. Polym. Sci. Part B-Polym. Phys.* **47,** 504–516 (2009).

157. Cheremisinoff, P. *Handbook of Engineering Polymeric Materials*. (CRC Press, 1997).

158. Li, D., Zhang, X., Yao, J., Simon, G. P. & Wang, H. Stimuli-responsive polymer hydrogels as a new class of draw agent for forward osmosis desalination. *Chem. Commun.* **47,** 1710–1712 (2011).

159. Berg, G. J., Gong, T., Fenoli, C. R. & Bowman, C. N. A Dual-Cure, Solid-State Photoresist Combining a Thermoreversible Diels–Alder Network and a Chain Growth Acrylate Network. *Macromolecules* **47,** 3473–3482 (2014).

160. Carenza, M. & Veronese, F. M. Entrapment of biomolecules into hydrogels obtained by radiation-induced polymerization. *J. Controlled Release* **29,** 187–193 (1994).

161. Skelly, P. J. & Tighe, B. J. Novel macroporous hydrogel adsorbents for artificial liver support haemoperfusion systems. *Polymer* **20,** 1051–1052 (1979).

162. El-Sherbiny, I. M., McGill, S. & Smyth, H. D. C. Swellable microparticles as carriers for sustained pulmonary drug delivery. *J. Pharm. Sci.* **99,** 2343–2356 (2010).

163. Yadavalli, V. K., Koh, W.-G., Lazur, G. J. & Pishko, M. V. Microfabricated protein-containing poly(ethylene glycol) hydrogel arrays for biosensing. *Sens. Actuators B Chem.* **97,** 290–297 (2004).

164. Romack, T. J., Maury, E. E. & DeSimone, J. M. Precipitation Polymerization of Acrylic Acid in Supercritical Carbon Dioxide. *Macromolecules* **28,** 912–915 (1995).

165. Xu, Q., Han, B. & Yan, H. Precipitation polymerization of acrylic acid in compressed carbon dioxide–cosolvent systems. *J. Appl. Polym. Sci.* **88,** 1876–1880 (2003).

166. Liu, T., Garner, P., DeSimone, J. M., Roberts, G. W. & Bothun, G. D. Particle Formation in Precipitation Polymerization: Continuous Precipitation Polymerization of Acrylic Acid in Supercritical Carbon Dioxide. *Macromolecules* **39,** 6489–6494 (2006).

167. Xu, Q., Han, B. & Yan, H. Effect of cosolvents on the precipitation polymerization of acrylic acid in supercritical carbon dioxide. *Polymer* **42,** 1369–1373 (2001).

168. Heskins, M. & Guillet, J. E. Solution Properties of Poly(N-isopropylacrylamide). *J. Macromol. Sci. Part - Chem.* **2,** 1441–1455 (1968).

169. Otake, K., Inomata, H., Konno, M. & Saito, S. Thermal analysis of the volume phase transition with N-isopropylacrylamide gels. *Macromolecules* **23,** 283–289 (1990).

170. Grinberg, V. Y., Dubovik, A. S., Kuznetsov, D. V., Grinberg, N. V., Grosberg, A. Y. & Tanaka, T. Studies of the thermal volume transition of poly(N-isopropylacrylamide) hydrogels by high-sensitivity differential scanning microcalorimetry. 2. Thermodynamic functions. *Macromolecules* **33,** 8685–8692 (2000).

171. Cho, E. C., Lee, J. & Cho, K. Role of bound water and hydrophobic interaction in phase transition of poly(N-isopropylacrylamide) aqueous solution. *Macromolecules* **36,** 9929–9934 (2003).

172. Kirstein, J., Platschek, B., Jung, C., Brown, R., Bein, T. & Bräuchle, C. Exploration of nanostructured channel systems with single-molecule probes. *Nat. Mater.* **6,** 303–310 (2007).

173. Zürner, A., Kirstein, J., Döblinger, M., Bräuchle, C. & Bein, T. Visualizing single-molecule diffusion in mesoporous materials. *Nature* **450,** 705–708 (2007).

174. Wong, I. Y., Gardel, M. L., Reichman, D. R., Weeks, E. R., Valentine, M. T., Bausch, A. R. & Weitz, D. A. Anomalous Diffusion Probes Microstructure Dynamics of Entangled F-Actin Networks. *Phys. Rev. Lett.* **92,** 178101 (2004).

175. Lee, C. H., Crosby, A. J., Emrick, T. & Hayward, R. C. Characterization of Heterogeneous Polyacrylamide Hydrogels by Tracking of Single Quantum Dots. *Macromolecules* **47,** 741–749 (2014).

176. Guan, J., Wang, B. & Granick, S. Even Hard-Sphere Colloidal Suspensions Display Fickian Yet Non-Gaussian Diffusion. *ACS Nano* **8,** 3331–3336 (2014).

177. He, K., Babaye Khorasani, F., Retterer, S. T., Thomas, D. K., Conrad, J. C. & Krishnamoorti, R. Diffusive Dynamics of Nanoparticles in Arrays of Nanoposts. *ACS Nano* **7,** 5122–5130 (2013).

178. Eral, H. B., Oh, J. M., van den Ende, D., Mugele, F. & Duits, M. H. G. Anisotropic and Hindered Diffusion of Colloidal Particles in a Closed Cylinder. *Langmuir* **26,** 16722–16729 (2010).

179. Parthasarathy, R. Rapid, accurate particle tracking by calculation of radial symmetry centers. *Nat. Methods* **9,** 724–726 (2012).

180. Yan, H., Blanford, C. F., Holland, B. T., Parent, M., Smyrl, W. H. & Stein, A. A Chemical Synthesis of Periodic Macroporous NiO and Metallic Ni. *Adv. Mater.* **11,** 1003–1006 (1999).

181. Bartlett, P. N., Birkin, P. R. & Ghanem, M. A. Electrochemical deposition of macroporous platinum,palladium and cobalt films using polystyrene latex sphere templates. *Chem. Commun.* 1671–1672 (2000). doi:10.1039/B004398M

182. Ye, Y.-H., Badilescu, S. & Truong, V.-V. Large-scale ordered macroporous SiO2 thin films by a template-directed method. *Appl. Phys. Lett.* **81,** 616–618 (2002).

183. Blanco, A., Chomski, E., Grabtchak, S., Ibisate, M., John, S., Leonard, S. W., Lopez, C., Meseguer, F., Miguez, H., Mondia, J. P., Ozin, G. A., Toader, O. & van Driel, H. M. Large-scale synthesis of a silicon photonic crystal with a complete three-dimensional bandgap near 1.5 micrometres. *Nature* **405,** 437–440 (2000).

184. Xia, Y., Gates, B., Yin, Y. & Lu, Y. Monodispersed Colloidal Spheres: Old Materials with New Applications. *Adv. Mater.* **12,** 693–713 (2000).

185. Sun, F., Cai, W. P., Li, Y., Cao, B., Lu, F., Duan, G. & Zhang, L. Morphology Control and Transferability of Ordered Through-Pore Arrays Based on the Electrodeposition of a Colloidal Monolayer. *Adv. Mater.* **16,** 1116–1121 (2004).

186. Guliants, V. V., Carreon, M. A. & Lin, Y. S. Ordered mesoporous and macroporous inorganic films and membranes. *J. Membr. Sci.* **235,** 53–72 (2004).

187. Kulinowski, K. M., Jiang, P., Vaswani, H. & Colvin, V. L. Porous Metals from Colloidal Templates. *Adv. Mater.* **12,** 833–838 (2000).

188. Velev, O. D., Jede, T. A., Lobo, R. F. & Lenhoff, A. M. Porous silica via colloidal crystallization. *Nature* **389,** 447–448 (1997).

189. Sen, T., Tiddy, G. J. T., Casci, J. L. & Anderson, M. W. Synthesis and Characterization of Hierarchically Ordered Porous Silica Materials. *Chem. Mater.* **16,** 2044–2054 (2004).

190. Holland, B. T., Blanford, C. F. & Stein, A. Synthesis of Macroporous Minerals with Highly Ordered Three-Dimensional Arrays of Spheroidal Voids. *Science* **281,** 538–540 (1998).

191. Jiang, P., Hwang, K. S., Mittleman, D. M., Bertone, J. F. & Colvin, V. L. Template-Directed Preparation of Macroporous Polymers with Oriented and Crystalline Arrays of Voids. *J. Am. Chem. Soc.* **121,** 11630–11637 (1999).

192. Imhof, A. & Pine, D. J. Ordered macroporous materials by emulsion templating. *Nature* **389,** 948–951 (1997).

193. Imhof, A. & Pine, D. J. Uniform Macroporous Ceramics and Plastics by Emulsion Templating. *Adv. Mater.* **10,** 697–700 (1998).

194. Bibette, J. Depletion interactions and fractionated crystallization for polydisperse emulsion purification. *J. Colloid Interface Sci.* **147,** 474–478 (1991).

195. Hamley, I. W. *The Physics of Block Copolymers*. (Oxford University Press, 1999).

196. Bates, F. S. Polymer-Polymer Phase Behavior. *Science* **251,** 898–905 (1991).

197. Bates, F. S. & Fredrickson, G. H. Block Copolymers—Designer Soft Materials. *Phys. Today* **52,** 32–38 (1999).

198. Tan, H., Moet, A., Hiltner, A. & Baer, E. Thermoreversible gelation of atactic polystyrene solutions. *Macromolecules* **16,** 28–34 (1983).

199. Tong, L. K. J. & Kenyon, W. O. Heats of Polymerization. I. An Isothermal Calorimeter and its Application to Methyl Methacrylate. *J. Am. Chem. Soc.* **67,** 1278–1281 (1945).

200. Lee, H. & Colby, C. Heat of polymerization of nine mono-, di-, and trimethacrylate esters tested neat and with low levels of peroxide by dynamic differential scanning calorimetry. *Dent. Mater.* **2,** 175–178 (1986).

201. Matsumoto, K., Talukdar, B. & Endo, T. Synthesis and properties of methacrylate-based ionic networked polymers containing ionic liquids: comparison of ionic and nonionic networked polymers. *Polym. Bull.* **66,** 771–778 (2011).

202. Lu, H., Carioscia, J. A., Stansbury, J. W. & Bowman, C. N. Investigations of step-growth thiol-ene polymerizations for novel dental restoratives. *Dent. Mater.* **21,** 1129–1136 (2005).

203. Hayakawa, T. & Horiuchi, S. From Angstroms to Micrometers: Self-Organized Hierarchical Structure within a Polymer Film. *Angew. Chem. Int. Ed.* **42,** 2285–2289 (2003).

204. Goodner, M. D. & Bowman, C. N. Development of a comprehensive free radical photopolymerization model incorporating heat and mass transfer effects in thick films. *Chem. Eng. Sci.* **57,** 887–900 (2002).

205. Galina, H., Dušek, K., Tuzar, Z., Bohdanecky, M. & Štokr, J. The structure of low conversion polymers of ethylene dimethacrylate. *Eur. Polym. J.* **16,** 1043–1046 (1980).

206. Naghash, H. J., Okay, O. & Yaĝci, Y. Gel formation by chain-crosslinking photopolymerization of methyl methacrylate and ethylene glycol dimethacrylate. *Polymer* **38,** 1187–1196 (1997).

207. Storey, B. T. Copolymerization of styrene and p-divinylbenzene. Initial rates and gel points. *J. Polym. Sci. A* **3,** 265–282 (1965).

208. Rey, L., Galy, J. & Sautereau, H. Reaction Kinetics and Morphological Changes during Isothermal Cure of Vinyl/Dimethacrylate Networks. *Macromolecules* **33,** 6780–6786 (2000).

209. Kast, H. & Funke, W. Crosslinking mechanism in radical polymerization of tetrafunctional monomers. *Makromol. Chem.* **180,** 1335–1338 (1979).

210. Deegan, R. D. Pattern formation in drying drops. *Phys. Rev. E* **61,** 475–485 (2000).

211. Kajiya, T., Monteux, C., Narita, T., Lequeux, F. & Doi, M. Contact-Line Recession Leaving a Macroscopic Polymer Film in the Drying Droplets of Water−Poly(N,N-dimethylacrylamide) (PDMA) Solution. *Langmuir* **25,** 6934–6939 (2009).

212. Maruyama, N., Koito, T., Nishida, J., Sawadaishi, T., Cieren, X., Ijiro, K., Karthaus, O. & Shimomura, M. Mesoscopic patterns of molecular aggregates on solid substrates. *Thin Solid Films* **327–329,** 854–856 (1998).

213. Nishikawa, T., Ookura, R., Nishida, J., Arai, K., Hayashi, J., Kurono, N., Sawadaishi, T., Hara, M. & Shimomura, M. Fabrication of Honeycomb Film of an Amphiphilic Copolymer at the Air−Water Interface. *Langmuir* **18,** 5734–5740 (2002).

214. Nishikawa, T., Nishida, J., Ookura, R., Nishimura, S.-I., Wada, S., Karino, T. & Shimomura, M. Mesoscopic patterning of cell adhesive substrates as novel biofunctional interfaces. *Mater. Sci. Eng. C* **10,** 141–146 (1999).

215. Ishii, D., Yabu, H. & Shimomura, M. Novel Biomimetic Surface Based on a Self-Organized Metal−Polymer Hybrid Structure. *Chem. Mater.* **21,** 1799–1801 (2009).

216. Castro, F., Westbrook, K. K., Hermiller, J., Ahn, D. U., Ding, Y. & Qi, H. J. Time and Temperature Dependent Recovery of Epoxy-Based Shape Memory Polymers. *J. Eng. Mater. Technol.* **133,** 021025–021025 (2011).

217. Levchik, G. F., Si, K., Levchik, S. V., Camino, G. & Wilkie, C. A. The correlation between cross-linking and thermal stability: Cross-linked polystyrenes and polymethacrylates. *Polym. Degrad. Stab.* **65,** 395–403 (1999).

218. Yabu, H., Takebayashi, M., Tanaka, M. & Shimomura, M. Superhydrophobic and Lipophobic Properties of Self-Organized Honeycomb and Pincushion Structures. *Langmuir* **21,** 3235–3237 (2005).

219. Yabu, H., Hirai, Y., Kojima, M. & Shimomura, M. Surface Properties of Honeycomb and Pincushion Structures of Various Hydrophobic Polymer Materials Prepared by Self-Organization. *J. Adhes. Sci. Technol.* **22,** 277–284 (2008).

220. Cassie, A. B. D. Contact angles. *Discuss. Faraday Soc.* **3,** 11–16 (1948).